

January 2014

Automated Localization and Segmentation of Pelvic Floor Structures on MRI to Predict Pelvic Organ Prolapse

Sinan Onal

University of South Florida, sonal@mail.usf.edu

Follow this and additional works at: <http://scholarcommons.usf.edu/etd>

 Part of the [Biomedical Engineering and Bioengineering Commons](#), and the [Industrial Engineering Commons](#)

Scholar Commons Citation

Onal, Sinan, "Automated Localization and Segmentation of Pelvic Floor Structures on MRI to Predict Pelvic Organ Prolapse" (2014).
Graduate Theses and Dissertations.
<http://scholarcommons.usf.edu/etd/5288>

This Dissertation is brought to you for free and open access by the Graduate School at Scholar Commons. It has been accepted for inclusion in Graduate Theses and Dissertations by an authorized administrator of Scholar Commons. For more information, please contact scholarcommons@usf.edu.

Automated Localization and Segmentation of Pelvic Floor Structures on MRI to
Predict Pelvic Organ Prolapse

by

Sinan Onal

A dissertation submitted in partial fulfillment
of the requirements for the degree of
Doctor of Philosophy
Department of Industrial and Management Systems Engineering
College of Engineering
University of South Florida

Major Professor: Susana Lai-Yuen, Ph.D.
Stuart Hart, M.D.
Paul Bao, Ph.D.
Alfredo Weitzenfeld, Ph.D.
Tapas Das, Ph.D.
Bo Zeng, Ph.D.
Ravi Sankar, Ph.D.

Date of Approval:
May 29, 2014

Keywords: Medical Imaging, Prediction, Organ Location, SVM, Non-linear Regression

Copyright © 2014, Sinan Onal

Acknowledgments

I would like to express my heartfelt gratitude to my advisor, Dr. Susana Lai-Yuen for her supervision, and guidance from the very early stages of this research. She has always provided me constant encouragement and support in various ways in my journey of growing into a researcher and scientist. I am indebted to her more than she knows. My sincere thanks also go to Dr. Stuart Hart for his advice and crucial contribution to this study, which made him a backbone of this research. His involvement with his expertise in this area has triggered and nourished mine. I would also like to thank Dr. Paul Bao and Dr. Alfredo Weitzenfeld for guiding my research for the past several years and helping me to develop my background in medical image processing and machine learning. Dr. Tapas Das, Dr. Bo Zeng, and Dr. Ravi Sankar deserve special thanks as other members of my committee. Their being accessible and approachable as well as their instant support when I am in need has helped me experience a smoother and more fruitful process throughout this study. My sincere thanks also go to Dr. Jose Zayas-Castro for his endless support during my graduate study.

Last but not least, words fail me to express my appreciation to my wife Derya whose unconditional love and support, and persistent confidence in me, has taken the load off my shoulder, and to my one-and-only daughter, Pera, the reason of my life, for simply cheering it up and making it more meaningful with her presence every passing day. I would not be here today without them and their love.

Table of Contents

List of Tables	iii
List of Figures	v
Abstract	vii
Chapter 1: Introduction	1
1.1 Motivation.....	1
1.2 Dissertation Objectives and Contributions	3
1.3 Intellectual Merit.....	5
1.4 Broader Impact.....	6
1.5 Dissertation Outline	7
Chapter 2: Pelvic Organ Prolapse and its Diagnosis	9
2.1 Anatomy of the Female Pelvic Floor	9
2.2 Types of POP	11
2.3 Clinical Diagnosis of POP	12
2.4 Medical Imaging Techniques for Diagnosis of POP	15
2.5 Summary	19
Chapter 3: Literature Review	20
3.1 Pelvic Organ Prolapse Diagnosis using MRI.....	20
3.2 Medical Image Object Localization.....	22
3.2.1 Geometric Methods.....	22
3.2.2 Statistical Atlas-based Methods	22
3.2.3 Supervised Methods.....	23
3.3 Segmentation of Bone Structures on MRI	24
3.3.1 Model-Free Based Algorithms.....	25
3.3.2 Model Based Algorithms	26
3.4 Classification Systems and Feature Selection for Medical Diagnosis.....	29
3.4.1 Classification Systems	29
3.4.2 Feature Selection for Medical Diagnosis	31
3.5 Current Challenges to be Addressed in the Proposed Research	32
Chapter 4: Multiple Bone Localization on MRI.....	33
4.1 Overview of Multiple Bone Localization Model.....	33
4.2 Dataset Description.....	36
4.3 Identification of Bladder and Rectum.....	37
4.4 Identification of Pubic Bone Region.....	39

4.4.1 Keypoints Extraction	39
4.4.2 Generation of Candidate Bounding Boxes	42
4.4.3 Feature Extraction of Candidate Regions	44
4.4.4 Classification of Bounding Boxes	45
4.5 Identification of Coccyx and Sacral Promontory Regions	46
4.6 Results	48
4.7 Conclusion	53
Chapter 5: Image-based Pelvic Floor Measurements Model	54
5.1 Overview of Proposed Segmentation Method	54
5.2 Pre-segmentation Stage	56
5.3 Segmentation Stage	58
5.3.1 Feature Extraction	58
5.3.2 Block Classification	59
5.3.3 Block Clustering	61
5.3.4 Leak Detection and Registration	62
5.4 Point Identification Stage	63
5.5 Results	66
5.5.1 Segmentation Accuracy	66
5.5.2 Bone Segmentation	67
5.5.3 Reference Points Accuracy	73
5.5.4 Identification of the Reference Points	73
5.6 Conclusion	75
Chapter 6: Prediction Model for the Diagnosis of POP	77
6.1 Overview of the Prediction Model	77
6.2 Material and Methods	78
6.2.1 Data Acquisition	78
6.2.2 Methods	80
6.2.2.1 Automatic Extraction of MRI-based Features	80
6.2.2.2 Prediction Model	81
6.3 Results	83
6.4 Conclusion	86
Chapter 7: Discussion and Future Work	88
7.1 Discussion	88
7.2 Future Work	90
References	92
Appendices	102
Appendix A Data Acquisition Form	103
Appendix B IRB Approval	105
Appendix C Copyrights Permissions	106
About the Author	End Page

List of Tables

Table 2.1:	Pelvic organ prolapse quantification (POP-Q) system	14
Table 2.2:	Pelvic organ prolapse stages	14
Table 4.1:	Average center error (mean \pm standard deviation) for pelvic bone detection over 90 testing images	49
Table 5.1:	Intensity and GLCM features.....	58
Table 5.2:	Significance of each variable in the performance of the segmentation processes	69
Table 5.3:	Min and max standard deviation of reference points identified over all trials on 15 patients performed by 3 experts	74
Table 5.4:	Hausdorff distance and mean distance between point location identified by the proposed method and manual ground truth point location	74
Table 5.5:	Euclidian distance between points identified manually and using proposed model for 15 patients	74
Table 5.6:	Reference point accuracy based on different distance ranges	75
Table 6.1:	Patient characteristics.....	79
Table 6.2:	Distribution of prolapse cases with their corresponding stages for the studied group	79
Table 6.3:	Significant features for anterior prolapse.....	83
Table 6.4:	Significant features for apical prolapse.....	84
Table 6.5:	Significant features for posterior prolapse	84
Table 6.6:	The distribution of cases for the training and testing datasets for each type of prolapse.....	84
Table 6.7:	The distribution of prolapse stages within the testing and training datasets.....	85

Table 6.8:	Accuracy of the proposed prediction model for different types of prolapse and different types of features.....	86
Table A.1:	Data acquisition form.....	103

List of Figures

Figure 1.1:	MRI midsagittal view with currently used reference lines, MPL and PCL, for grading POP	2
Figure 1.2:	Dissertation objectives	4
Figure 2.1:	Female pelvic floor structure, sagittal view	10
Figure 2.2:	Types of pelvic organ prolapse	11
Figure 2.3:	Points and landmarks for POP-Q system examination	14
Figure 2.4:	Stage 3 leading edge: posterior wall prolapse.....	15
Figure 2.5:	The most popular imaging techniques	16
Figure 2.6:	Commonly used reference lines for grading pelvic organ prolapse	18
Figure 4.1:	Regions of interest with corresponding reference points.....	34
Figure 4.2:	Overview of the proposed multiple bone localization method	35
Figure 4.3:	Illustration of bladder and rectum localization	39
Figure 4.4:	Corner points extraction over an image with the Harris corner algorithm	41
Figure 4.5:	Keypoints within the local vicinity of the bladder.....	42
Figure 4.6:	Candidate region generation	43
Figure 4.7:	Generated candidate regions	43
Figure 4.8:	2D box features	44
Figure 4.9:	Parameterization of location of pelvic floor structure	47
Figure 4.10:	Percentage of correctly detected cases by the proposed bone localization model for different thresholds of DSI.....	50
Figure 4.11:	Results of bone localization	51

Figure 5.1:	Point of interests and proposed MRI-based features	55
Figure 5.2:	Overview of the proposed multi-stage method	56
Figure 5.3:	KxL size cropped image (window) and m×n size blocks	57
Figure 5.4:	Proposed segmentation process	64
Figure 5.5:	Reference bony joints for sacral promontory and coccyx	65
Figure 5.6:	Pelvic floor reference points and lines generated by the proposed method.....	65
Figure 5.7:	Performance comparison of the proposed method and texture-based block classification only for the average over the 20 image sequences per patient	67
Figure 5.8:	Performance comparison of the proposed method with other commonly used segmentation methods	71
Figure 6.1:	Region of interests and proposed MRI-based features	81

Abstract

Pelvic organ prolapse (POP) is a major health problem that affects women. POP is a herniation of the female pelvic floor organs (bladder, uterus, small bowel, and rectum) into the vagina. This condition can cause significant problems such as urinary and fecal incontinence, bothersome vaginal bulge, incomplete bowel and bladder emptying, and pain/discomfort. POP is normally diagnosed through clinical examination since there are few associated symptoms. However, clinical examination has been found to be inadequate and in disagreement with surgical findings. This makes POP a common but poorly understood condition. Dynamic magnetic resonance imaging (MRI) of the pelvic floor has become an increasingly popular tool to assess POP cases that may not be evident on clinical examination. Anatomical landmarks are manually identified on MRI along the midsagittal plane to determine reference lines and measurements for grading POP. However, the manual identification of these points, lines and measurements on MRI is a time-consuming and subjective procedure. This has restricted the correlation analysis of MRI measurements with clinical outcomes to improve the diagnosis of POP and predict the risk of development of this disorder.

The main goal of this research is to improve the diagnosis of pelvic organ prolapse through a model that automatically extracts image-based features from patient specific MRI and fuses them with clinical outcomes. To extract image-based features, anatomical landmarks need to be identified on MRI through the localization and segmentation of pelvic bone structures. This is the main challenge of current algorithms, which tend to fail during bone localization and segmentation on MRI. The proposed research consists of three major objectives: (1) to

automatically identify pelvic floor structures on MRI using a multivariate linear regression model with global information, (2) to identify image-based features using a hybrid technique based on texture-based block classification and K-means clustering analysis to improve the segmentation of bone structures on images with low contrast and image inhomogeneity, (3) to design, test and validate a prediction model using support vector machines with correlation analysis based feature selection to improve disease diagnosis.

The proposed model will enable faster and more consistent automated extraction of features from images with low contrast and high inhomogeneity. This is expected to allow studies on large databases to improve the correlation analysis between MRI features and clinical outcomes. The proposed research focuses on the pelvic region but the techniques are applicable to other anatomical regions that require automated localization and segmentation of multiple structures from images with high inhomogeneity, low contrast, and noise. This research can also be applicable to the automated extraction and analysis of image-based features for the diagnosis of other diseases where clinical examination is not adequate. The proposed model will set the foundation towards a computer-aided decision support system that will enable the fusion of image, clinical, and patient data to improve the diagnosis of POP through personalized assessment. Automating the process of pelvic floor measurements on radiologic studies will allow the use of imaging to predict the development of POP in predisposed patients, and possibly lead to preventive strategies.

Chapter 1

Introduction

The scope of this chapter is to introduce the research motivation and background. The research objectives and contributions are also presented followed by the dissertation outline.

1.1. Motivation

Pelvic Organ Prolapse (POP) is a major health problem affecting up to 30-50% of women and resulting in direct costs of about \$1 billion per year [1, 2]. POP is a herniation of the female pelvic floor organs (bladder, uterus, small bowel and rectum) into the vagina. This condition can cause significant problems including a bothersome vaginal bulge, incontinence, and incomplete bowel and bladder emptying. Almost 75% of women report a profound effect on their quality of life due to POP [3]. It is estimated that by the year 2030, the population of women over the age of 65 years in the U.S. will double to approximately 40 million [4]. Subsequently, the demand for women seeking care for POP will continue to increase significantly. POP is normally diagnosed through clinical examination since there are few associated symptoms. The International Continence Society (ICS) recommends the use of the Pelvic Organ Prolapse Quantification (POP-Q) system, which is a clinical examination that is currently considered the gold standard for assessing POP [5]. However, clinical examination has been found to be inadequate and in disagreement with surgical findings [6, 7]. Studies indicate that the clinical examination for POP concurred with surgical findings in only 59% of patients [8, 9]. Moreover, POP repair procedures are associated with high failure rates, with approximately 30% of women

who undergo surgical repair requiring another surgery for recurrence of symptoms within four years [10]. This makes POP a common but poorly understood condition.

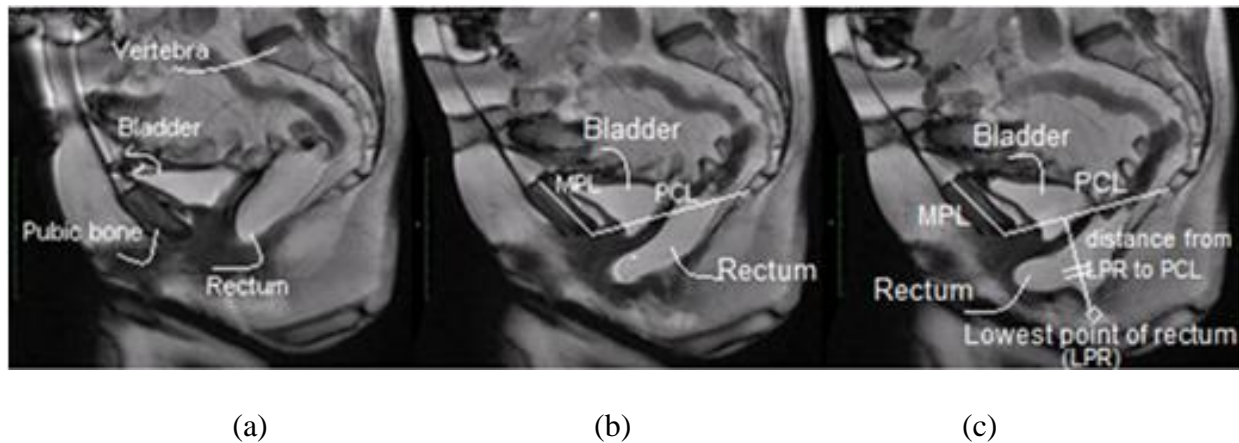


Figure 1.1: MRI midsagittal view with currently used reference lines, MPL and PCL, for grading POP. (a) Rest position, (b-c) Strain position

Dynamic magnetic resonance imaging (MRI) of the pelvic floor has become increasingly popular in assessing POP cases that may not be evident on clinical examination. It offers the advantages of providing a global assessment of the pelvic floor with associated interactions of pelvic organs, superior soft tissue contrast, and absence of ionizing radiation. Dynamic MRI is especially important in the diagnosis of patients with multi-compartment prolapse or who have failed previous prolapse surgeries. During the analysis of dynamic MRI, anatomical landmarks are identified manually on the midsagittal plane to determine lines and measurements for grading POP as shown in Figure 1.1. Although there are commonly used reference lines, there is no standardized system for evaluating MRI measurements for POP [11, 12]. Various reference lines have been proposed to improve diagnosis [13, 14]. Unfortunately, the manual identification of these MRI pelvic floor measurements is a time-consuming and subjective procedure. Current studies only analyzed small sample sizes resulting in limited and non-comparable data [15]. This has restricted the correlation analysis of MRI measurements with clinical information as well as

the validation of newly proposed reference lines. Therefore, there is an urgent need to improve and automate the diagnosis of POP to create prevention strategies. However, there is currently very few data to predict the risk of development of this disorder and the variables associated with its development remain poorly understood [16].

1.2. Dissertation Objectives and Contributions

The main goal of this research is to improve the diagnosis of pelvic organ prolapse through a model that automatically extracts image-based features from patient specific MRI and fuses them with clinical information. A model that automatically extracts image-based predictors from patient specific MRI and fuses them with wide range clinical information can lead to personalized and evidence-based diagnosis to prevent incorrect surgeries and minimize healthcare costs. To extract image-based features, anatomical landmarks need to be identified on MRI through the localization and segmentation of pelvic bone structures. Although dynamic MRI provides better information about soft tissues and their movement, bones are not easily differentiable from the soft tissue as their pixel intensities tend to be very similar and affected by disturbances like noise. This is the main challenge of current algorithms that tend to fail during bone localization and segmentation on MRI due to the large search space, numerous local minima, image inhomogeneity, and/or high computational cost. At the same time, image-based predictors are currently extracted manually resulting in a time-consuming and subjective procedure. This has led to current studies that can only analyze small sample sizes leading to limited and non-comparable data. Consequently, the correlation analysis of MRI-based predictors with clinical information has been limited restricting the development of healthcare systems that offer relevant decision support to clinicians at the point of care.

Our approach aims to overcome these limitations by proposing the basis of a system that automatically locates pelvic floor bone structures on MRI to extract image-based predictors; and then analyzes the correlation between the image-based features and clinical information to help predict POP cases.

The proposed research consists of three main research objectives as shown in Figure 1.2:

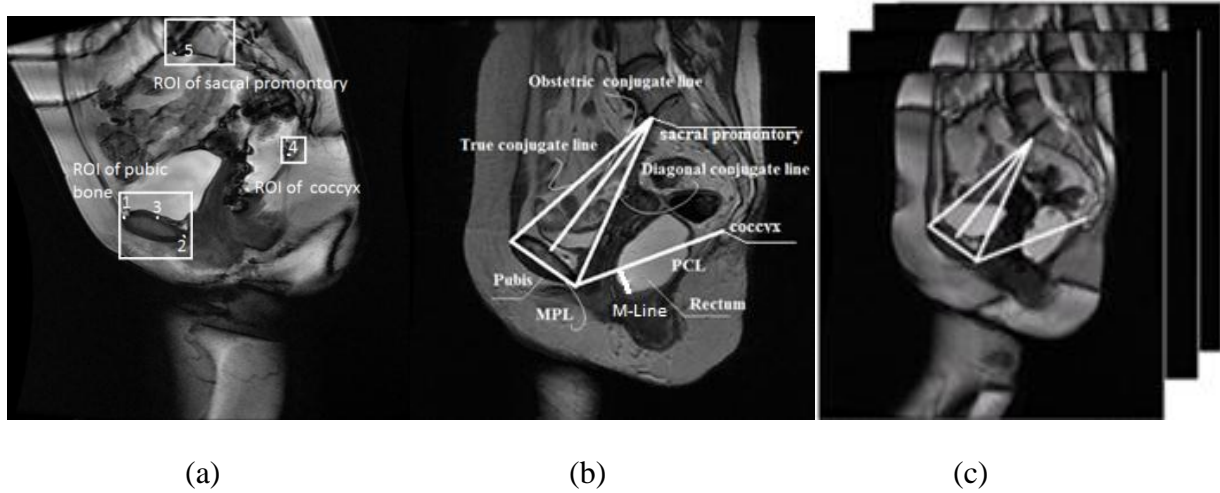


Figure 1.2: Dissertation objectives. (a) Automated multi-organ localization, (b) Identification of image based features and reference lines, (c) Prediction model for POP diagnosis

(1) To automatically identify pelvic floor structures on MRI using a non-linear regression model with global information. A model using non-linear regression is proposed for localizing multiple pelvic bone structures on patient specific MRI and extracting image features associated with POP. This will be achieved by integrating global information based on the relative location between objects' classes. This aims to improve the localization of pelvic organ structures without any user interaction.

(2) To identify image-based features through the segmentation of bone structures using a hybrid technique based on texture-based block classification and K-means clustering analysis. Prior shape information of the pelvic bone is generated and incorporated into the segmentation

process. Morphological skeleton operation is integrated to find the reference points located on the pubic bone while a corner detection algorithm is used to find reference points located on the vertebra. The proposed technique aims to improve the segmentation of bone structures from images with low contrast and non-homogeneous.

(3) To design, test and validate a prediction model using support vector machines with correlation analysis based feature selection to improve disease diagnosis. A dataset of 207 MRI from patients with and without POP is used in this study. Metrics were designed to assess the accuracy and reproducibility of the automated feature extraction method compared to manual feature extraction. The prediction model was built using the extracted MRI features from Objectives 1 and 2 to test with the clinical information using a proposed Support Vector Machines approach with correlation analysis based feature selection. The model was tested for accuracy, sensitivity and specificity.

1.3. Intellectual Merit

The proposed research aims to address the aforementioned medical and engineering challenges through the design of a framework that (1) automatically identifies pelvic floor structures on MRI, (2) extracts image-based features through bone segmentation from images with low contrast and high inhomogeneity, and (3) analyzes the extracted image-based features with clinical information to build a prediction model to assist in the diagnosis of POP. To address the engineering challenges, pelvic floor structures are automatically identified using a non-linear regression model that captures global and local information. Then, the corresponding landmarks are identified using a hybrid supervised and unsupervised image segmentation technique that integrates texture-based block classification and k-means clustering. These

techniques enable the localization of multiple bone structures and their landmarks on MRI by using both local and global information to overcome the problems of image inhomogeneity and numerous local minima. Medically, a prediction model using the extracted MRI features to test with the clinical information was designed using a support vector machines approach with correlation analysis based feature selection. The proposed feature selection consists of independent significance feature selection followed by sequential forward selection. This will allow the selection of an appropriate set of features that have high separability power to improve the accuracy of the classification process and consequently, improve POP diagnosis.

The proposed model will allow high-throughput analysis of images with high inhomogeneity, low contrast, and noise. It will also enable the design of a quantitative prediction model for improving the accuracy of diagnosis of POP while increasing our understanding of the relationships between image-based features and clinical information. The proposed research will set the foundation towards a computer-aided decision support system that will enable the fusion of image, clinical, and patient data to improve the diagnosis of POP through personalized and evidence based assessment.

1.4. Broader Impact

The outcome of the proposed research is a quantitative prediction model that automatically extracts and analyzes image and textual data to improve the accuracy of diagnosis of pelvic organ prolapse (POP). There are a number of broader impacts that are expected as a result of this research. First of all, the ability to automate the process of image based feature extraction for the pelvic floor on radiologic studies will allow the use of imaging technology to predict the development of POP in predisposed patients, and possibly lead to the development of

preventive strategies. Compared to current clinical examination, the use of imaging technology is less invasive and can provide a global view of the pelvic floor. Additionally, it is expected that this quantitative prediction model will enable more accurate diagnosis of POP and consequently help reduce health care costs by decreasing the number of unnecessary surgeries. Moreover, after this model begins to be widely used, it is anticipated that it will also serve as a medical training tool to educate local and nationwide healthcare professionals in order to have a better knowledge of pelvic organ prolapse disorder and its causes.

Although this research focuses on the pelvic region, the proposed object localization, segmentation, and prediction model is applicable to other anatomical regions where images have low contrast, high inhomogeneity, and noise. This research can also be applicable to the automated extraction and analysis of image-based features for the diagnosis of other diseases where clinical examination is not adequate. Furthermore, it can be applied to other areas such as image-based automated inspection on industrial products such as wood and steel welds, and for computer vision for the navigation of robots to enable the identification of objects of interest on images with noise.

1.5. Dissertation Outline

The remaining chapters of the dissertation are organized as follows: Chapter 2 introduces pelvic organ prolapse and current diagnosis techniques. Chapter 3 discusses the state-of-the-art on the diagnosis of POP using MRI, automated object localization, medical image segmentation, and classification systems. Chapter 4 provides details about the proposed automated multi-bone localization technique on MRI. Chapter 5 presents the structure of the bone segmentation method. Chapter 6 presents the prediction model for the diagnosis of POP while Chapter 7

provides the summary and future work, summarizing the major findings and contribution of this dissertation.

Chapter 2

Pelvic Organ Prolapse and its Diagnosis

This chapter introduces the anatomy of the female pelvic floor, types of pelvic organ prolapse, and current diagnosis techniques.

2.1. Anatomy of the Female Pelvic Floor

Pelvic organ prolapse (POP) is a serious health problem affecting many women. POP occurs when the pelvic floor organs such as bladder, rectum, small bowel and uterus drops from the normal position towards the vaginal wall. There are different types of prolapse cases based on the affected organs such as cystocele (bladder), rectocele (rectum), and enterocele (small bowel). Pelvic Organ Prolapse-Quantification (POP-Q) system is a quantitative measurement of site specific points that is normally used for the clinical evaluation of POP. Medical imaging techniques are also used for diagnosis of POP when there is no clear evidence during the clinical examination using POP-Q.

The main components of the female pelvic floor are the pelvic bone, rectum, bladder, uterus, vagina, levator ani muscle and small/large bowel as shown in Figure 2.1. Details of each component are presented in the following sections.

The rectum is about 6 to 8 inches long and is the final portion of the large intestine leading into the anal canal. The main function of the rectum is to act as a temporary storage site for fecal matter before it is eliminated from the body through the anal canal.

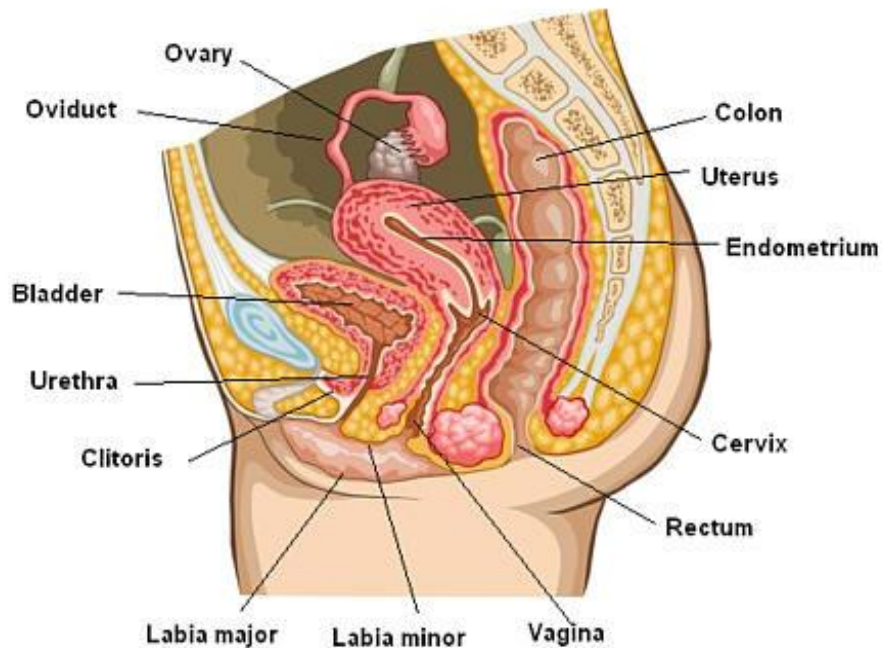


Figure 2.1: Female pelvic floor structure, sagittal view. ©2014 Free-Ed.Net

The pelvis is a bone structure that connects the base of the spine to the upper end of the rear legs, and it consists of several bones such as ilium, ischium, pubic bone, coccyx, and sacrum. The main functions of the pelvis are to carry the weight of the upper body when sitting and standing, and to carry over that weight from the axial skeleton to the lower appendicular skeleton when standing and walking.

The bladder is an organ that collects urine evacuated by the kidney. When the bladder is empty, it is about the size and shape of a pear.

The uterus is a hollow muscular organ located in the female pelvis between the bladder and rectum. The main function of the uterus is to maintain the developing fetus prior to birth.

The vagina is an elastic, muscular canal with a soft, flexible lining that is located in front of the rectum and behind the bladder. It has two main functions: childbirth and sexual intercourse.

The levator ani muscle is the main muscle in the pelvic floor and has a complex shape. It is composed of different muscles such as pubovaginalis, coccygeus and pubococcygeus. The maintenance of continence is one of the levator ani muscle's role and damage or weakening of levator ani muscle is considered one of the main causes of POP [17].

Intestine is a long and continues muscular tube which extends from the stomach to the anus. Food and the products of digestion pass through the intestine, which is divided into two sections called the small intestine and the large intestine. Small intestine absorbs the most of the nutrients from food and drink. The large bowel absorbs water from wastes, creating stool. As stool enters the rectum, nerves there create the urge to defecate.

2.2. Types of POP

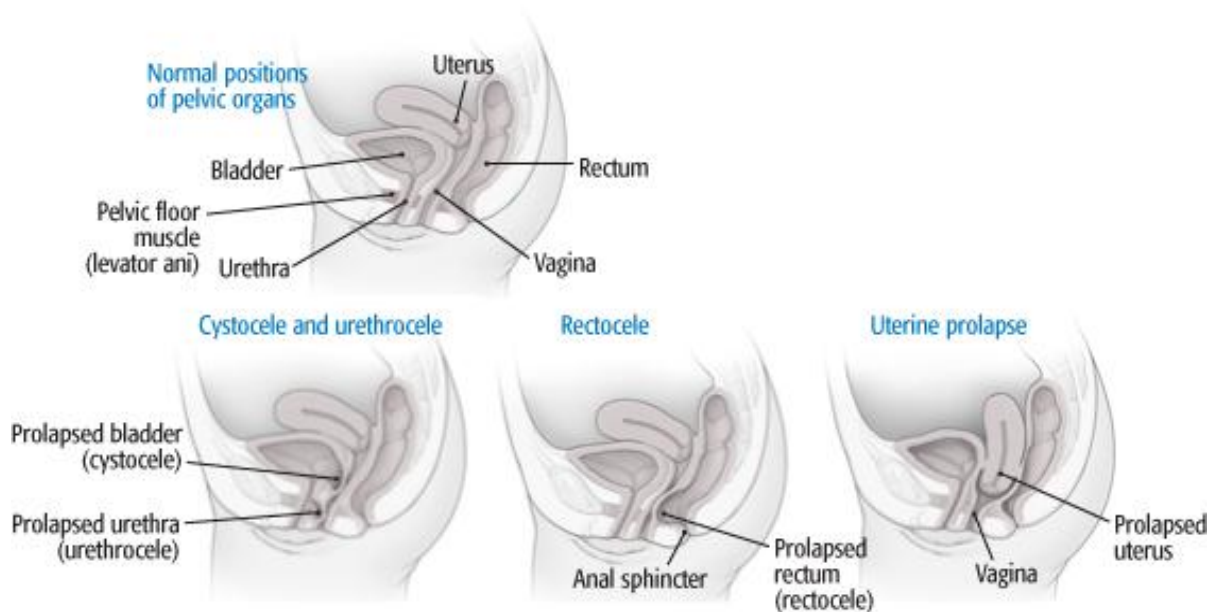


Figure 2.2: Types of pelvic organ prolapse. ©2014 Scott Leighton, CMI, medicusmedia.com

There are different types of POP depending on the organ affected as seen in Figure 2.2. Cystocele is the most common prolapse case and it occurs when the bladder drops from its

original position into the front wall of the vagina. A rectocele is defined as an outpouching of the rectum into the vagina caused by a weakening of the rectovaginal septum. An enterocele is defined as a peritoneum-lined sac with abdominal contents (usually small bowel and/or omentum) that herniates down between the vagina and rectum. This occurs when there is a separation of the rectovaginal septum fascia from the vaginal cuff. Enterocele often occurs with vaginal vault prolapse where the top of the vagina (vaginal vault) drops. Vaginal vault prolapse occurs most often in women who have had a hysterectomy (uterus removal operation). Uterine prolapse is defined as a hernia of the uterus into the vagina.

2.3. Clinical Diagnosis of POP

POP diagnosis begins with a physical examination of the pelvic floor organs. The physicians also ask several questions about medical and family history of the patient and the symptoms. Tests used during physical examination of POP includes: Cotton swab test, bladder function test, and pelvic floor strength test. In the cotton swab test, a small cotton-tipped applicator lubricated with anesthetic gel is inserted into the urine tube and the patient is asked to strain. The applicator indicates loss of support to the urethra. The bladder function test measures the bladder's ability to store and empty urine. It helps the physicians to determine the most appropriate type of surgery for bladder or urethral prolapse. In the pelvic floor strength tests, the physicians test the strength of the pelvic floor muscles and ligaments that support the vaginal walls, uterus, rectum, urethra and bladder.

POP is also diagnosed through clinical examination using the Pelvic Organ Prolapse Quantification (POP-Q) system as seen in Figure 2.3, which is recommended by the International Continence Society (ICS) and is considered the gold standard for assessing POP [5]. POP-Q is a

site-specific system describing, quantifying and staging of pelvic organ descent during evaluation of POP. It provides a standard tool for gynecologists to document, compare and communicate the clinical finding of POP. The hymen acts as the fixed point of reference throughout the POP-Q system. There are 6 points measured at the vagina with respect to the hymen to create a topographic map of the vagina- Aa, Ap, Ba, Bp, C, D and three distances- gh, pb, and tvl as seen in Figure 2.3 [18]. Each point is measured in centimeters above the hymen and below the hymen with the plane of the hymen being defined as zero. Persu et al. stated that:

“There are three reference points anteriorly (Aa, Ba, and C) and three posteriorly (Ap, Bp, and D). Points Aa and Ap are 3 cm proximal to or above the hymenal ring anteriorly and posteriorly, respectively. Points Ba and Bp are defined as the lowest points of the prolapse between Aa anteriorly or Ap posteriorly and the vaginal apex. Anteriorly, the apex is point C (cervix), and posteriorly is point D. In women after hysterectomy, point C is the vaginal cuff and point D is omitted. Three other measurements are taken: the total vaginal length at rest (tvl), the genital hiatus (gh) from the middle of the urethral meatus to the posterior hymenal ring, and the perineal body (pb) from the posterior aspect of the genital hiatus to the mid-anal opening” [19].

Points above the hymen are negative numbers, points below the hymen are positive numbers, and all measurements except total vaginal length (tvl) are measured at maximum valsalva (straining maneuver) to observe the movement of the pelvic organs from rest to maximum strain. These anatomic points can then be used to determine the stage of the prolapse based on Table 2.1 and Table 2.2.

For example, the leading point of prolapse is upper posterior vaginal wall, point Bp (+5). Point Ap is 2 cm distal to hymen (+2) and vaginal cuff scar is 6 cm above hymen (-6). Cuff has undergone 2 cm of descent because it would be at -8 (total vaginal length) if it were properly supported. This represents stage III Bp prolapse (rectocele) as seen in Figure 2.4.

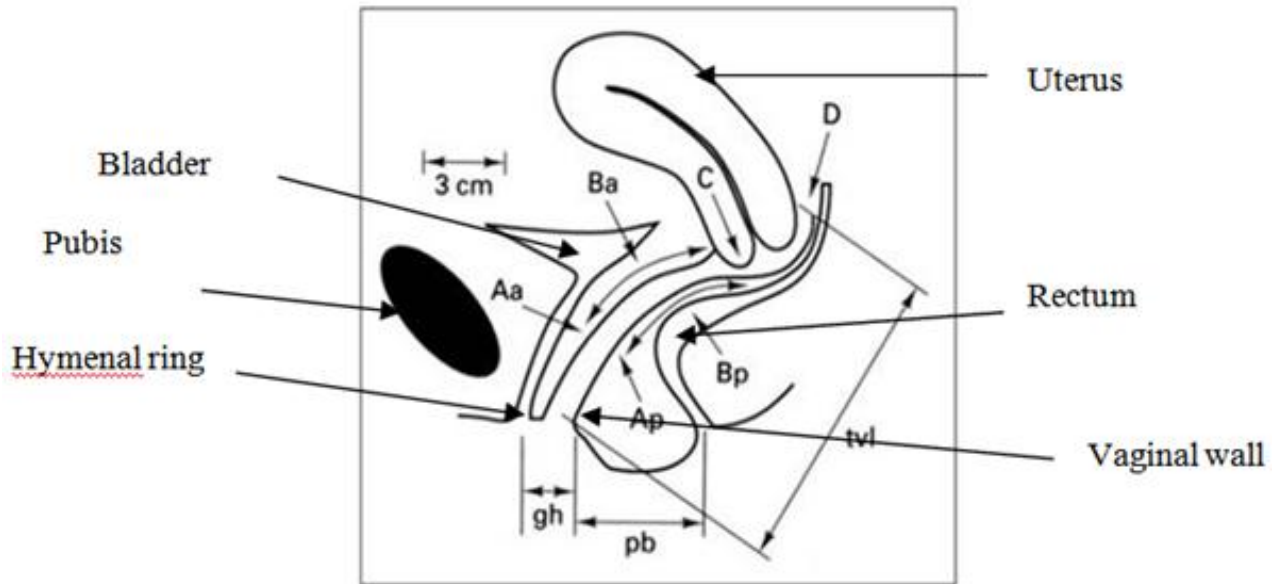


Figure 2.3: Points and landmarks for POP-Q system examination

Table 2.1: Pelvic organ prolapse quantification (POP-Q) system

Point	Description	Range of values
Aa	Anterior vaginal wall 3 cm proximal to the hymen	-3 cm to +3 cm
Ba	Most distal position of the remaining upper anterior vaginal wall	-3 cm to +tvl
C	Most distal edge of cervix or vaginal cuff scar	
D	Posterior fornix (N/A if post-hysterectomy)	
Ap	Posterior vaginal wall 3 cm proximal to the hymen	-3 cm to +3 cm
Bp	Most distal position of the remaining upper posterior vaginal wall	-3 cm to + tvl

Table 2.2: Pelvic organ prolapse stages

Stage 0	No prolapse is demonstrated
Stage 1	The most distal portion of the prolapse is more than 1 cm above the level of the hymen
Stage 2	The most distal portion of the prolapse is 1 cm or less proximal or distal to the hymenal plane
Stage 3	The most distal portion of the prolapse protrudes more than 1 cm below the hymen but no farther than 2 cm less than the total vaginal length
Stage 4	Vaginal eversion is essentially complete.

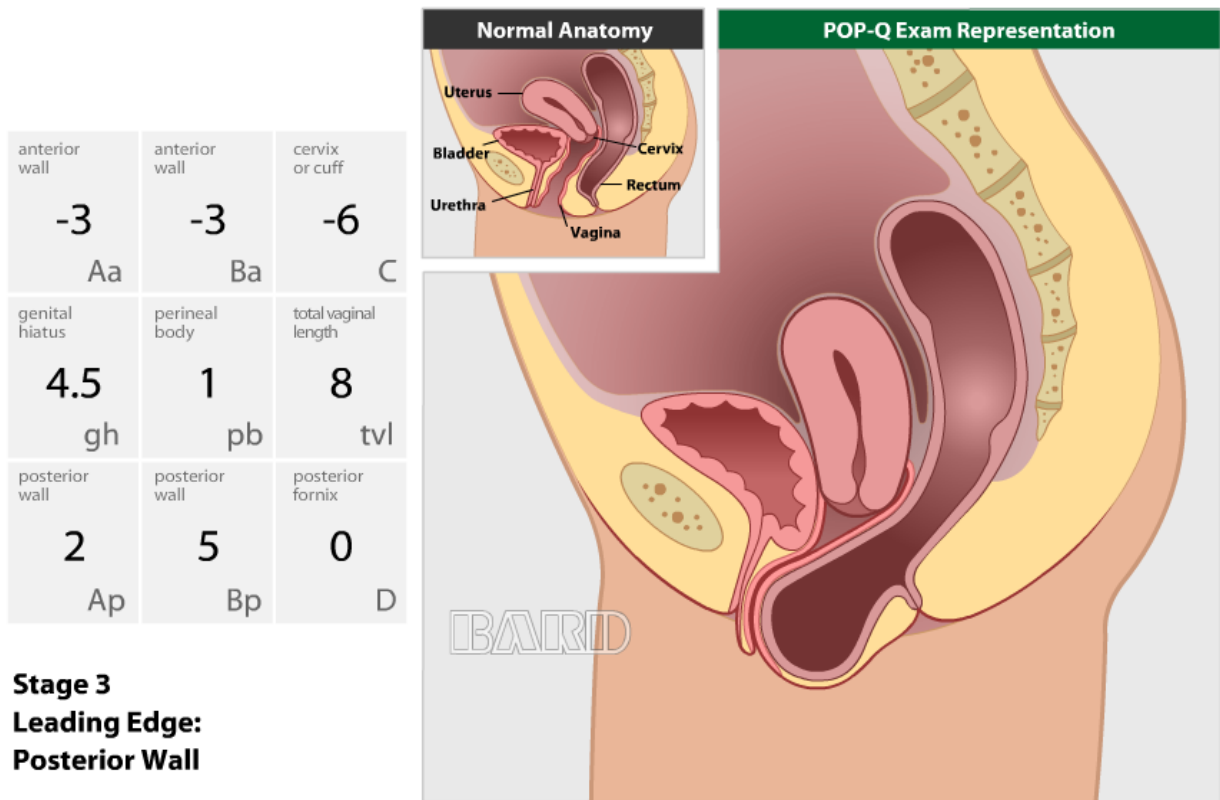


Figure 2.4: Stage 3 leading edge: posterior wall prolapse. Illustrations ©2014 Tim Peters and Company, Inc. All Rights Reserved. Developed in consultation with Patrick Culligan, MD. Morristown, NJ

2.4. Medical Imaging Techniques for Diagnosis of POP

Medical imaging modality is a system that uses an imaging technique to detect different physical signals arising from a human body to produce images. Some of these modalities use ionizing radiation with sufficient energy to ionize atoms and molecules within the body, and others use non-ionizing radiation. Ionizing radiation in medical imaging comprises x-rays and γ -rays, both of which need to be used prudently to avoid causing serious damage to the body and to its genetic material. Non-ionizing radiation, on the other hand, does not have the potential to damage the body directly and the risks associated with its use are considered to be very low. Examples of such radiation are ultrasound, high-frequency sound, and radio frequency waves.

The most popular imaging techniques that are used for diagnosis of POP are computed tomography (CT), X-Ray (ionizing radiation), ultrasound and magnetic resonance imaging (MRI) (non-ionizing radiation) as seen in Figure 2.5.



(a) (b) (c)
Figure 2.5: The most popular imaging techniques. (a) Ultrasound, (b) X-Ray, (c) MRI

Computerized Tomography (CT) is one of the noninvasive medical imaging techniques used for diagnosis and treatment of medical conditions. CT scan is frequently used for internal organs, soft tissue, bones, and blood vessels since it provides clearer details than regular x-ray exams to diagnose medical conditions such as cancers, cardiovascular disease, and musculoskeletal disorders. The main concern with CT imaging is to use minimal radiation without affecting the image quality. High dose radiation creates higher contrast resulting in higher quality image but it is also associated with increased risk of cancer. On the contrast, low dose of radiation results in noisy images with low contrast.

X-ray is another medical imaging technique that provides imaging of body structures, particularly of bones. X-ray beams pass through the body and are absorbed by each part of the body differently depending on the density of the body structure.

Ultrasound, also called sonography, is a non-invasive real-time imaging technique that involves using a transducer and gel to expose the body to high frequency sound waves that are

more than 20,000 cycles per second. Ultrasound imaging is a safe and painless procedure that does not use ionizing radiation. There are no known harmful effects on human body. It is easy to use and less expensive than the other imaging techniques. Since it is a real-time procedure, they are used to show the structure of the body and internal organs as well as blood flowing through blood vessels. Ultrasound diagnosis helps physicians to monitor the changes in kidneys, bladder and the muscles around the anus that do not show up in X-ray images.

Magnetic resonance imaging (MRI) is another non-invasive medical imaging technique that is widely used in medicine to visualize the internal structure of the body to create a detailed, 3D image of the pelvis. Unlike x-ray imaging and computed tomography (CT) scans, MRI does not depend on ionizing radiation. Magnetic resonance imaging (MRI) uses radio frequency pulses to create detailed pictures of soft tissue and organs, bone structures and any other body structures. MRI is used to monitor and evaluate pelvic floor organs including bladder, small bowel, and rectum as well as the reproductive organs such as the uterus. MR images of the soft-tissue structures and organs are better in identifying and characterizing diseases than other imaging methods. This detail makes MRI an invaluable tool in early diagnosis and evaluation of pelvic floor organs movements. The MRI examination poses almost no risk to the average patient when appropriate safety guidelines are followed.

Dynamic MRI is an important medical imaging modality to monitor changes in soft tissue and organs of pelvic floor structure over time. It comprises a series of data acquisitions in the spatial frequency domain from which a time series of images is formed. Dynamic MRI imaging of the pelvic floor offers several advantages over conventional imaging techniques by providing a global, dynamic assessment of the pelvic floor with associated interactions of pelvic organs (evaluation of all three compartments simultaneously), superior intrinsic soft-tissue

contrast with multiplanar imaging capability, and the absence of ionizing radiation. This is especially important given the inaccuracies of the clinical examination. In addition, Dynamic MRI can also help monitor the muscular and ligamentous pelvic floor support structures and detecting incidental findings.

During the analysis of dynamic MR images, anatomical landmarks are identified manually in the midsagittal plane to create the reference lines that are used to measure POP in each compartment. Although several reference systems exist, two of the more commonly used reference lines for measuring POP are shown in Figure 2.6: pubococcygeal line (PCL), and mid-pubic line (MPL). Distances are measured from PCL and MPL to the bladder neck, cervix, and anorectal junction on the images to determine the severity of prolapse as shown in Figure 2.6. As shown in the figure, the grading of rectocele is based on the measured length of the M-Line, which is defined as the perpendicular line with respect to the PCL until the inferior margin of the organ of interest. The rectocele grading based on the M-Line's length is as follows: negative, < 1 cm; mild, 1-2cm; moderate, 2-4cm; or severe, >4cm [20].

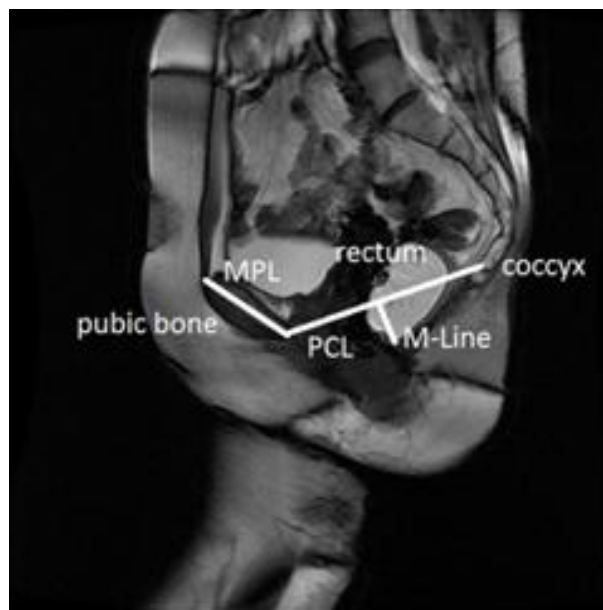


Figure 2.6: Commonly used reference lines for grading pelvic organ prolapse

2.5. Summary

In this chapter, the anatomy of the female pelvic floor, types of pelvic organ prolapse, and current diagnosis techniques of POP were introduced. POP is normally diagnosed through clinical examination but its accuracy is limited and has been found to be in disagreement with surgical findings in many cases. Dynamic MR imaging of the pelvic floor has become an increasingly useful tool in the assessment of POP and functional disorders of the pelvic floor since it enables evaluation of all compartments simultaneously. However, the MRI pelvic floor measurement process is time-consuming and subjective. Therefore, there is a need for automating the pelvic floor measurement process by locating anatomical structures and identifying their corresponding landmarks. The following chapter presents the state-of-the-art on clinical diagnosis of POP, medical image localization and segmentation, and classification systems for medical diagnosis.

Chapter 3

Literature Review

This chapter provides an overview of previous work in the areas of POP diagnosis techniques, automated organ localization, bone segmentation, classification systems for disease diagnosis, and feature selection techniques.

3.1. Pelvic Organ Prolapse Diagnosis using MRI

Currently, dynamic MR images are analyzed based on reference lines to determine the stages of POP. The most commonly used reference lines for measuring POP are pubococcygeal line (PCL), and mid-pubic line (MPL). The PCL is determined by the inferior border of the pubic bone and the last visible coccygeal joint while the MPL is a midsagittal long axis of the symphysis pubis and extends through the level of the vaginal hymen [21, 22]. Distances are then measured from PCL and MPL to the bladder neck, cervix, and anorectal junction on the images when the patient is at rest and under maximum pelvic strain. Based on these distances, the severity of prolapse can be graded as mild, moderate, or severe [13].

Previous studies have shown that the use of the PCL as a reference line on MR imaging can help in assessing the clinical stages of POP for the anterior and the apical compartment [23, 24]. For the posterior compartment, the diagnosis of rectocele has been diverse. It has been reported that only 51% of rectocele were correctly identified with physical examination [25]. Fauconnier et al. compared the clinical measurement points with MRI anatomical landmarks, and found a good correlation in the anterior and apical compartment [26]. On the other hand, no

correlation was found for the posterior compartment. Broekhuis et al. shows the high agreement in the anterior and apical compartment that clinical assessment and dynamic MR imaging are interchangeable. However, the agreement between these two methods in the posterior compartment is lower. Therefore, posterior prolapse remains the most difficult type of prolapse to diagnose [11]. Pannu et al. [27] found a relationship between MRI and clinical measurements in identifying POP using both the pubococcygeal line (PCL) and the midpubic line (MPL) in the anterior compartment. However, there was no significant difference in agreement using the MPL or PCL, therefore either line can be used on MRI. Cortes et al. [28] performed a correlation analysis between the clinical examination and the MRI data for vaginal apex prolapse using MPL and they found poor correlation between clinical examination and MRI. They suggested a complementary diagnostic tool to identify complex vaginal apex prolapse. Lienemann et al. [24] investigated which reference lines on functional cine-magnetic resonance imaging correlated best with the clinical diagnosis, which led to the conclusion that POP descent cannot be described using only one reference line and agreement has not been presented. Robinson et al. [29] demonstrated a prediction model for POP by using artificial neural network (ANN) and clinical data only. It was found that 20 variables made the largest contributions to the model such as age, gravidity, parity, and the number of vaginal deliveries. In the study, only clinical data was used and no image data was used.

The main disadvantage of these studies is that they have not been completely tested and proven on large image samples given that the MRI pelvic floor measuring process remains a time-consuming and subjective procedure. Moreover, because there is no standardized system for MRI measurements, these studies have led to incomplete and non-comparable data.

3.2. Medical Image Object Localization

The main goal of object localization algorithms is to estimate an object's approximate location on images to identify the object's center point, contour, or bounding box. Various approaches have been proposed for the automated localization of multiple organs such as heart, liver, spleen, lungs, kidneys and bladder on medical images using geometric methods, statistical atlas-based techniques, and supervised methods [3-10].

3.2.1. Geometric Methods

Geometric methods include template matching, and convolution techniques. The information about the objects is represented explicitly. The recognition can then be interpreted as deciding whether a given image can be a projection of the known model of an object. Geometrically meaningful features were used in [30, 31] for the segmentation of the aorta and the airway tree, respectively. Such geometric approaches often have problems capturing invariance with respect to deformations (e.g. due to pathologies), changes in viewing geometry (e.g. cropping) and changes in intensity. Techniques built upon "softer" geometric models with learned spatial correlations have been demonstrated to work well both for rigid and deformable objects.

3.2.2. Statistical Atlas-based Methods

Statistical atlas-based techniques enable the inclusion of high level information to the detection process in the form of shape priors. These techniques are normally performed on three steps: a registration step where the target image is aligned to the single or multiple atlases, a label propagation step where the labels are transferred from the atlases to the target, and a final

segmentation step in which transferred labels are used to segment the target image. The registration process consists of two separate steps: a global registration followed by a local non-rigid registration. Since it involves a complex discrete optimization problem, this process is often computationally expensive, and sensitive to initialization. Multi-class atlas provides better results since it enhances the variation of the atlas, but it still has the same drawback as single atlas. Atlas-based techniques have been applied to the brain [32], multi-organ [33, 34], head and neck [35] and heart [36].

3.2.3. Supervised Methods

For supervised methods, discriminative classification algorithms such as AdaBoost [37], Probabilistic Boosting Trees and random decision forest have been applied to the automatic detection of tumors [38, 39], pulmonary emphysema [40], organs in whole-body scans [41] and brain [42, 43]. In these classification-based algorithms, local and global image features are used to discriminate the desired objects from an image. Local edge orientation and local velocity in an image sequence can be used as local image features while contour representation, shape descriptors and texture features are used as global image features.

Among supervised methods, there has been an increasing interest in regression-based approaches for anatomical structure localization, since organs and tissues in the human body have known relative arrangement. Zheng et al. [44] proposed an approach called marginal space learning (MSL) that uses a set of classifiers based on probabilistic boosting tree (PBT) to predict the position, position-orientation and full 3D pose. In [45], the authors further expanded this idea to non-rigid marginal space learning using statistical shape models. Zhou et al. [46] introduced an approach based on boosting ridge regression to detect and localize the left ventricle (LV) in

cardiac ultrasound 2D images. Criminisi et al. [47] proposed regression forests to predict the location of multiple anatomical structures in CT scans. Cuingnet et al. [48] presented an improved regression forest by adding a refinement step to the detection process to find kidneys in CT scans. These methods use the difference in mean intensities to locate the bounding boxes of the anatomical structures on the images. However, considering only intensity levels is not sufficient for the localization of anatomical structures such as bones on MRI.

3.3. Segmentation of Bone Structures on MRI

Medical images differ from normal digital images since they have poor contrast and natural noise. This limits the use of current segmentation approaches for normal digital images as they cause weak segmentation results. Medical image segmentation has become increasingly important in automating the identification of structures of interest for diagnosis, localization of pathology, treatment and surgical planning. It has been successfully applied to identify a tumor, cell, bone and diagnosis of heart and lung diseases. Medical image segmentation techniques are influenced by objects' boundaries, homogeneities and shapes. The object's boundaries and homogeneities are image based and affected by some specific disturbances like noise. They are also highly dependent on the image modality techniques. For instance, bones have more visible boundaries in computed tomography (CT) but poor boundaries in magnetic resonance images (MRI). On the other hand, soft tissues such as organs are better observed on MRI than CT. Medical image segmentation algorithms are divided into two main methods: model-free based algorithms and model-based algorithms.

3.3.1. Model-Free Based Algorithms

Model-free based segmentation methods, also called unsupervised segmentation methods, are based on local image properties such as intensity value, gradient magnitude, and textures. Image statistics tools such as histogram, mean, variance, and entropy can be used in this kind of segmentation. The following methods are the most frequently used model-free techniques: thresholding, image feature-space clustering, region based and boundary based. The simplest image segmentation method is the thresholding method, which is used very commonly for segmenting gray scale images [49, 50]. The image feature-space clustering method is a multi-dimensional extension of the thresholding segmentation, and it segments an image by grouping similar pixels into one group [51]. Although thresholding and image clustering techniques are effective when the intensity levels of the objects fall outside the levels in the background, their disadvantage is that they do not incorporate the spatial characteristics of the image data. The region based image segmentation approaches such as region growing, region splitting, region merging, or hybrid model group spatially connected pixels into homogeneous groups [52]. Region based segmentations [53] are based on the principle of homogeneity. Pixels that have the similar properties are grouped together as a homogenous region. An advantage of the region based segmentation is that segmented groups are guaranteed to be homogeneous spatially. It is also possible to separate groups at multi-scales using region-based approaches and spatial information. Image segmentation can also be obtained by boundary based techniques. One of the most common boundary based approach is edge detection which is an important task in image processing and many different approaches have been proposed [54-56]. Edge detection techniques are very effective and easy to apply to any image. However, these techniques usually fail with very noisy images such as MRI, CT, or X-Ray. In recent years, wavelet transformation

based edge detection techniques have been proposed medical image processing [57]. Zhang and Bao [58] showed that the scale multiplication provides better results than either of the two scales, especially on the localization performance. Bao and Zhang [54] applied the scale multiplication technique to enhance the canny edge detection algorithm. Chao et al. [59] performed the wavelet analysis with Markov Random Field for segmentation of regions of interest on the MRI based on Maximum Entropy Theory. Flores-Tapia et al. [60] performed MRI prostate segmentation based on wavelet multi-scale products flow tracking.

3.3.2. Model Based Algorithms

Model based segmentation approaches build a model representing an object using a training set and later match the model to unknown image data. During the matching process, the model's shape and additional properties are varied to improve the match iteratively. Some typical model based segmentations with locally modeled shape prior technique is active contour or snake [61].

An active contour detects specified properties of an image and can dynamically fit to the edges of a structure by minimizing an energy function. There are two types of energy that control the segmentation: the internal energy and the external energy. The internal energy provides the rigidity and the tension of the contour and defines how smooth and flexible the snake is. The internal energy therefore is a local shape prior, which determines how the object to be segmented should locally look like. The image driven part of the segmentation method is given by the external energy. It determines what kinds of image features attract the contour. Successful applications have been reported on segmentation of the anatomical structure such as brain [62], and lung [63]. However, active contour has several disadvantages. First, the method depends on

the initial positions of the contour or surface, which needs to be carefully placed by the user to avoid getting trapped in local minima. Secondly, the method depends on the quality of the images having drawbacks when applied to low contrast images. Another drawback is that the snake is not able to fully adapt to the structure in some parts while in other parts it may be already too flexible and leak into neighboring structures. Lastly, the method is complicated and requires a lot of computation during iterations.

Globally modeled shape prior techniques use the global shape knowledge for segmentation. Geometric model based segmentation is the most widely and successfully used segmentation technique in this category. The shape is represented by geometric objects like point clouds, polygonal surfaces, simplex meshes and B-spline representations. Based on the chosen shape representation, an initial shape is created to be used for segmentation. For example, the initial shape, also called template, can be the mean shape of some representative shapes of the anatomical structures to be segmented. The model is then placed in the image directly on the structure to be segmented. Then, similar to local prior shape methods, image features like edges are searched in the image by external energy and integrated into an image term. Usually, image features are used to describe the boundary of the structure to segment.

There are many ways to model a group of template shapes. The simplest way is to define a single object to be the template if the shape variance of the structure to segment is not high. However, for anatomical structures that strongly vary between individuals, a single template shape is not sufficient. For such structures, a representative set of template shapes is necessary. However, using many templates also increases the complexity of the decision process of whether the current model is similar to the template shape set. Statistical shape modeling has been first proposed by Cootes et al [64] and has been applied to segment the liver in CT [65, 66], the heart

and heart chambers in CT [67, 68], and the prostate in MRI [69]. Because geometric model based segmentation depends on knowing the expected shape of the structure to segment a-priori, it is less suited for segmenting objects that can have arbitrary shapes like soft tissues, organs and tumors.

Traditionally, MRI has been used to study soft tissues, whereas computed tomography (CT) scanning has been associated with imaging of hard tissues such as bones. However, the use of MRI for imaging bone has become more commonplace due to the lack of ionizing radiation. Many methods have been proposed for the segmentation of bones on MRI such as region growing approaches, medial models, active shape models, general deformable models (live-wire, active contour or active surface models), clustering methods, and graph-based approaches. Lorigo et al [70] used texture-based geodesic active contours to perform segmentation of knee bone. Fripp et al [71] used three-dimensional active shape models initialized by affine registration to an atlas and achieved good segmentation results of knee bone. Bourgeat et al [72] used features extracted from the phase of MR signal to improve texture discrimination in the bone segmentation. Graph-based approaches (graph-cuts) have been highly successful in obtaining globally optimal solutions for a class of discrete optimization problems.

Schmid et al. [73] presented an approach based on physically-based deformable models and prior shape knowledge for the segmentation of femur and hip bones on MRI. Yin et al. [74] used graph cuts for knee-joint bone and cartilage segmentation starting from initial segmentations that are formed by adapting single-object statistical shape models of the knee bones.

Recently, segmentation techniques based on statistical classification have been used for bone segmentation on MRI [72, 75]. These techniques group pixels or voxels based on

distinguished features such as intensities, gradients and texture. Simple intensity-based features do not provide successful segmentation results because different tissues have overlapping image intensity values. Bourgeat et al [72] used Gabor filter features extracted from the phase of MR signal to improve texture discrimination in bone segmentation. Van Ginneken et al [75] combined texture based classification with the anatomically valid shape information of the chest structure to constrain the segmentation. Although these methods present promising results, the main drawbacks are high computation time, initialization sensitivity, definition of many parameters, and lack of leak detection processes.

3.4. Classification Systems and Feature Selection for Medical Diagnosis

3.4.1. Classification Systems

Data mining techniques have become very popular in enhancing medical diagnosis by exploring the hidden patterns in the medical data sets. They have been widely used for diagnosis of illnesses such as diabetes [76], stroke [77], cancer diagnosis [78], and heart disease [79]. Data mining techniques can be classified into two categories unsupervised (description) and supervised (prediction). The description techniques aim to find a pattern and association on the whole data set while prediction techniques seek to foretell some response of interest.

Supervised classifications are one of the most useful data mining techniques in health care. Such techniques include decision tree [80], artificial neural networks [79, 81], support vector machine [82], and the naïve Bayesian classifier [83]. A number of classification methods have been applied using anatomical MRI data to diagnose subjects as having psychiatric illnesses and tumor [84-88]. Hinrichs et al. [89] and Zhang et al. [90] used data from both anatomical MRI and positron emission tomography (PET) to classify subjects with Alzheimer's disease. A

support vector machine (SVM) was used to learn the decision boundary in a feature space, and the performances of the classifier were validated using a leave-one-out approach. Twellmann et al. [91] applied a classification method to detect suspicious cancer lesions in dynamic MRI data. In the study, cancer cells were selected in a supervised fashion and fed to a SVM, which was trained to perform a binary classification between benign and malicious cells. Pena-Reyes and Sipper [92] used fuzzy modeling and cooperative coevolution to classify the entire Wisconsin breast cancer database. Setiono [93] used a Feed forward Neural Network Rule Extraction Algorithm for breast cancer diagnosis.

The SVM algorithm works very well with high dimensional data and avoids the curse of dimensionality problem. SVM has shown to be very successful in the diagnosis of various diseases due to its strong theoretical foundation and accuracy results. In [94], four different methods: combined neural network, probabilistic neural network, recurrent neural network and SVM were applied to breast cancer diagnosis where SVM achieved the highest classification accuracy of 97.36%. In [82], a least square SVM was used for the diagnosis of cancer resulting in a 98.53% accuracy. Akay [95] achieved a 99.51% classification accuracy for the diagnosis of cancer using a SVM-based method combined with F-score technique.

The classification framework involves two step processes: the first step is to construct a classification model based on the data, and the second step is to apply the model to test examples. Classification techniques can be also divided into two main categories regarding their training processes: eager learners and lazy learners. The eager learners are designed to learn a model that maps input variables to the class as soon as the training data becomes available. On the other hand, lazy learner techniques memorize the entire training data and perform classification only if the variables of a test set exactly match one of the training set. The only

drawback of the lazy learners is that some test records may not be classified because they do not match any training example.

3.4.2. Feature Selection for Medical Diagnosis

In classification problems, the feature selection process is very important and has a considerable impact on the classification results. Given that available raw medical data is widely distributed and heterogeneous, this data needs to be collected in an organized form to identify the significant features, eliminate the irrelevant features and build a good learning model for the classification. Feature selection approaches can be divided into two main categories: filter based and wrapped based. In the filter based approaches, all features are scored and ranked based on statistical criteria and then features with higher ranking are selected. These methods include t-test [96], chi-square [97], mutual information [98], Pearson correlation coefficient [99] and principal component analysis [100]. On the other hand, in the wrapped methods, the feature selection is wrapped in a learning algorithm and it is applied to subsets of features and tested based on prediction accuracy to determine the feature set quality. The most common wrapped algorithms are sequential forward selection (SFS) and sequential backward selection (SBS) [101, 102]. Stochastic algorithms have been also proposed to select subset features by solving large scale problems such as genetic algorithm [103], practical swarm optimization [104] and simulated annealing [105]. Recently, several authors proposed hybrid approaches taking advantages of both filter and wrapper methods. Examples of hybrid algorithms include t-statistics and a GA [106], a correlation-based feature selection algorithm and a genetic algorithm [107], and mutual information and a GA [108].

3.5. Current Challenges to be Addressed in the Proposed Research

The current research challenges for the diagnosis of POP in MRI can be divided into two main groups: medical and engineering based. In terms of medical challenges, the currently used features have shown to be insufficient to identify the presence and stages of POP. This has led to results from clinical studies that disagree with surgical outcomes. Moreover, the extraction of these features is a time-consuming and subjective procedure. This has restricted the correlation analysis of MRI measurements with clinical information and surgical outcomes as well as the validation of newly proposed reference lines.

In terms of engineering based challenges, many of the features currently used for evaluation of POP are based on the identification of pelvic bone structures and their corresponding landmarks on dynamic MRI. However, bones are not easily identifiable from the soft tissue on MRI since fat tissues tend to have intensity characteristics that are very similar to the intensity of the bone structures. This constitutes a major challenge for current algorithms that tend to fail during bone localization and segmentation by erroneously classifying soft tissue as bone. Moreover, most of the algorithms for structure localization on MRI are semi-automated requiring user input. Automated segmentation algorithms have been presented mainly for applications where boundaries are well defined [70, 71, 109, 110]. Therefore, the main challenges that remain for automated medical object identification are the large search space, numerous local minima, image inhomogeneity, and/or high computational cost.

Chapter 4

Multiple Bone Localization on MRI

This chapter introduces a model to automatically find the location of multiple bone structures on dynamic MRI. For the pubic bone, the model consists of the identification of keypoints and extraction of candidate regions using Harris corner detector and texture based classification. For the localization of coccyx and sacral promontory, a non-linear regression approach is presented using previously identified bladder, rectum, and pubic bone locations.

4.1. Overview of Multiple Bone Localization Model

In this study, the bone localization problem consists of finding the bounding boxes of the structures of interest as seen in Figure 4.1. A model is proposed that locates the bounding boxes of multiple bone structures on MRI using support vector machines (SVM) based classification and non-linear regression model with global and local information. The proposed scheme first identifies pelvic organs using k -means clustering and morphological opening operations. Then, it uses the spatial relationship between the organs and bone structures to estimate the locations of the structures. The pubic bone is located using the relative location between bones and organs, and texture information. Then, a non-linear regression model is used to predict the location of other bone structures whose local information is insufficient, such as sacral promontory and coccyx. The main contribution of this scheme is a new parameterization through non-linear regression approach for the multiple bone localization problems on MRI.

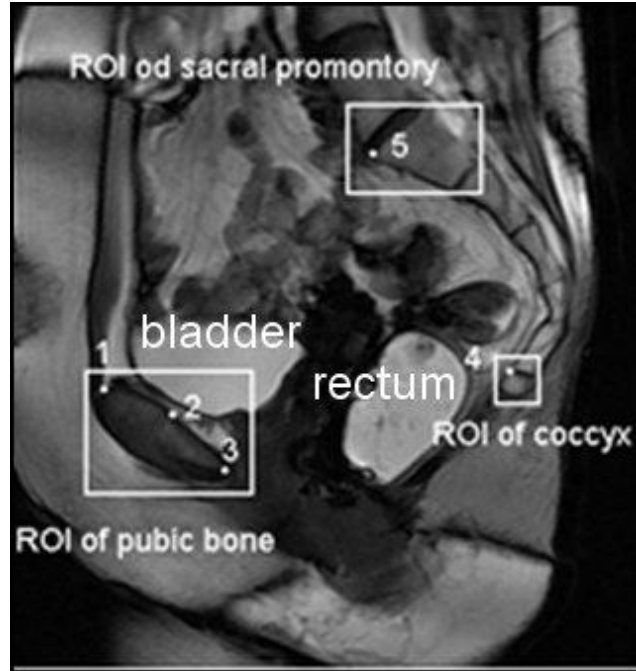


Figure 4.1: Regions of interest with their corresponding reference points

As shown in Figure 4.1, three regions of interest (ROIs) need to be located automatically that correspond to the pubic bone, sacral promontory, and coccyx, respectively. However, bones are not easily differentiable from soft tissues on MRI as their pixel intensities tend to be very similar. This is particularly true for bones located on the vertebra such as sacral promontory and coccyx. On the other hand, both the bladder and the rectum are visible as retrograde bladder/ureteral dye is injected during image capturing to enhance visualization. Therefore, the regions for both the bladder and the rectum have high intensity values on the MR images and can be used as contextual information to automatically locate the pelvic floor structures of interest. Based on these observations, our scheme is designed to localize the pubic bone first using both global and local information, and then use global information to localize the sacral promontory and coccyx.

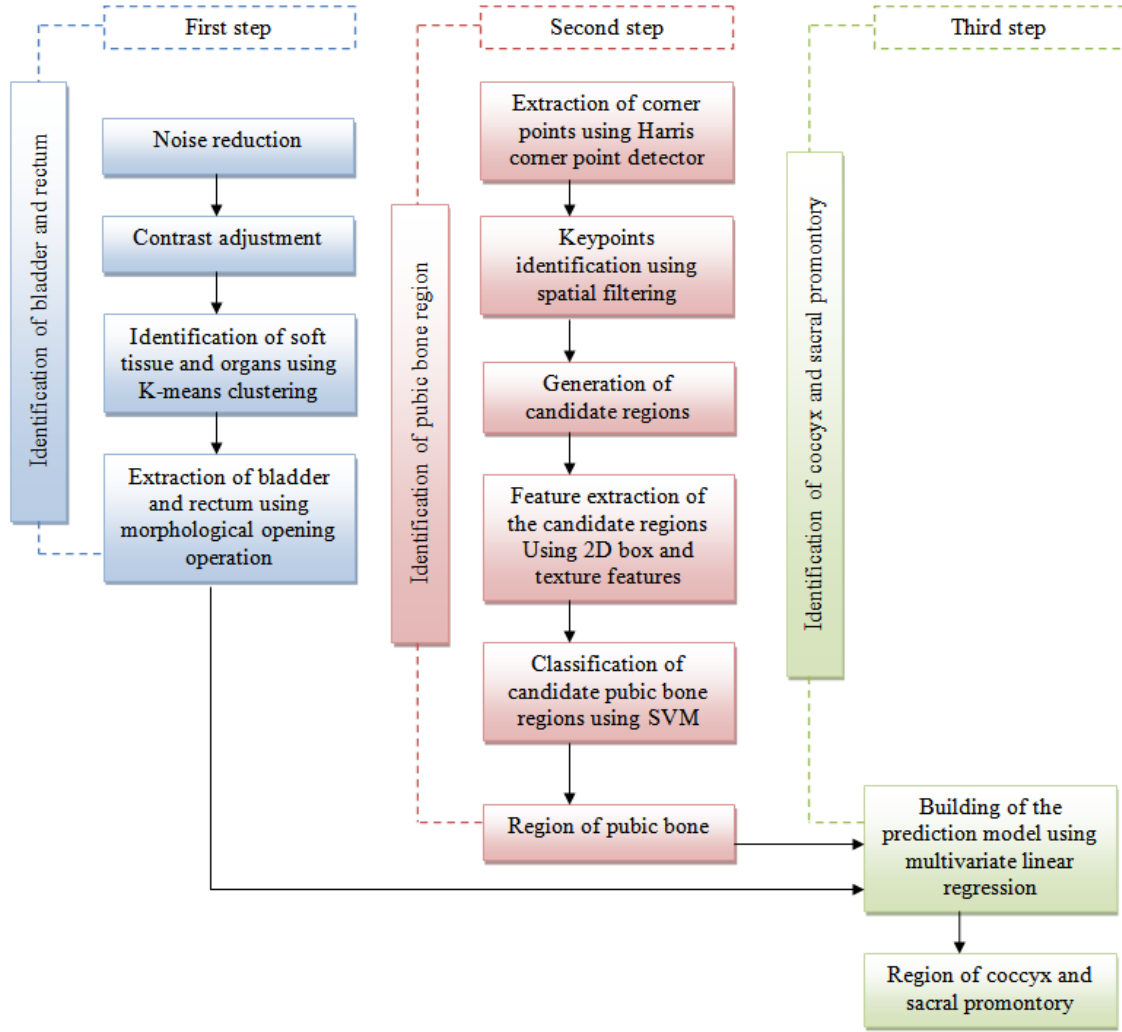


Figure 4.2: Overview of the proposed multiple bone localization method

Each bone region has specific characteristics so different approaches are needed to find these regions. For instance, the pubic bone region is located between the bladder and abdomen, which are high contrast regions while the coccyx and sacral are low contrast regions resulting limited visibility in midsagittal view of dynamic MRI. The location of the pubic bone can be found using both contextual and texture information based on the location of the bladder and rectum. On the other hand, the location of the sacral promontory and coccyx can be found using only contextual information based on the location of the bladder, rectum, and pubic bone.

The proposed method consists of three main steps: identification of bladder and rectum, identification of pubic bone region, and identification of coccyx and sacral promontory regions (see Figure 4.2). The first step starts with noise reduction and contrast adjustment of the images followed by clustering of the anatomical structures through bisecting K-means clustering using pixel intensities. K-means is convenient for medical images as the number of clusters (K) is usually known for particular regions of the human anatomy [111]. The anatomical structure can be divided into four sub-regions representing the organ and soft tissue, bone, cartilage, and background. The brightest regions represent the bladder and rectum since dye is injected before imaging to make these organs more visible for radiological examination. The regions (clusters) corresponding to the bladder and rectum are separated from the other clusters using morphological opening operation. In the second phase, the pubic bone region is localized based on “keypoints”, which are corner points on the input image that satisfy certain intensity and location constraints. Based on the identified keypoints, candidate bounding boxes of the pubic bone can be determined. The best bounding box that describes the pubic area is selected using support vector machines (SVM) with 2D box features. In the third phase, the coccyx and sacral promontory regions are localized using the location of the bladder, rectum and pubic bone via a non-linear regression model. The detailed description of the proposed scheme is as follows.

4.2. Dataset Description

MR images were obtained from a 3-Tesla GE system (General Electric Company, GE Healthcare, Buckinghamshire, UK) using an 8-channel torso phased-array coil with the patient in a modified dorsal lithotomy position (patient laying in the supine position with their knees slightly elevated and abducted under a support). Dynamic MRI of the pelvis was performed

using a T2-weighted single-shot turbo spin-echo (SSH-TSE) sequence in the midsagittal plane for 23-27 seconds with a temporal resolution of 2s (FOV 300×300 mm², slice thickness 3 mm, TR/TE 2,000/75 ms, 20 image sequences, in-plane resolution of 1.6×1.6 mm²). Subjects were coached, prior to imaging, on performance of an adequate valsalva maneuver (straining maneuver) to observe the movement of the pelvic organs from rest to maximum strain. The image data has been preprocessed to de-identify the images before applying the method.

4.3. Identification of Bladder and Rectum

The model uses the location of pelvic organs to predict the location of the pelvic bone structures. The first phase of the proposed scheme is to perform noise reduction by applying a 3 by 3 Gaussian kernel due to its computational efficiency. After noise reduction, contrast adjustment is performed to improve the contrast in the images by stretching the range of intensity values. Minimum and maximum values used for normalization are 0 and 255 respectively.

Given the clear visibility of the bladder and the rectum on dynamic MRI due to ureteral dye use, these two organs can be automatically identified to be used as contextual information for the localization of the bone structures. The ureteral dye helps to improve visualization of these two organs by increasing the contrast. A “bisecting K-means” algorithm is used to identify regions on the image and to overcome the initialization susceptibility of the basic K-means clustering algorithm. The idea is to obtain K clusters by first splitting the set of all points into two clusters. Then one of these clusters is selected for splitting and the process continues until K clusters are generated. In the study, the value of K is 4 because the region of the pelvic floor is divided into four sub-regions representing the bone, cartilage, soft tissue and organ, and background.

After identifying the four types of regions, the regions with the highest intensity are selected to locate the bladder and rectum regions. However, many regions with similar intensities to the bladder and rectum may be identified as shown in Figure 4.3 (b). To separate the bladder and rectum, size, homogeneity, and location constraints were incorporated. For size constraint, connected regions that have less than a specified number of pixels were removed using morphological opening operations. For homogeneity, it was observed that the bladder and rectum regions on MRI are homogeneous regions without internal holes. Therefore, the *Euler* number, which is a topological descriptor, was used to determine the number of holes inside the regions and to eliminate those regions with internal holes. Finally, as location constraint, the location of the bladder and rectum normally appear close to the center of the image so the search of these two organs was limited to the center of the image. The results of this process are shown in Figure 4.3 (c).

The mathematical description of this filtering operation to find the desired regions H (bladder and rectum) is shown below. R_l corresponds to the set of regions obtained after clustering.

$$H = \{ s_{min} < s_{R_l} < s_{max}, \phi_{R_l} = 1, d_{R_l} < r \ \forall R_l \in R \} \quad (4.1)$$

where s_{R_l} denotes the size of the l^{th} region in set R , which was obtained through bisecting K-means clustering, s_{min} and s_{max} are the minimum and maximum region sizes, respectively. ϕ_{R_l} is the specified *Euler* number which is 1. d_{R_l} denotes the distance between the centroid of the l^{th} region and the midpoint of the image, and r is the specified distance.

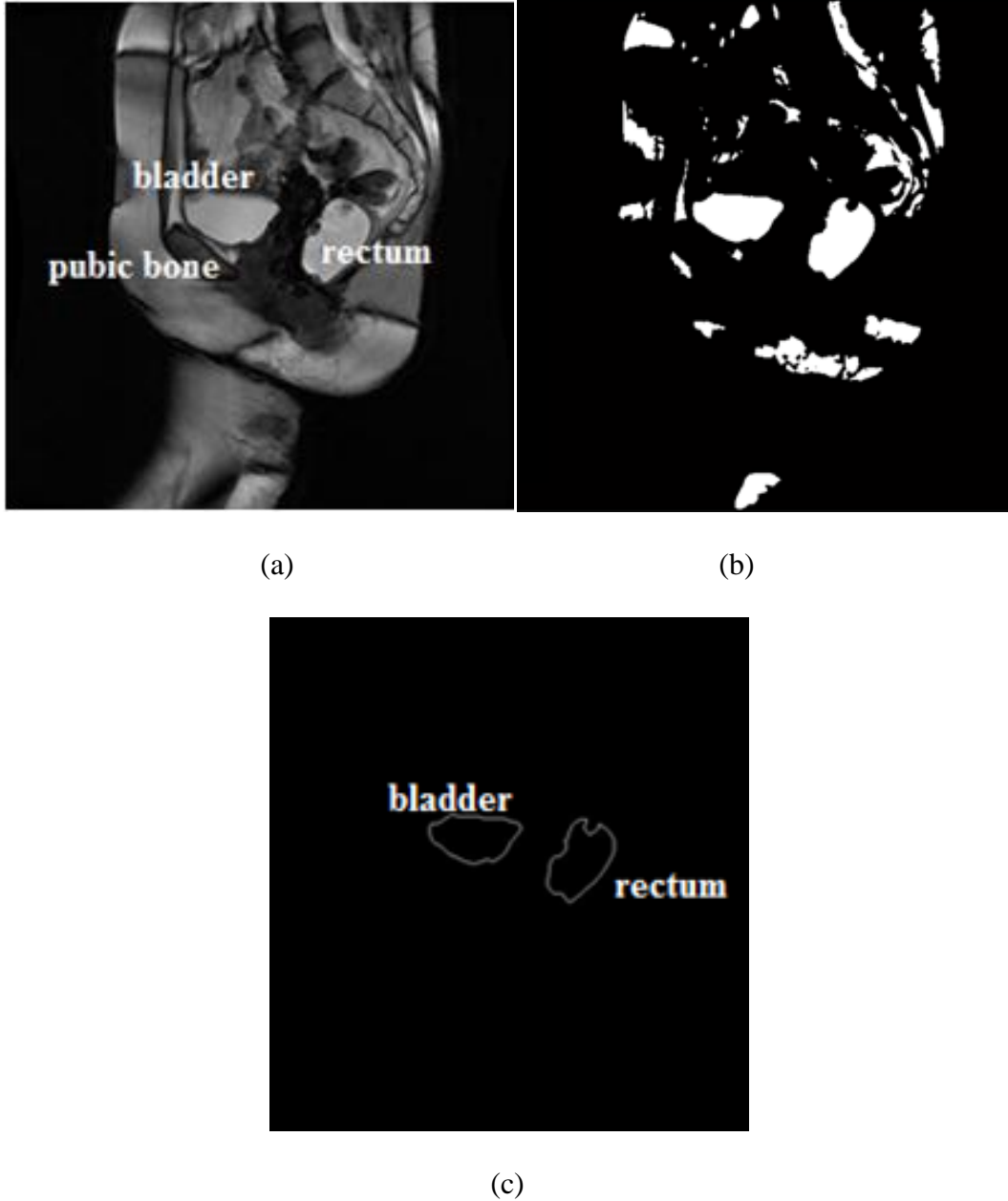


Figure 4.3: Illustration of bladder and rectum localization. (a) Input image, (b) Clustering with $k=4$, (c) Identified regions for bladder and rectum using shape and location constraints

4.4. Identification of Pubic Bone Region

4.4.1. Keypoints Extraction

After the locations for the bladder and rectum have been identified, the next phase is to identify the location of the pubic bone. This is achieved through the identification of keypoints

on the image that satisfy specific location and intensity constraints. The use of corner points was selected instead of pixels because corner points can be extracted without any user input and it is computational efficient.

Corner points are identified using the Harris corner detector. It is based on the local auto-correlation function of a signal that measures the local changes of the signal with patches shifted by a small amount in different directions.

If I denotes a 2-D grayscale image, then, taking an image patch over the area (u, v) and shifting it by (x, y) . The weighted sum of squared differences between these two patches is given by:

$$S(x, y) = \sum_u \sum_v w(u, v) (I(u + x, v + y) - I(u, v))^2 \quad (4.2)$$

$I(u + x, v + y)$ can be approximated by a Taylor expansion and I_x and I_y are the partial derivatives of I , such that

$$I(u + x, v + y) \approx I(u, v) + I_x(u, v)x + I_y(u, v)y \quad (4.3)$$

This produces the approximation

$$S(x, y) \approx \sum_u \sum_v w(u, v) (I_x(u, v)x + I_y(u, v)y)^2 \quad (4.4)$$

which can be written:

$$S(x, y) \approx (x \ y) A \begin{pmatrix} x \\ y \end{pmatrix} \quad (4.5)$$

where A is the structure tensor,

$$A = \sum_u \sum_v w(u, v) \begin{bmatrix} I_x^2 & I_x I_y \\ I_x I_y & I_y^2 \end{bmatrix} = \begin{bmatrix} \langle I_x^2 \rangle & \langle I_x I_y \rangle \\ \langle I_x I_y \rangle & \langle I_y^2 \rangle \end{bmatrix} \quad (4.6)$$

The matrix indicates the Harris matrix, and angle brackets denote averaging (i.e., summation over (u, v)). A corner is characterized by a large variation of S in all directions of the

vector $(x \ y)$. By analyzing the eigenvalues, denoted λ , when both eigenvalues are small there is little change for any $(u \ v)$. Once one of the eigenvalues is large and the other is small it indicates there is an edge, since one direction has high change, while the orthogonal direction has small change. A corner is indicated when both eigenvalues are large. The result of the corner point detection process is shown in Figure 4.4.



Figure 4.4: Corner points extraction over an image with the Harris corner algorithm

Corner point extraction is followed by spatial filtering to eliminate the number of corner points that are outside of the vicinity of the bladder. The following equations provide the mathematical framework of the spatial filtering operation. Set C corresponds to the set of locations obtained after an initial selection of corner points.

$$C = \{p(x \ y) \in P: T_1 < I(x \ y) < T_2, d_1 < p(x) - c(x) < d_2, \quad (4.7)$$

$$c(y) < p(y) < d_3 \text{ and } \forall p \in P \}$$

where $p(x \ y)$ denotes the interest point location, P is the set of points obtained by the Harris corner detector, $I(x \ y)$ denotes the intensity level at $p(x \ y)$, T_1 is the threshold for minimum

pixel intensity, T_2 is the threshold for maximum pixel intensity, and d_1 and d_2 denote the minimum and maximum distances between the key points and the centroid of the bladder on the x direction, respectively. d_3 is the maximum distance between the key points and the centroid of the bladder on the y direction, where $c(x)$ and $c(y)$ denote the centroids of the regions on the x and y direction, respectively. These distances are determined based on the relative positions between anatomical structures on the body from the training image dataset. The constraints ensure that corner points that are below and to the left of the bladder and within a specific distance and intensity range are retained. For instance, the mean intensity value of pixels located on the pubic bone has been defined as 33 ± 10.4 using histogram analysis over the training image dataset. Hence, corner points with intensity levels between 10 and 60 can be considered as potential keypoints corresponding to the pubic bone as seen Figure 4.5.

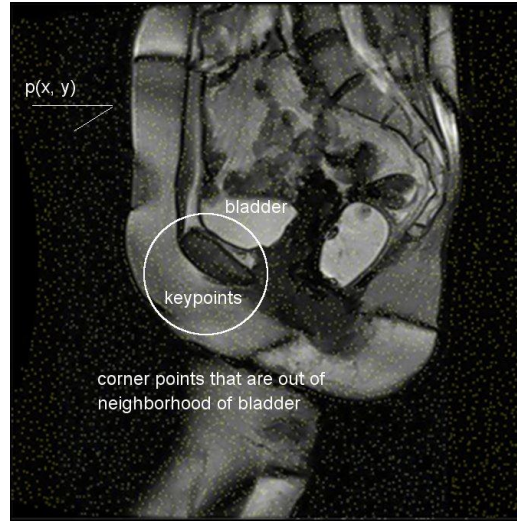
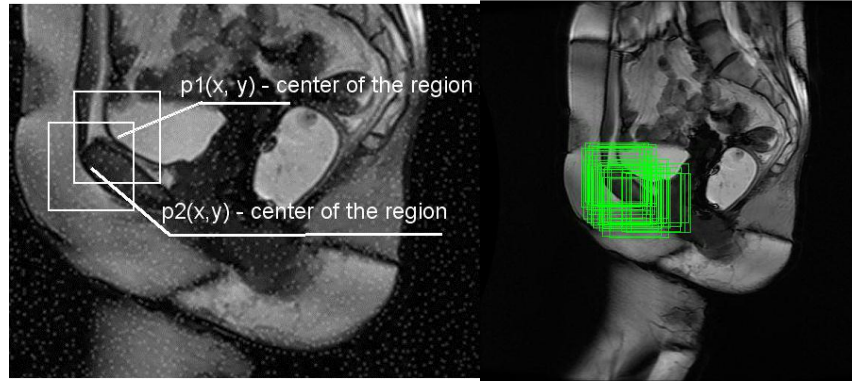


Figure 4.5: Keypoints within the local vicinity of the bladder

4.4.2. Generation of Candidate Bounding Boxes

After spatial filtering, potential pubic bone regions are generated as seen in Figure 4.6 and Figure 4.7. These bounding boxes are centered at the keypoints and the size is set to a value

defined by analyzing the training image dataset. Principal component analysis (PCA) is applied to the manually segmented pubic bone regions in the training image dataset to find the mean shape and the shape variation models of the pubic bone. This is used to determine the size of the bounding boxes to enclose the pubic bone. Each of these bounding boxes represents a potential bounding box for the pubic bone. However, some of these bounding boxes do not completely enclose the pubic bone as the keypoints may fall near the boundaries of the bone. For this reason, the bounding boxes that completely enclose the pubic bone need to be identified. To do this, each region based on 2D box and texture features is analyzed as described in the following sections.



(a)

(b)

Figure 4.6: Candidate region generation. (a) Keypoints used as centroids of candidate regions, (b) Candidate regions of pubic bone

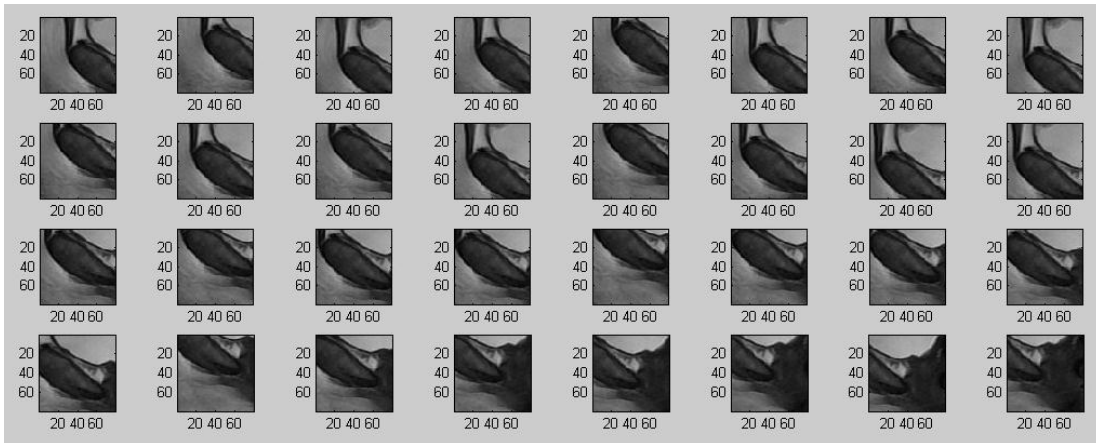


Figure 4.7: Generated candidate regions

4.4.3. Feature Extraction of Candidate Regions

The selected features need to be robust to represent changes and imaging conditions on each candidate region. The candidate regions are evaluated based on 2D box features and texture features. Texture features have shown to enable more reliable results on MRI by providing relative position information of any two pixels with respect to each other. Medical images possess different textures depending upon the area of the body considered for imaging. The texture features are (i) average gray level, (ii) average contrast, (iii) smoothness, (iv) skewness, (v) uniformity, and (vi) entropy.

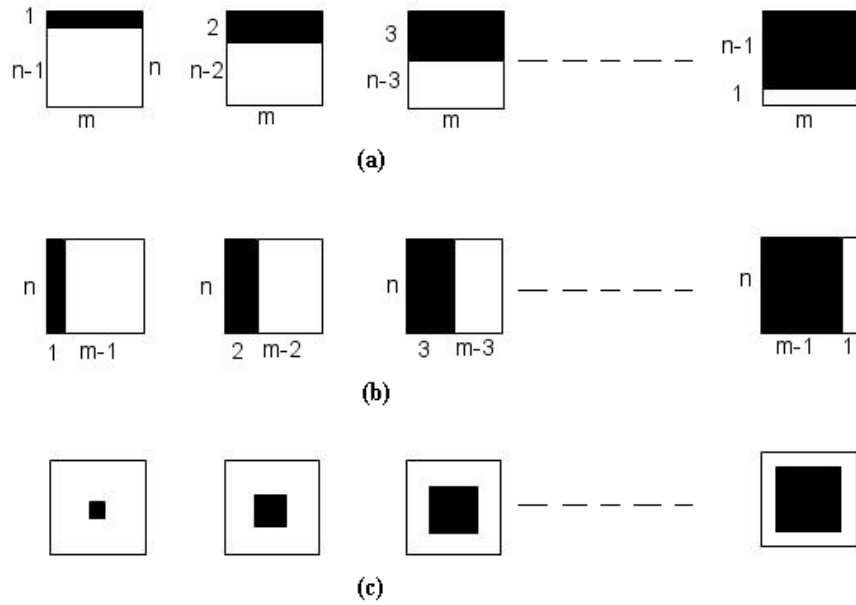


Figure 4.8: 2D box features. (a) Horizontal box features, (b) Vertical box features, (c) Centered box features

The other set of features used on evaluation of candidate regions are 2D box features. These features provide the average intensity difference between two displaced boxes as shown in Figure 4.8. For instance, the horizontal 2D box shown in Figure 4.8 (a) can be generated as follows:

$$\text{Horizontal box feature (1)} = \text{average of (1xm)} - \text{average of ((n - 1)xm)} \quad (4.8)$$

$$\text{Horizontal box feature (2)} = \text{average of (2xm)} - \text{average of ((n - 2)xm)} \quad (4.9)$$

$$\text{Horizontal box feature (k)} = \text{average of ((n - 1)xm)} - \text{average of (1xm)} \quad (4.10)$$

Since the centered pubic bone is desirable for bounding boxes bone location process, 2D box features provide information on whether the pubic bone is in the center of the bounding box or not. Similarly, texture features calculate six measures of texture from each generated region.

4.4.4. Classification of Bounding Boxes

For the candidate regions defined in Section 4.2.2., the feature set representing the candidate regions are evaluated using support vector machines. As described in Section 3.3, SVM has shown to achieve the highest classification accuracy for medical diagnosis compared to other classification techniques. This is a two-class problem where candidate bounding boxes are classified into bounding boxes of pubic bone or not. The classification of the candidate regions involves two steps: construction of the classifier and prediction. In the first step, a classifier structure is constructed based on the training data set using support vector machines (SVMs). The implementation of SVMs is designed to increase the speed of the classification process by classifying blocks of pixels instead of classifying each pixel. SVMs is trained using the “*kernel trick*” which allows the algorithm to fit the maximum-margin hyper plane in a transformed feature space to provide for non-linear decision surface as discussed in Section 4.3.2. After the regions are trained according to the features, the second step of the segmentation process is to apply the model to test example images using the built SVM classifier. The anticipated outcome at the end of this process is a set of two groups of regions that are automatically classified as enclosed pubic bone regions and partially enclosed pubic bone regions.

4.5. Identification of Coccyx and Sacral Promontory Regions

At this point of the process, the locations of the bladder, rectum, and pubic bone have been identified. Since the estimated position of the bladder, rectum, and pubic bone are strongly correlated with the coccyx and sacral promontory, the non-linear model is built to predict the location of the coccyx and sacral promontory regions. To do that, the location of the pelvic floor structures is parameterized using the bladder, rectum and pubic bone location information as seen in Figure 4.9. Therefore, the proposed model is first trained by non-linear regression model.

The locations of the bladder, rectum, and pubic bone are strongly correlated with the locations of the sacral promontory and coccyx. However, the relationship between these organs is complex given the different sizes and locations of the organs. Thus, non-linear regression model is built to predict the location of the coccyx and sacral promontory regions.

The proposed non-linear model has been trained through parameterizing the location of the pelvic floor structures with respect to the bladder, rectum and pubic bone locations. For training, the input is $(\mathbf{S}_i, \mathbf{P}_i)$, where \mathbf{S}_i is the input matrix and \mathbf{P}_i is the predicted matrix. \mathbf{S}_i consists of $c_{i1}^j(x, y)$, $d_{i1}(x, y)$, and $d_{i2}(x, y)$, where $c_{i1}^j(x, y)$ is the location of the centroid of structure j for the i^{th} subject, j corresponds to the regions (bladder, rectum, pubic bone, coccyx and sacral promontory), $d_{i1}(x, y)$ and $d_{i2}(x, y)$ are the relative distances between the centroids of the bladder and rectum to the centroid of the pubic bone, respectively. \mathbf{P}_i consists of $d_{i3}(x, y)$ and $d_{i4}(x, y)$, where $d_{i3}(x, y)$ and $d_{i4}(x, y)$ are the distances between the centroids of sacral promontory and coccyx to the centroid of the pubic bone, respectively. \mathbf{P}_i helps in predicting the sacral promontory and coccyx regions for the testing image dataset.

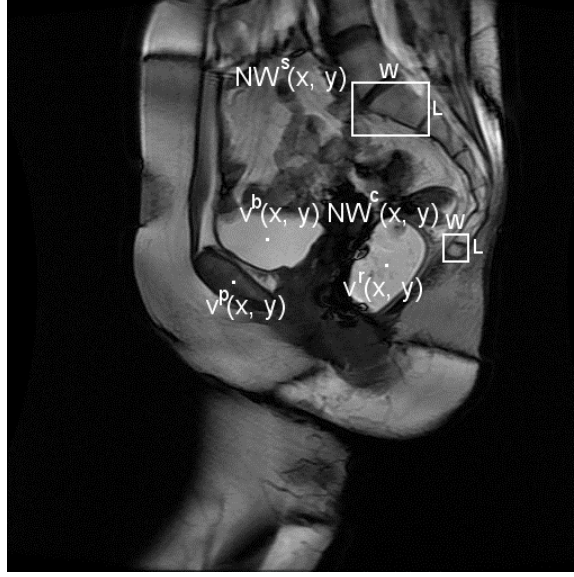


Figure 4.9: Parameterization of location of pelvic floor structure

After parameterization, the next step was to choose the model function to fit the model to the dataset. The selection of the model is a critical step as the accuracy of the model depends on this function. The data set has been trained using different non-linear models and the exponential polynomial model has been selected since it provides the minimum distance between the model curve and data points. Another reason for the selection of this model is that the residuals appear randomly distributed across the zero line indicating that the model is a good fit. The goodness of fit has also been measured using quantitative measures such as R square. The selected model provided the highest R square among the other models. The selected non-linear model can be expressed as follows:

$$f(V, \beta) = e^{\beta_0 + \beta_1 V_1 + \beta_2 d_1^2 + \beta_3 d_2^3} \quad (4.11)$$

Unlike in linear regression, most non-linear regression models require initialization of the parameters ($\beta_0, \beta_1, \beta_2$ and β_3). In order to find the initial values, the data set has been transformed and analyzed using linear regression. After selecting the initial values, the

parameters are estimated from the dataset by minimizing the distance between the model curve ($f(V, \beta)$) and the data points (y_i) using the equation below.

$$\sum_{n=1}^n [y_i - f(V, \beta)]^2 \quad (4.12)$$

Once the centroids of the sacral promontory and coccyx are determined, the bounding boxes that enclose these regions are determined based on PCA by generating the mean boxes and box variations of the coccyx and sacral promontory regions. PCA provides fixed size bounding boxes for each region. For instance, the maximum size for the bounding box of the sacral promontory has been defined as $[60px \ 6 \ px]$ based on the training dataset and PCA. For the coccyx, the maximum size for the bounding box was determined to be $[30px \ 30px]$. These bounding boxes are centered at the centroids of the sacral promontory and coccyx.

4.6. Results

The proposed automated bone localization model was evaluated on a wide range of MR images along the midsagittal view and at different stages of POP. The validation of the proposed model was performed on a representative clinical data set of 204 selected dynamic MRI. The database is divided into a training set and a testing set. The training set contains 114 images and the testing set is composed of the remaining 90 images for evaluating the model's performance. The proposed scheme was implemented using Matlab 2012b on a workstation with 3.00GHz dual processors and 2 GB RAM.

The regions identified through the proposed localization method were compared to the regions identified manually by experts. The Euclidean distance between the centers of the predicted and ground truth bounding boxes was used to assess the accuracy of the bone

localization approach. In addition, the region overlap between the predicted and ground truth regions is quantified using the Dice Similarity Index (DSI), where

$$DSI = 2 \cdot \frac{|A_{ref} \cap A|}{|A_{ref}| + |A|} \quad (4.13)$$

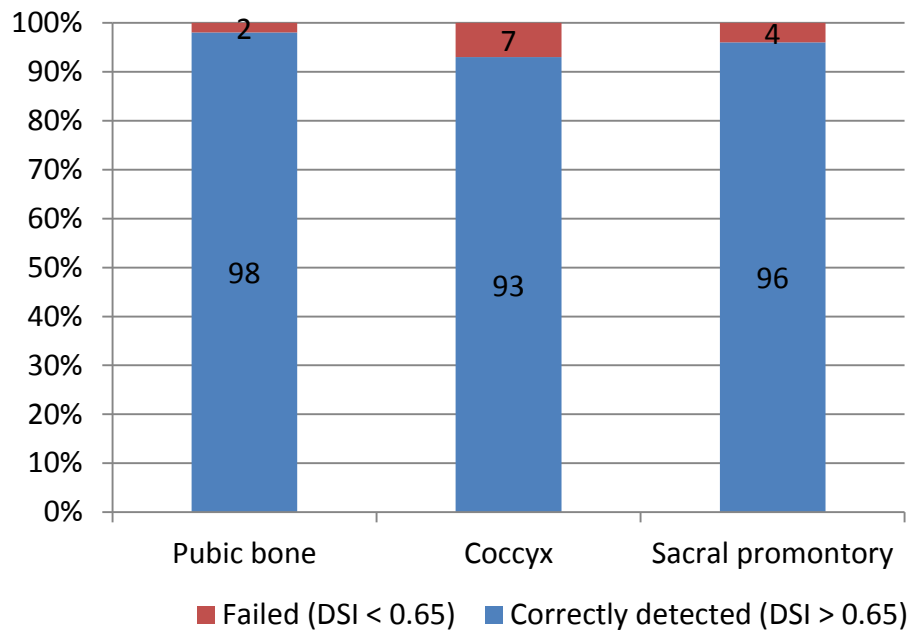
where A_{ref} and A indicate the manual and automatic segmented regions, respectively.

Table 4.1 provides the average center error in mm for the 90 testing images. The average center error for the pubic bone is 3.2 mm with 1.2 mm standard deviation. For the coccyx, the average center error is 14.5 mm with 4.6 mm standard deviation while the error and standard deviation for the sacral promontory are 8.1 mm and 3.8 mm, respectively. It can be observed that the center error for the pubic bone is the lowest compared to the coccyx and sacral promontory while average center error is the highest for the coccyx.

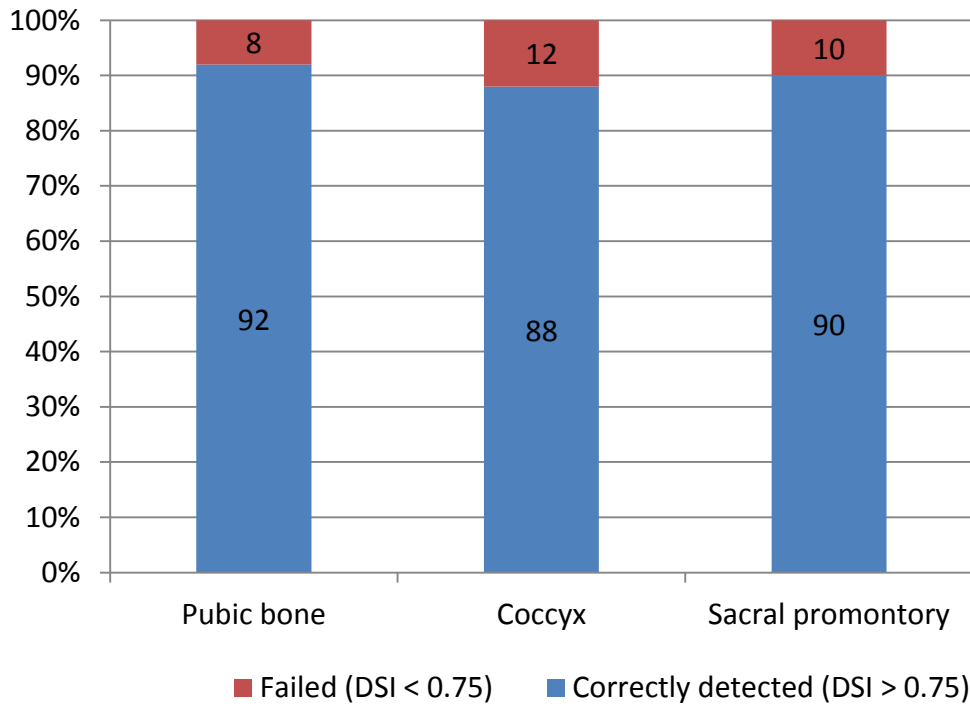
Table 4.1: Average center error (mean \pm standard deviation) for pelvic bone detection over 90 testing images

Center error (mm)		
Pubic bone	Coccyx	Sacral Promontory
3.2 \pm 1.2	14.5 \pm 4.6	8.1 \pm 3.8

Figure 4.10 provides the percentage of correctly detected cases at different thresholds for DSI. It can be observed that even at very high thresholds for DSI, the proposed method can correctly detect the pubic bone ($DSI > 0.90$) in 90% of the testing images by the proposed scheme. Similarly, the proposed scheme correctly detected the sacral promontory in 86% of the unknown images and the coccyx in 81% of the images. Once the overlapping percentage between two regions is decreased to 0.75, the proposed scheme correctly detected the pubic bone ($DSI > 0.75$) in 92% of the testing images. At the same time, the sacral promontory and coccyx were correctly detected in 90% and 88% of the testing images, respectively.

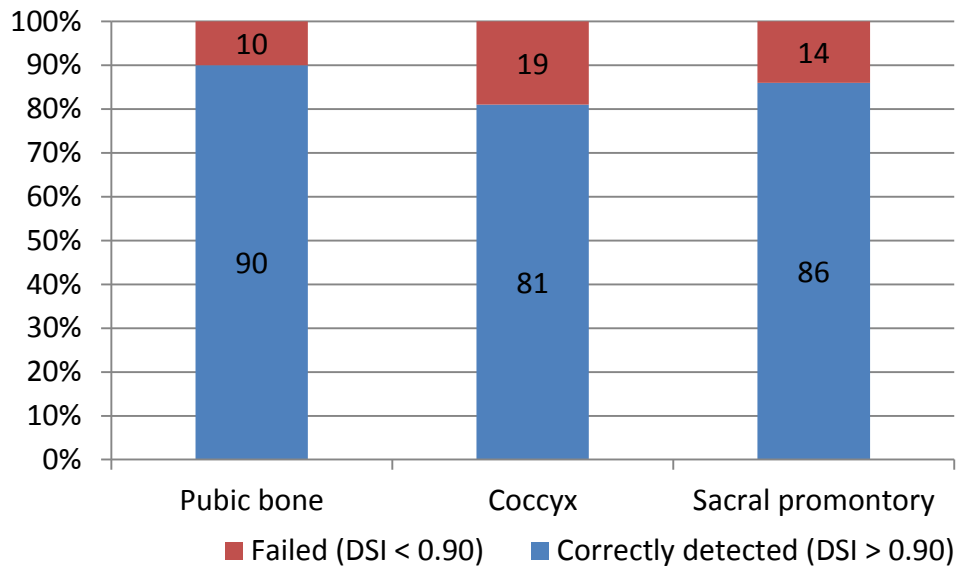


(a)



(b)

Figure 4.10: Percentage of correctly detected cases by the proposed bone localization model for different thresholds of DSI. (a) 0.65, (b) 0.75, (c) 0.90



(c)

Figure 4.10 (Continued)

Figure 4.11 shows some sample localization results of the proposed scheme compared to the ground truth regions of the pubic bone, sacral promontory, and coccyx. The regions shown with solid lines correspond to the regions found by the proposed scheme while regions with dashed lines indicate the ground truth regions.



Figure 4.11: Results of bone localization. (Solid line: predicted model, dashed line: ground truth)

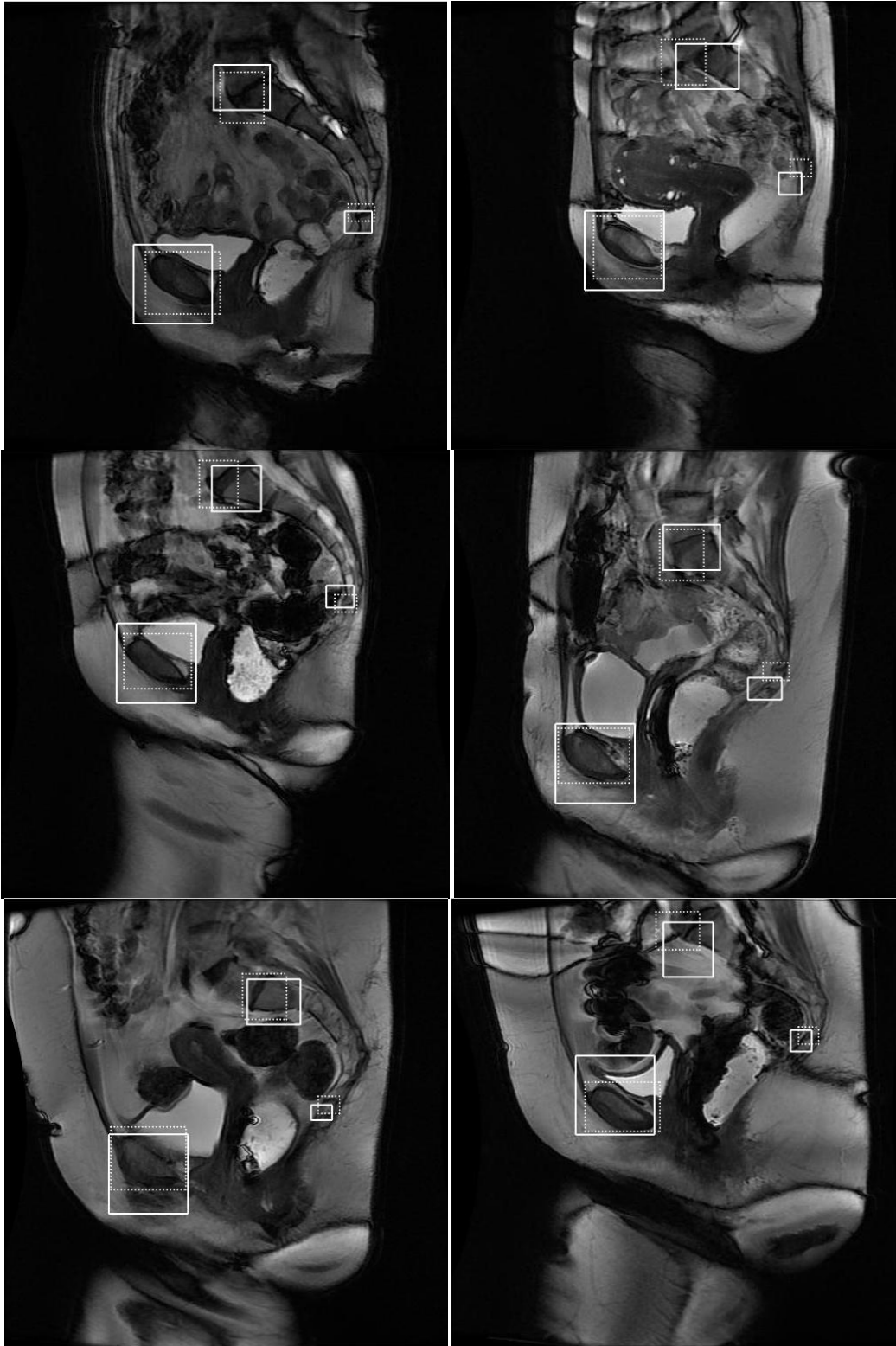


Figure 4.11 (Continued)

4.7. Conclusion

A model using SVM based classification and non-linear regression model with global and local information is presented to automatically localize multiple pelvic bone structures on MRI. The main contribution of this approach is a new parameterization through non-linear regression approach for the multiple bone localization problem. The model uses the location of pelvic organs to approximate the relative location of the pelvic bones. The best pubic bone region is selected using a SVM classifier based on texture and 2D box features. Then, a non-linear regression model was built to establish the association between the locations of the bladder, rectum, and pubic bone with respect to the location of the sacral promontory and coccyx. Results demonstrate that the proposed scheme can accurately find the location of the bone structures on each image consistently. The proposed automated bone localization scheme will be used to automatically identify regions of interest to extract image based predictors for pelvic floor measurements as described in the following chapter.

Chapter 5^{1 2}

Image-based Pelvic Floor Measurements Model

In this chapter, a new image based pelvic floor measurement model is presented. The model consists of two stages: bone segmentation and reference point identification. Experimental results show that the presented model can extract image based features faster, more accurately and consistently compared to the manual extraction process.

5.1. Overview of Proposed Segmentation Method

Pelvic floor measurements on MRI begin with the identification of reference points. As shown in Figure 5.1 (a), these reference points are located on three areas: pubic bone, sacral promontory, and coccyx. Each area has specific characteristics so different approaches are needed to find these points. Points located on the pubic bone (points 1, 2, and 3) can be found through segmentation of the pubic bone and its cartilage. On the other hand, points located on the sacral promontory and coccyx (points 4 and 5) can be defined as intersecting points, and can be

¹ The work presented in this chapter has been previously published (Onal S, Lai-Yuen, S., Bao, P., Weitzenfeld, A., Hart, S. MRI based Segmentation of Pubic Bone for Evaluation of Pelvic Organ Prolapse. IEEE Journal of Biomedical and Health Informatics. 2013;PP(99), p.2168-77). See Appendix C for copyright information.

² Some figures and tables of the work presented in this chapter have also been previously used in the following two articles. (1) Onal S, Lai-Yuen, S., Bao, P., Weitzenfeld, A., Greene, K., Kedar, R., Stuart, H. Assessment of a Semi-Automated Pelvic Floor Measurement Model for the Evaluation of Pelvic Organ Prolapse on MRI. International Urogynecology Journal 2014. doi: 10.1007/s00192-013-2287-4. (2) Onal S, Lai-Yuen, S., Bao, P., Weitzenfeld, A., Hart, S. Image based measurements for evaluation of pelvic organ prolapse. Journal of Biomedical Science and Engineering. 2013;6(1):45-55. See Appendix C for copyright information.

found using a corner detection algorithm. After all the reference points are determined, the points are connected through lines for pelvic floor measurements.

The proposed method consists of three main stages: pre-segmentation, segmentation, and point identification (see Figure 5.2). The first stage starts with noise reduction, contrast adjustment and normalization of the images followed by manual segmentation of the anatomical structures of interest for data training, and statistical mean shape generation. In the approach, each ROI is sub-divided into small blocks of 3×3 pixels to classify them as bone or background blocks and to reduce computational cost. In the second step, feature extraction of the blocks based on intensity and texture features is performed using independent significance feature selection method. Then, blocks are classified as bone and background blocks using support vector machines (SVM) followed K-means clustering to generate the initial segmentation. First phase morphological operation is used to eliminate small regions that do not belong to the bone regions. The final segmentation is obtained by incorporating prior shape information into the initial segmentation. Then, the reference points are identified for pelvic floor measurements. Following is the detailed description of the proposed method.

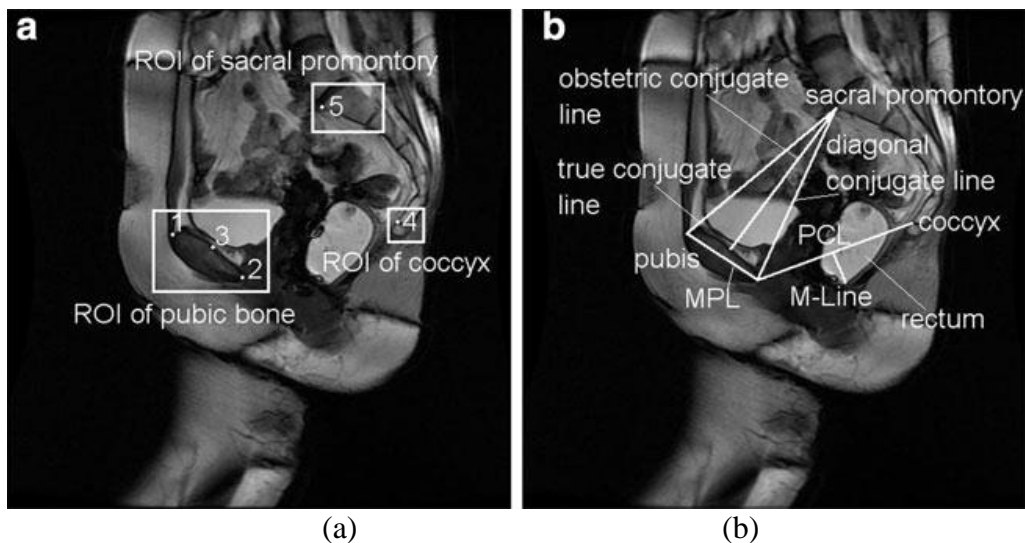


Figure 5.1: Point of interests and proposed MRI-based features. (a) Point of interest, (b) Current and proposed MRI-based features

5.2. Pre-segmentation Stage

The first step of the proposed method is to perform noise reduction by applying the convolution operation onto the raw image with the smoothing kernel. In this study, Gaussian kernel is used due to its computational efficiency and ability to control the degree of smoothing. The Gaussian kernel is expressed in the discrete form with a size of 3×3 pixels. After noise reduction, contrast adjustment is performed to improve the contrast in the images by stretching the range of intensity values.

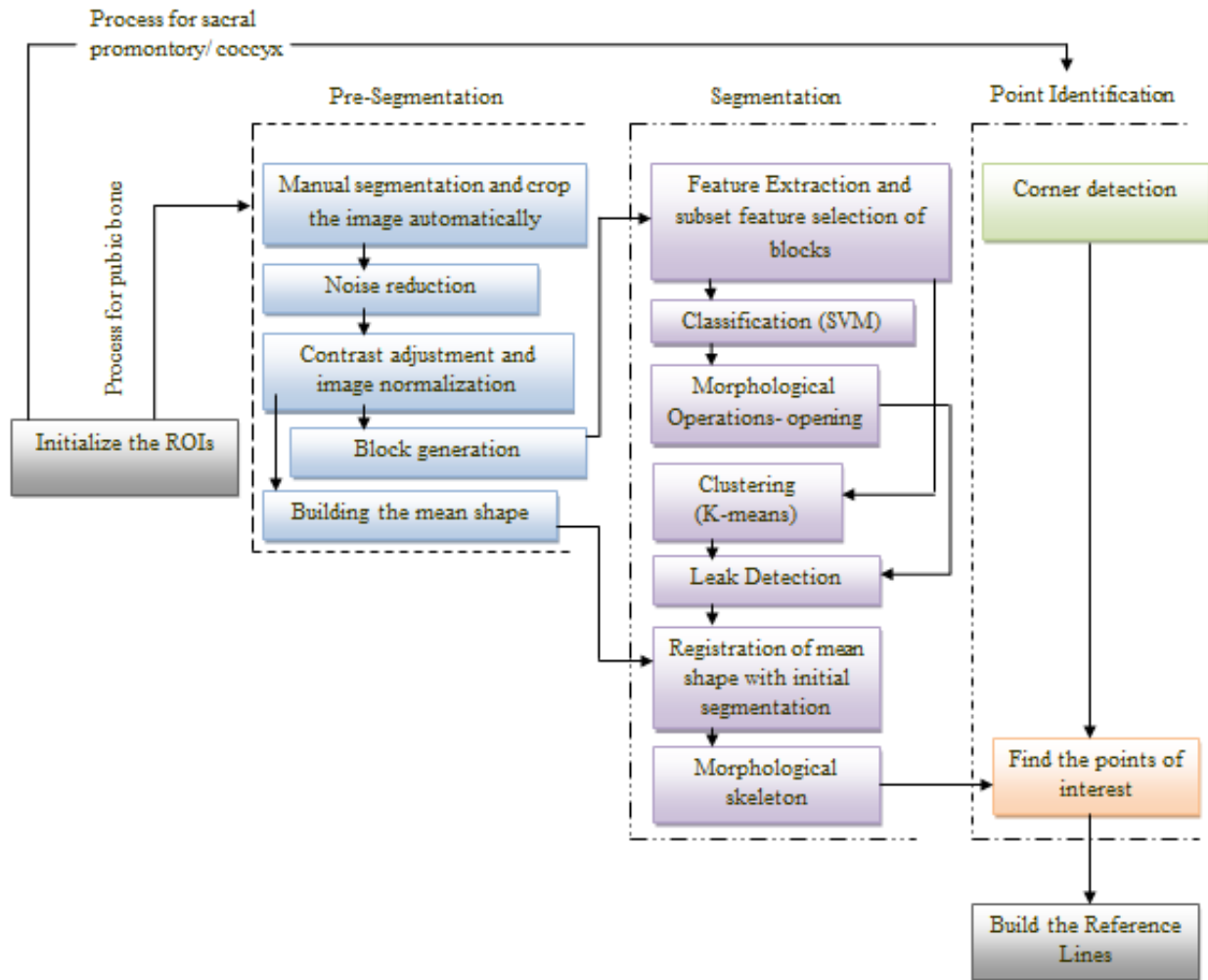


Figure 5.2: Overview of the proposed multi-stage method

Prior shape information is obtained by generating the mean shape of the pubic bone (bone, cartilage) from a set of training images. To achieve this, the pubic bone was segmented manually on all the images by a radiologist and the results were stored as a binary mask. The region of interest (ROI) for the pubic bone is cropped through a $K \times L$ size window using the automated bone localization algorithm mentioned in the previous chapter (Chapter 4) to build the statistical mean shape from the training set. The extracted structures are aligned with respect to a set of reference axes to filter out the differences in shapes due to translation, scaling, and rotation. An image is selected arbitrarily as the reference shape, and all the other shapes are aligned with respect to this reference shape. A mean shape is generated as a binary image as described in [112, 113].

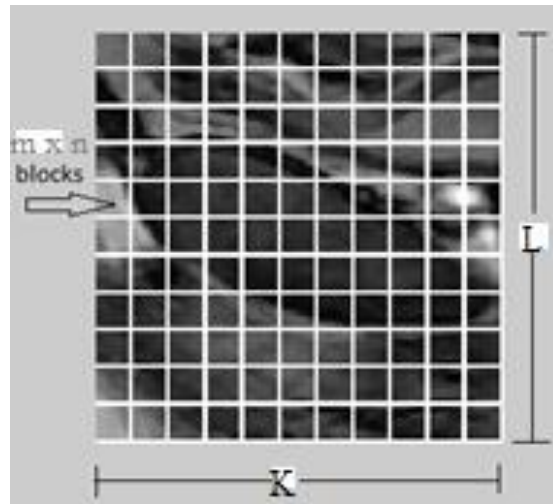


Figure 5.3: $K \times L$ size cropped image (window) and $m \times n$ size blocks. (Blocks are shown larger than 3×3 pixels for demonstration purposes)

Finally, the region of interest for the pubic bone is sub-divided into small blocks of $m \times n$ size as shown in Figure 5.3. These small blocks of pixels will be used for the classification process instead of using individual pixels to increase computational efficiency and to enable the use of texture features for classification.

5.3. Segmentation Stage

5.3.1. Feature Extraction

For classification, the main issue in the feature extraction task is to identify suitable features that characterize different patterns accurately. Since MRI has low-level contrast intensity, gray level based features are not sufficient to provide enough information for the classification. Texture features have shown to enable more reliable results on MRI by providing relative position information of any two pixels with respect to each other [114]. Medical images possess different textures depending upon the area of the body considered for imaging.

Gray level features are extracted from each block. Moreover, gray level co-occurrence matrix (GLCM) is used to extract the texture features suggested in Haralick [114]. GLCM provides information regarding the relative position of two pixels with respect to each other. GLCM are obtained using horizontal left to right direction. Table 5.1 shows the intensity and GLCM features used in this study.

Table 5.1: Intensity and GLCM features

Intensity Features	GLCM Features	
Average gray level	Autocorrelation	Sum of squares
Average contrast	Contrast	Sum average
Smoothness	Correlation	Sum variance
Skewness	Cluster prominence	Sum entropy
Uniformity	Cluster shade	Difference variance
Entropy	Dissimilarity energy	Difference entropy
	Entropy	Info. measure of correlation
	Homogeneity	Inverse difference normalized
	Maximum probability	

After feature extraction, a two-step feature subset selection is performed. In the first step, irrelevant or redundant features are removed using the independent significance feature selection method as described by Weiss and Indurkha [115]. This method is used to eliminate features with a significance level lower than 2 as calculated from the following equation:

$$\text{significance}_i = \frac{|\text{mean}(\text{Bone}_i) - \text{mean}(\text{Background}_i)|}{\sqrt{\frac{\text{var}(\text{Bone}_i) + \text{var}(\text{Background}_i)}{n_1 + n_2}}} \quad (5.1)$$

where Bone_i represents the i^{th} feature being measured from bone blocks, Background_i indicates the i^{th} feature being measured from background blocks, n_1 and n_2 are the corresponding number of blocks for bone and background, respectively. Based on the significance level, 12 independent significant features were identified in this study.

In the second step of the feature subset selection process, the final set of significant features for training the classifier is selected using the sequential forward selection method measured by 10-fold cross validation. In 10-fold cross-validation, the feature set was first divided into k subsets of equal size. Each subset is tested on the remaining $k - 1$ subsets using mean squared error that minimizes the mean criterion value. This process continues until the addition of more features does not decrease the criterion any further.

Proposed Two-Step Feature Subset Selection Algorithm:

Input: Full feature set $Y_f = \{x_i\}$

1. Start with the full feature set $Y_f = \{x_i\}$
2. Find the significance level of each feature $\{\text{significance}_i\}$
3. Select the best features $Y_b = \{\text{significance}_i > 2\}$
4. Set $Y_m = \{\emptyset\}$; Set $J(Y_m) = 0$
5. For each feature x_j in Y_b
 - Calculate $J(Y_m + x_j)$
 - if $J(Y_m + x_j) > J(Y_m)$
 - update $Y_m = Y_m + x_j$; $J(Y_m) = J(Y_m + x_j)$;
 - end
6. End

Output: selected subset feature $Y_m = \{m_k\}$ where $m \in x$

5.3.2. Block Classification

The classification of the image blocks involves two steps: construction of the classifier and prediction. In the first step, a classifier structure is constructed based on the training data set using support vector machines (SVMs). The implementation of SVMs is designed to increase the

speed of the classification process by classifying blocks of pixels instead of classifying each pixel. The SVMs was trained using the “*kernel trick*” which allows the algorithm to fit the maximum-margin hyper plane in a transformed feature space to provide for non-linear decision surface. The training vectors $\mathbf{x}_i, i = 1, 2, \dots, L$ are nonlinearly mapped onto a high-dimensional feature space by $\Phi: \mathbb{R}^M \mapsto \mathcal{F}$ and then a linear separation is attempted in \mathcal{F} . If \mathcal{F} is a Hilbert space, K is a kernel function in the original space \mathbb{R}^M that describes the inner product in \mathcal{F} .

$$\Phi(u) \cdot \Phi(v) = K(u, v) = (u \cdot v + 1)^2 \quad (5.2)$$

where $K(\mathbf{u}, \mathbf{v})$ should satisfy Mercer’s condition that ensures that the kernel function can always be expressed as the dot product between two input vectors in high dimensional space. This transformed space of the SVM kernels is called a reproducing kernel Hilbert space. The Radial Basis Function kernel (RBF) was employed in the training process to construct nonlinear SVMs and is described as follows:

$$K(u, v) = \exp(-\gamma ||u - v||^2) \quad (5.3)$$

There are two parameters for an RBF kernel that need to be determined: C representing the penalty parameter and γ representing the RBF sigma parameter. Cross validation is used to identify the best (C, γ) , 10-fold cross validation in this study, so that the classifier can accurately predict unknown data. After the blocks are trained according to the selected features, the second step of the segmentation process is to apply the model to test example images using the built SVM classifier. The anticipated outcome, R_{class} , at the end of this process is a set of two groups of blocks that are automatically classified as bone (white) and background (black) as shown in Figure 5.4 (b).

The classification method evaluates each block independently based on the selected features. Since the classifier may produce errors, a relaxation stage is needed to smooth the

classifier's output. Therefore, first phase morphological operations are applied to the classifier's output to remove the misclassified background blocks. The filling operation is used to fill the small holes and gaps on the contours first and then small regions that are fewer than 100 pixels are removed by using the area opening operation. Image opening is done by using “disk” structuring elements of size 4 followed by “*thinning*”. The result, $R_{class+morph}$, is shown in Figure 5.4 (c).

The bone segmentation may occasionally include regions with similar intensity characteristics such as soft tissue. These segmentation problems are called as “*leaks*”. Such occasional leak problems can take place when pubic bone and background regions (soft tissue, cartilage and fat regions) become joined together due to the lack of strong edges between them. This situation requires operations to separate the two regions as described in the following sections.

5.3.3. Block Clustering

A leak detection approach based on integrating SVM classification and K-means clustering is proposed. K-means clustering is used since it is convenient for medical images as the number of clusters (K) is usually known for particular regions of human anatomy [111]. The region of the pubic bone can be divided into four sub-regions representing the bone, cartilage, fat, and background. Therefore, K is selected to be 4 in this study. Since the basic K-means clustering is susceptible to initialization, a “bisecting K-means” algorithm presented in [116] was used. The idea in the bisecting K-means is to obtain K clusters by first splitting the set of all points into two clusters. Then, one of these clusters is selected for splitting and the process continues until K clusters are generated. The bisecting K-means algorithm is less dependent on

initialization because it performs several trial bisections and takes the one with the lowest sum of the squared error (SSE). Outcome of this process is the region called $R_{cluster}$.

5.3.4. Leak Detection and Registration

After clustering the blocks, the cluster that represents the cartilage is selected to identify the leak as shown in Figure 5.4 (d). The clustered cartilage region $R_{cluster}$ is subtracted from the classified region after first morphological operation $R_{class+morph}$ to find the leakage area $R_{leakage}$ as seen in Figure 5.4 (e) (black region). Their complement $R_{complement}$ is shown in Figure 5.4 (f) (white region), which is calculated as follows:

$$R_{complement} = (R_{class+morph} - R_{cluster})(i, j) \geq 1 \quad (5.4)$$

where,

$$R_{leakage} = (R_{class+morph} - R_{cluster})(i, j) < 0 \quad (5.5)$$

As shown in Figure 5.4 (f), the region $R_{complement}$ provides separated regions that include the desired bone region (largest region in the figure), and the soft tissue and fat regions. $R_{complement}$ is improved by incorporating prior shape information, $R_{meanshape}$, as shown in Figure 5.4 (g). $R_{meanshape}$ is registered with the $R_{complement}$ by using registration with the similarity type transformation that contains rotation, translation and scaling as shown in Figure 5.4 (h). The initialization problem was eliminated by using the largest component in $R_{complement}$ that corresponds to the bone structure. Any small regions surrounding the bone structure were removed by morphological opening operations in the previous steps. The mean square error metric was used as a similarity metric and step gradient descent approach was used for minimization. This results in the initial segmentation region $R_{initial}$.

$$R_{initial} = \left(R_{meanshape} \xleftrightarrow{\text{Transform}} R_{complement} \right) \quad (5.6)$$

Then, as shown in Figure 5.4 (i), the correction step involves adding the cartilage region $R_{cluster}$ to $R_{initial}$ to obtain the preliminary region of the pubic bone $R_{initial+cluster}$. The current procedure for identifying the pelvic floor reference points on MRI is based on the pubic bone and its cartilage (bone+cartilage). For this reason, the goal is to identify both the pubic bone and its cartilage to determine the corresponding reference points automatically. In the work, k-mean clustering is employed to find the cartilage region and the texture-based classification provides the bone structure region. Therefore, the two regions are combined to obtain the full bone+cartilage region to find the reference points for assessing POP. Finally, a second registration is performed between the corrected image, $R_{initial+cluster}$ and the mean shape, $R_{meanshape}$, with the same similarity type transformation. At the end of this process, the final segmentation of the pubic bone is obtained, R_{final} , as shown in Figure 5.4 (j). Then, the boundary of the pubic bone is extracted as shown Figure 5.4 (k). This will be used to identify the reference points using the morphological skeleton operation as indicated in Figure 5.4 (l).

$$R_{final} = \left(R_{meanshape} \xleftrightarrow{\text{Transform}} R_{initial+cluster} \right) \quad (5.7)$$

5.4. Point Identification Stage

Once segmentation is performed, the reference points located in the pubic bone can be found using the morphological skeleton operation. This operation removes pixels on the boundaries of the pubic bone and provides at least three branches of the skeleton but does not allow the object to break apart. The remaining pixels constitute the image skeleton, whose extreme points indicate the reference points 1, 2 and 3.

On the other hand, points in the region of sacral promontory and coccyx are defined as corner points for which there are two dominant and different edge directions on the local neighborhood of the point. For this reason, these points are detected using corner detection algorithms. In the previous work [113], the Harris corner detection algorithm was adapted to detect the bony joints as shown in Figure 5.5. The Harris corner detector [117] is based on the local auto-correlation function of a signal that measures the local changes of the signal with patches shifted by a small amount in different directions.

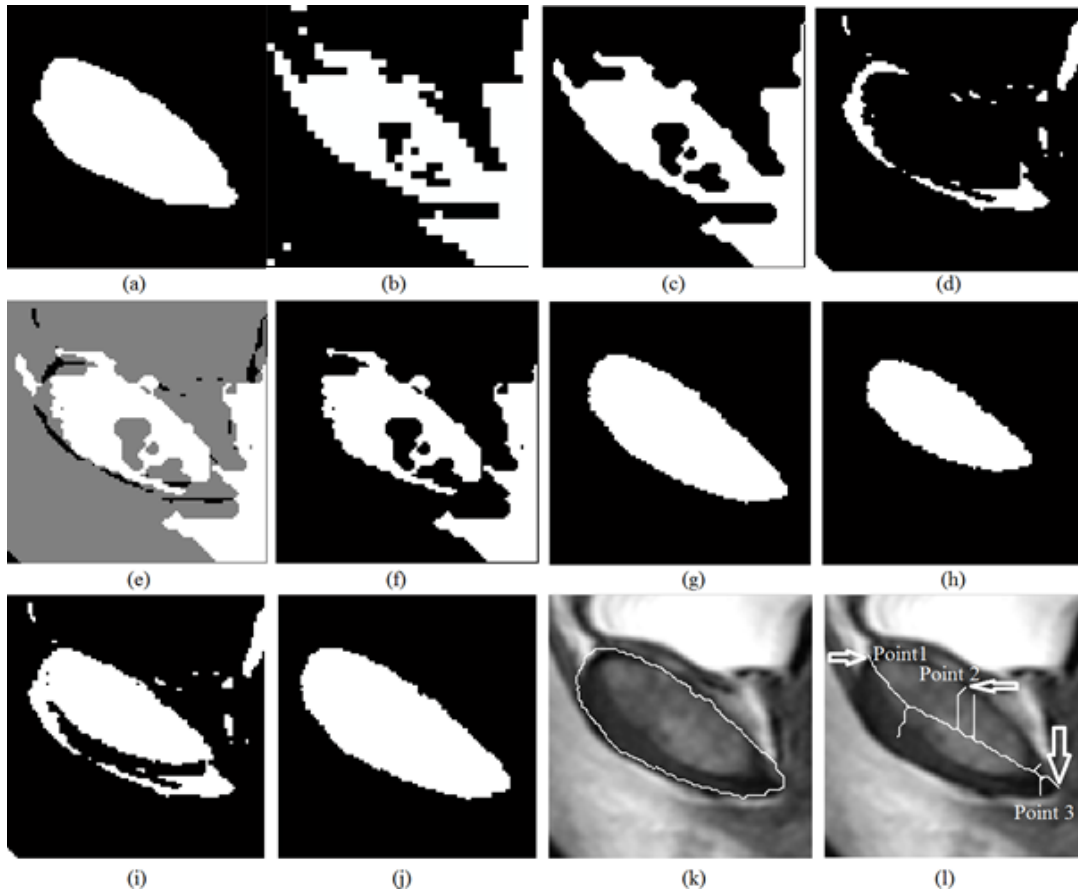


Figure 5.4: Proposed segmentation process. (a) Ground truth image, (b) Block classification (R_{class}) with bone (white) and background (black), (c) First phase classified image with morphological operations ($R_{class+morph}$), (d) Clustering ($R_{cluster}$) with cartilage (white) and background (black), (e) Leakage region detected (black area), (f) $R_{complement}$, (g) Mean shape ($R_{meanshape}$), (h) First registration between f and g ($R_{initial}$), (i) Union of d and h ($R_{initial+cluster}$), (j) Final registration between g and i (R_{final}), (k) Final segmentation of pubic bone, (l) Morphological skeleton of final segmentation

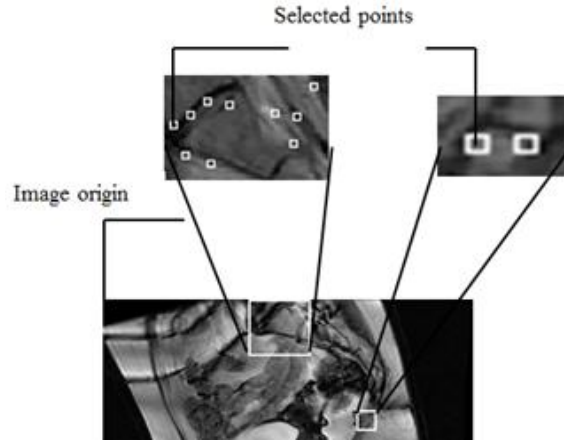


Figure 5.5: Reference bony joints for sacral promontory and coccyx



Figure 5.6: Pelvic floor reference points and lines generated by the proposed method

Once the reference points are identified, they are moved onto the original MR image as seen in Figure 5.6. These points are then connected using lines that represent the reference lines normally used to characterize the presence and severity of pelvic organ prolapse: PCL and MPL. The identified points are also used to determine other reference lines such as Diagonal, Obstetric and True Conjugate lines, which could possibly be used for the diagnosis of different types of POP.

5.5. Results

The validation of the proposed method was performed on a representative clinical data set of 25 selected dynamic MRI for this study. The database was divided into a training set of 10 randomly selected images and a testing set composed of the remaining 15 images. The dynamic MRI of each patient consists of 20 image sequences. The presented method was implemented using *Matlab* 2012b on a workstation with 3.00GHz dual processors and 2 GB RAM.

5.5.1. Segmentation Accuracy

The performance of the proposed segmentation method was measured by quantifying the region overlap between the manual and automated segmentations using the *Dice Similarity Index* (*DSI*), where

$$DSI = 2 \cdot \frac{|A_{ref} \cap A|}{|A_{ref}| + |A|} \quad (5.8)$$

A_{ref} and **A** indicate the manual and automatic segmented region, respectively.

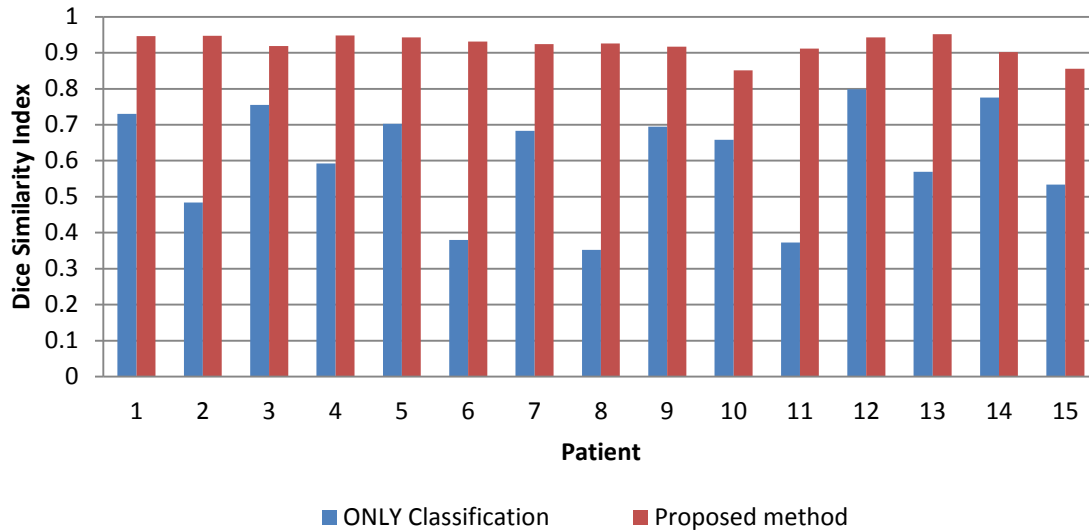
In addition to the dice similarity index, two additional measures were used: correct rate and area error measure (AEM). Correct rate is measured by quantifying correctly assigned pixels as bone over assigned pixels. Area error measure is defined as the percentage of area error for the evaluated segmentation area:

$$Area\ error\ measure(AEM) = \frac{|A_{ref} - A|}{|A_{ref}|} \quad (5.9)$$

The Hausdorff distance [118] is calculated between the contours of the manually segmented pubic bone and the segmentation from the proposed algorithm. The mean absolute distance (MAD) is also determined based on the average distance between the automatic segmentation and the ground truth.

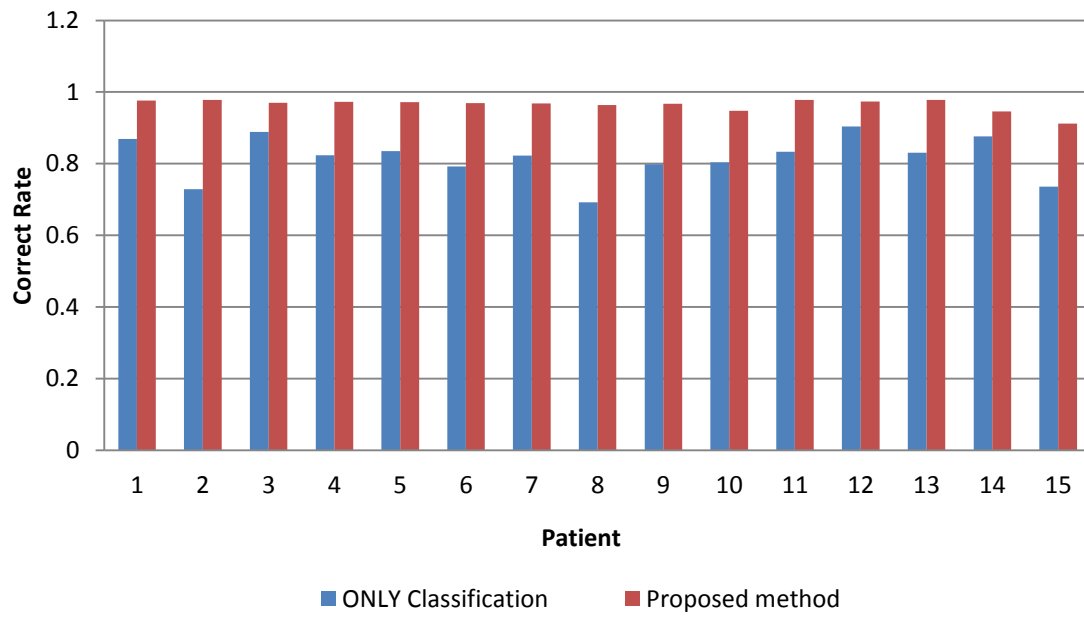
5.5.2. Bone Segmentation

First, the segmentation results from the proposed method vs. results from the texture-based classification method were compared only as shown in Figure 5.7. Each method is tested against the manually segmented region identified by experts. The texture-based classification method is approximately 6 seconds faster than the proposed method. However, the segmentation accuracy of the texture-based classification is very low with a DSI and correct rate of 52% and 79%, respectively. It was also observed that the segmented regions obtained with the classification method only resulted in over-segmentation in most of the cases. The area error measure should be 0 for a perfect segmentation. The classification method resulted in more negative values indicating that the segmented regions are larger than the manually segmented regions. On the other hand, the proposed method with the leak detection algorithm provides higher accuracy for all cases with a dice similarity metric above 92% for thirteen cases and a correct rate metric above 95% for all cases.

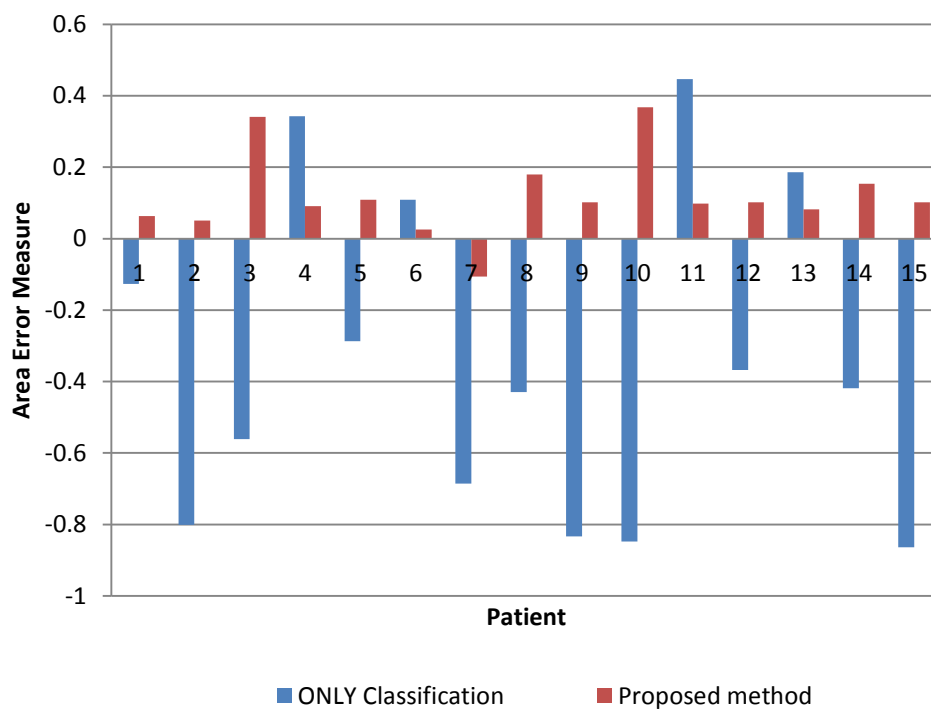


(a)

Figure 5.7: Performance comparison of the proposed method and texture-based block classification only for the average over the 20 image sequences per patient. (a) Dice similarity index, (b) Correct rate, (c) Area error measure, (d) Computation time

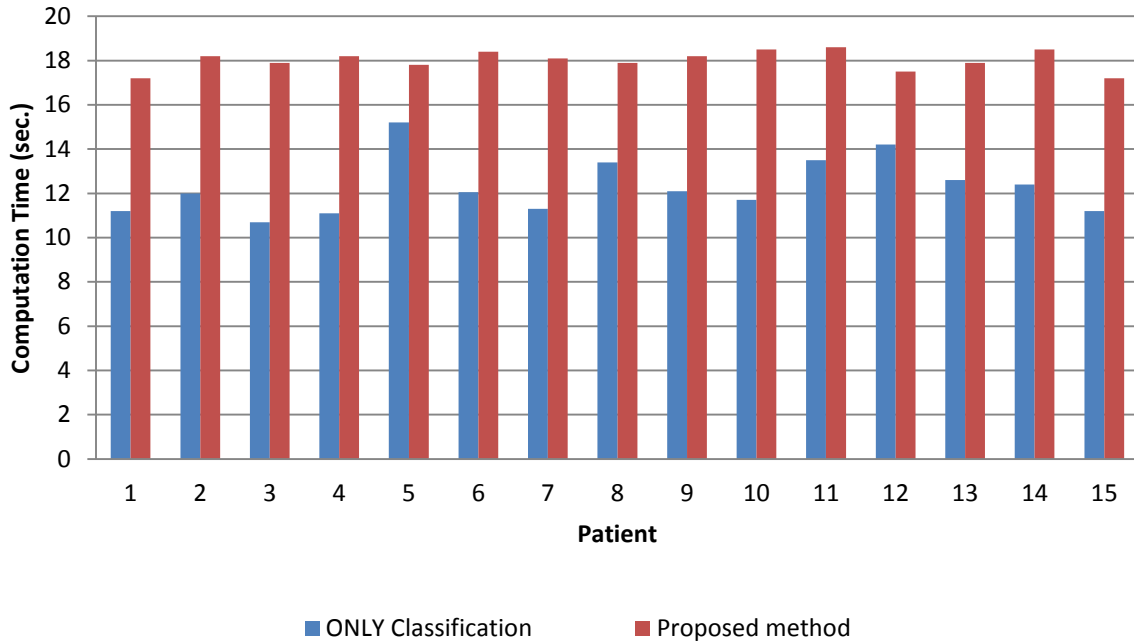


(b)



(c)

Figure 5.7 (Continued)



(d)

Figure 5.7 (Continued)

Table 5.2: Significance of each variable in the performance of the segmentation processes

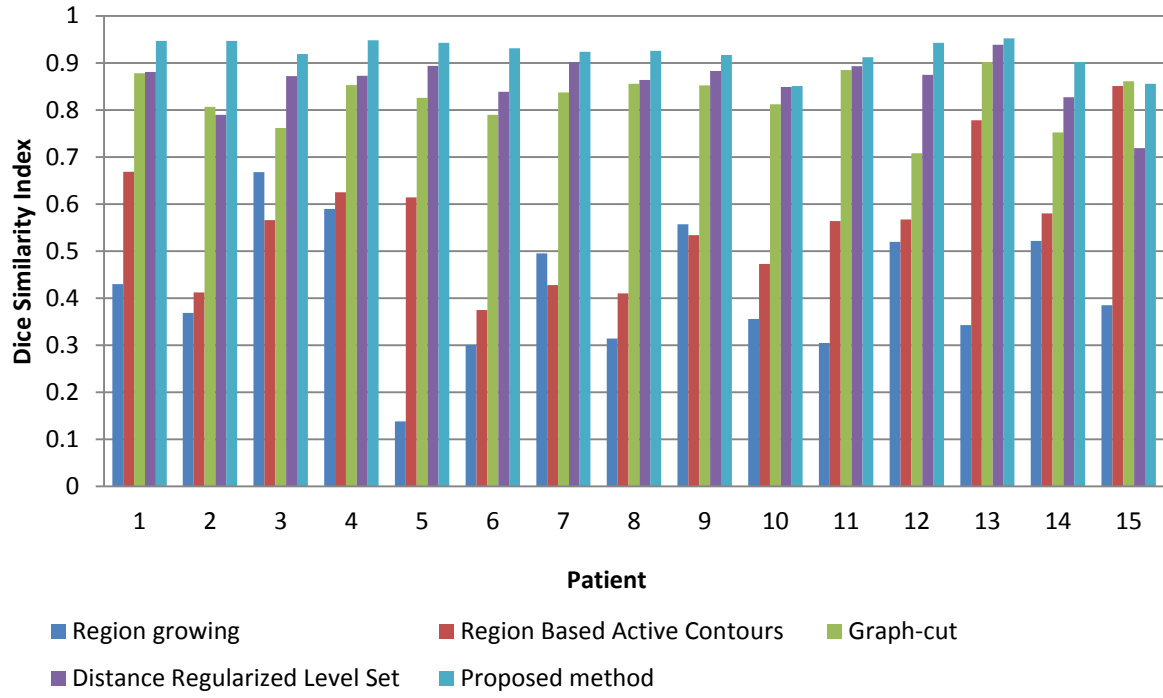
Region growing	Absolute threshold level to be included: 10 and maximum distance to the initial position: 20
Region based active contour	Alpha: 0.2 Maximum iteration: 250
Graph-cut:	10 seed for background and 10 seeds for foreground Large constant, $K=10$ Similarity variance, $\sigma=1$ Terminal Constant, $\lambda=10^{12}$ Similarity Constant, $c=10^8$
Distance regularized level set	Time step=1 Coefficient of the distance regularization, $\mu=0.2/\text{time step}$ Inner iteration =10 Outer iteration =30 Coefficient of the weighted length, $\lambda=5$ Coefficient of the weighted area, $\alpha=-3$ Parameter that specifies the width $\epsilon=1.5$

In order to verify the quality of the proposed segmentation technique, the method was compared with four commonly used segmentation methods in medical image segmentation:

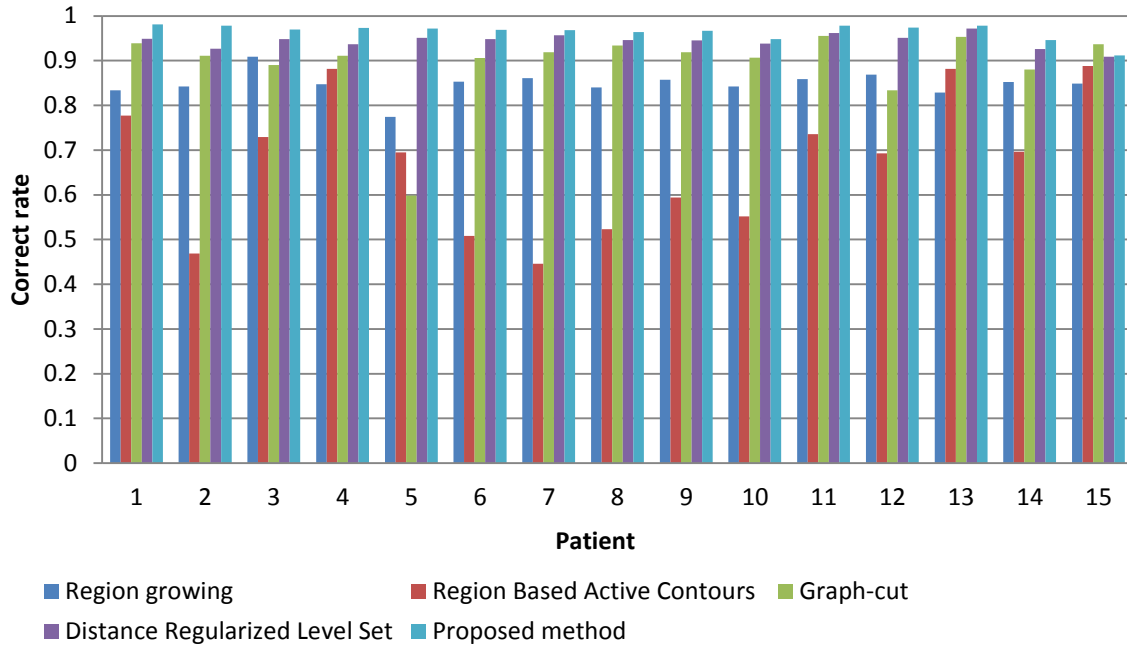
region growing [119], region based active contour [120], graph-cut [121], and distance regularized level set [122]. In this study, the Taguchi method [123] is used to analyze the significance of each variable in the performance of the segmentation processes. The parameters used are given in Table 5.2.

As shown in Figure 5.8 (d), the region growing method is the fastest segmentation method; however, its segmentation accuracy is the lowest among the methods, with approximately 30% in DSI and 80% in correct rate. It can also be observed that the segmented regions from the region growing method are smaller than the manually segmented regions for all cases. The graph-cut and distance regularized level set methods provide better results than the region growing and region based active contour for all cases in terms of DSI and correct rate. However, both methods have drawbacks such as longer computational time, initialization sensitivity, and the need to select the best parameters. The area error measure rates for these methods are also very low compared to the region growing and active contour methods.

The proposed method provides the highest accuracy with above 92% in DSI for thirteen cases and above 95% in correct rate metric for all cases. In terms of computational time, the method is the second fastest method. Results also show that the proposed method only has one case with over-segmentation but with very low error rate. Only two cases provided a smaller region when compared with the manually segmented region. These results demonstrate that the proposed segmentation technique achieves higher segmentation accuracy and performance compared to other segmentation methods.

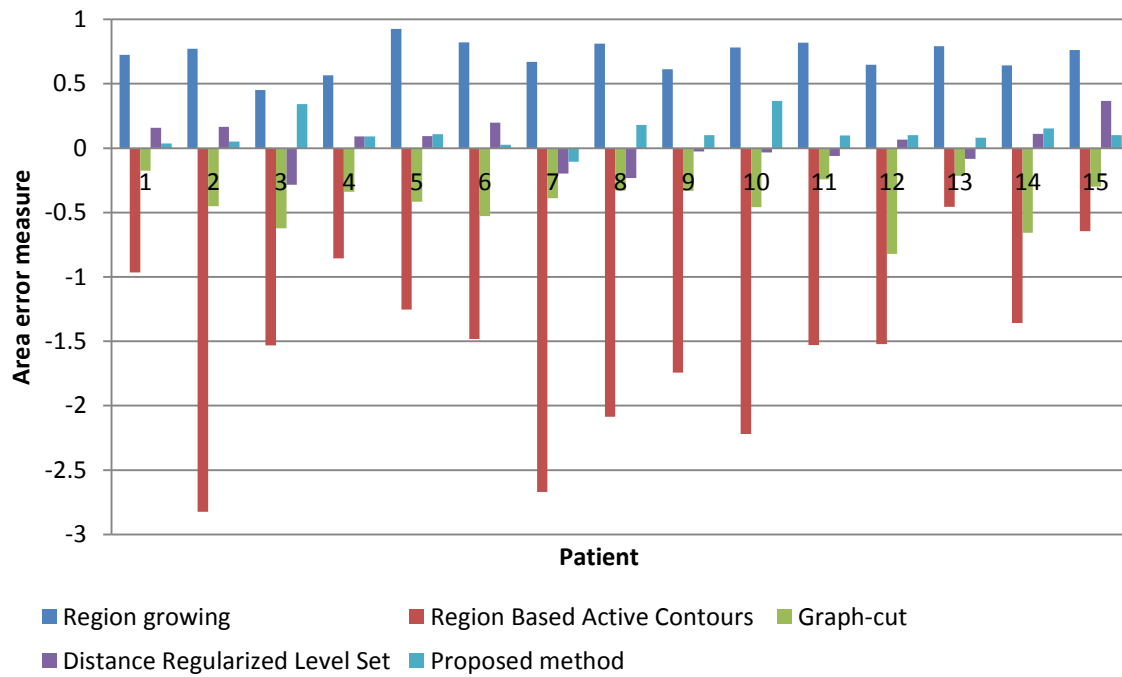


(a)

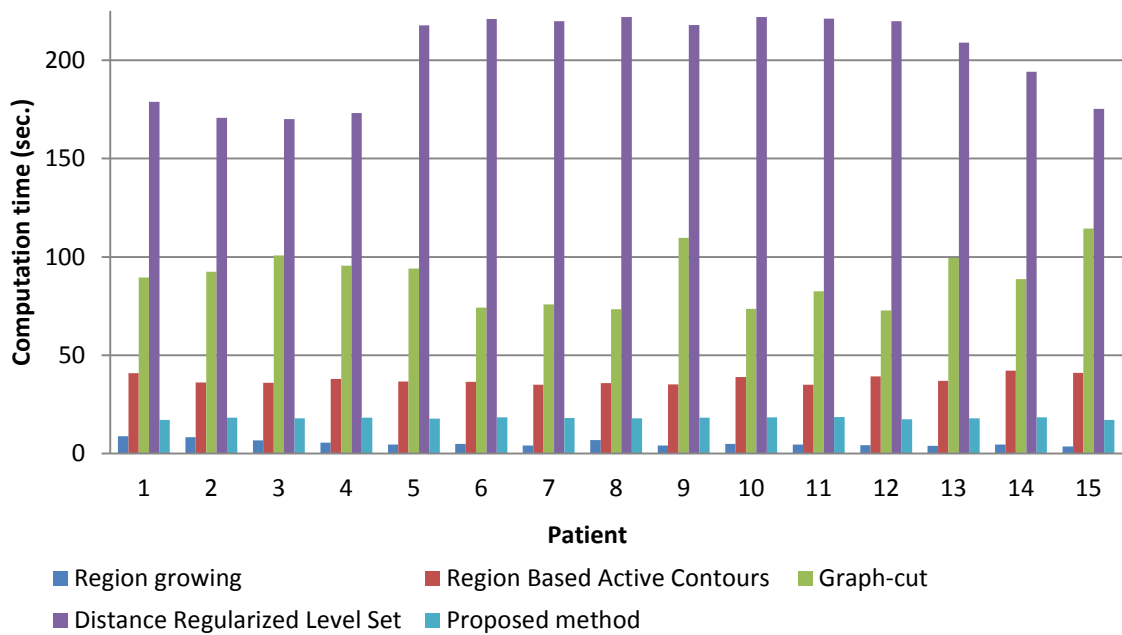


(b)

Figure 5.8: Performance comparison of the proposed method with other commonly used segmentation methods. (a) Dice similarity index, (b) Correct rate, (c) Area error measure, (d) Computation time



(c)



(d)

Figure 5.8 (Continued)

5.5.3. Reference Points Accuracy

The proposed segmentation mechanism was applied to identify the reference points on the pelvic bone and vertebra on the testing images. The accuracy of the point identification is measured by comparing them with the average location of the manually identified points. Then, the point accuracy is measured by $Point\ accuracy_j = n_j / T$ where n_j is the number of cases where the points are within the distance range j , and T is the total number of cases in the testing set. The Hausdorff distance was also calculated between the reference points identified by the proposed method and the reference points identified manually by experts.

5.5.4. Identification of the Reference Points

The proposed method was used to identify the pelvic bone and its reference points (p1, p2, and p3) and the reference points on the vertebra (p4 and p5) on the testing images. The point locations identified by the proposed method was compared with the points identified manually by three experts over three iterations. The average of the three iterations is calculated to find the experts' average point location. Table 5.3 shows the standard deviation of each point identified by the experts. The computation time of the manual point identification process for each patient that has 20 image sequences was about 10 minutes. As shown in the table, each point has a standard deviation range for all the fifteen images. Inter-observer reliability was also assessed by calculating the intra-class correlation coefficient (ICC) for all five reference points. An ICC >0.9 indicates excellent agreement, between 0.9 and 0.6 good agreement, between 0.6 and 0.4 moderate agreement, and <0.4 poor agreement. The computation time of the proposed point identification method was about 4.5 minutes

Table 5.3: Min and max standard deviation of reference points identified over all trials on 15 patients performed by 3 experts

<i>Point</i>	<i>Standard deviation (in mm) by manual identification</i>		<i>ICC</i>	<i>CI 95%</i>
	<i>x</i>	<i>y</i>		
p1	[0.31 – 4.52]	[0.22 – 4.37]	0.95	(0.94-0.96)
p2	[0.13 – 3.08]	[0.37 – 3.64]	0.98	(0.97-0.99)
p3	[0.63 – 6.47]	[0.83 – 4.12]	0.98	(0.96-0.98)
p4	[2.01 – 21.04]	[4.37 – 26.87]	0.81	(0.79-0.94)
p5	[0.38 – 27.19]	[1.01 – 20.12]	0.97	(0.94-0.98)

Table 5.4: Hausdorff distance and mean distance between point location identified by the proposed method and manual ground truth point location

<i>Point</i>	<i>Hausdorff distance</i>	<i>Mean distance</i>
p1	4.12	1.10
p2	10.19	2.13
p3	6.08	1.93
p4	14.42	4.00
p5	8.54	2.40

Table 5.5: Euclidian distance between points identified manually and using proposed model for 15 patients

	P1	P2	P3	P4	P5	P6	P7	P8	P9	P10	P11	P12	P13	P14	P15
p1	1.5	1.3	3.3	3.2	3.9	6.9	6.8	2.1	5.4	3.7	0.9	6.9	3.5	5.2	0.9
p2	7.0	16.3	3.8	3.0	1.9	3.2	3.4	5.6	4.7	14.9	8.2	4.1	1.4	1.2	0.9
p3	5.6	3.9	3.0	2.3	11.2	9.6	5.3	9.9	7.5	3.0	2.4	3.0	3.9	2.6	2.7
p4	14.8	24.3	7.6	5.3	5.3	9.8	12.3	2.9	5.7	6.4	9.4	17.4	8.8	1.1	3.8
p5	8.7	10.7	9.6	6.5	4.1	7.3	1.1	3.3	3.6	5.8	2.8	4.2	5.7	1.8	7.0

Table 5.4 provides the Hausdorff distance and the mean distance between the point locations identified by the proposed method and experts. This can be confirmed from Table 5.2 where points 4 and 5 have the highest standard deviation indicating that these two points are located with the highest variability among experts. Although the manual point identification procedure has high standard deviation indicating that each expert identified points in different locations, the accuracy of the automatically identified points by the proposed method was compared to the average location of the manually identified points. To do that, the Euclidian

distance is calculated between the manually and automatically identified points as shown in Table 5.5.

Then, the accuracy of the automated points is established based on the distance range as shown in Table 5.6. For instance, in the table, the accuracy of point 1 is shown as 67% for [0-5] mm distance range. This means that in ten cases from a total of fifteen cases, the distance between the automatically identified point and the manually identified point is between 0 and 5 mm. The table shows that the cumulative accuracy increases as the distance range increases. As seen in the table, the lowest accuracy obtained is related to points 4 and 5. Based on the results shown in Table 5.4, the proposed method is able to accurately identify all the reference points within the [0-20] mm distance range. This range is considered by experts as a practically acceptable accuracy level.

Table 5.6: Reference point accuracy based on different distance ranges

<i>Point</i>	<i>Distance range in mm</i>			
	[0-5]	[0-10]	[0-15]	[0-20]
p1	67%	100%	100%	100%
p2	67%	87%	94%	100%
p3	60%	94%	100%	100%
p4	20%	74%	87%	94%
p5	47%	94%	100%	100%

5.6. Conclusion

In this chapter, a scheme to automatically identify the reference points for evaluation of pelvic organ prolapse (POP) using MRI has been presented. The points located on the pubic bone were identified by segmenting the pubic bone and then identifying its reference points. The segmentation of bones on MRI is a challenging task due to weak boundaries and inhomogeneity. To overcome this problem, a multi-stage segmentation mechanism using texture-based

classification, leak detection, and prior shape information is presented. The reference points of the pubic bone were identified using morphological skeleton operation whereas the points located on the vertebra were identified by intersecting point detection methods. Experiments demonstrate that the presented method provides more accurate and faster segmented regions compared to other commonly used segmentation methods. The point identification process is also accurate, faster and consistent compared with the process of manual point identification by experts. The presented method aims to overcome the current limitations of manually identifying points and measurements on MRI and to enable high throughput image analysis.

Chapter 6

Prediction Model for the Diagnosis of POP

This chapter presents a prediction model using support vector machines with correlation analysis based feature selection to improve pelvic organ prolapse classification. The image based features extracted through the techniques presented in Chapters 4 and 5 will be tested with clinical information to build a prediction model for pelvic organ prolapse diagnosis.

6.1. Overview of the Prediction Model

Previous studies that analyze the correlation between clinical and MRI measurements for POP diagnosis have been limited. Moreover, these studies used few features (variables) based on commonly used MRI reference lines such as PCL and MPL. Although previous studies have found a good correlation between clinical and MRI measurements for anterior and apical prolapse, no correlation has been found for posterior prolapse. Therefore, there is a major need to investigate the correlation between clinical and MRI-based features as well as to test new MRI-based features that can potentially improve the prediction of prolapse, particularly for posterior prolapse.

The main objective of this research is to build a prediction model using Support Vector Machines (SVM) that analyzes clinical and new MRI-based features to improve the diagnosis of POP. The proposed MRI-based features were extracted using previously developed automated pelvic floor measurement model [113, 124]. The significant features, both clinical and MRI based are selected using correlation analysis with 95% significance level. The proposed

prediction model will allow the use of imaging technology to predict the development of POP in predisposed patients, and possibly lead to the development of preventive strategies. Additionally, it is expected that this quantitative prediction model will enable more accurate diagnosis of POP.

6.2. Material and Methods

6.2.1. Data Acquisition

This retrospective study used the data of 207 women with different types and stages of pelvic organ prolapse from the database of the University of South Florida Division of Female Pelvic Medicine and Reconstructive Surgery within the Department of Obstetrics and Gynecology. The study was approved by the Institutional Review Board at the University of South Florida. The data collected from the database for each patient consists of demographic information, clinical history, POP-Q outcomes, and dynamic MRI-based features (see APPENDIX). Each patient had been assigned to particular types of prolapse (anterior, apical, and posterior), and their corresponding stage of prolapse (stage 0 through stage 4) using the POP-Q system. It was ensured that only patients with complete data were selected for this study.

The characteristics of the studied group are shown in Table 6.1. Variables include age, body mass index, parity, gravidity, number of vaginal deliveries, and number of caesarean deliveries. As shown in the table, 28% of the patients were between 56-65 years old, 25% of them were between 66-75 years old, and 23% of patients were between 46-55 years old. Only 2% of the patients were younger than 35 years old. Table 6.2 shows the distribution of prolapse cases with their corresponding stages for the studied group. For anterior and posterior prolapse, the majority of the patients are in the stages 2 and 3. On the other hand, the majority of the

patients with apical prolapse are in the stages 0 and 1. In this study, prolapse cases were defined as those with stage 2, 3, or 4 whereas controls were defined as those with stage 0 or 1.

Table 6.1: Patient characteristics

	Control (Stages 0-1)			Prolapse (Stages 2-3-4)		
Variables	Anterior (n=57)	Apical (n=151)	Posterior (n=58)	Anterior (n=150)	Apical (n=56)	Posterior (n=149)
Age	57.5±11.3	57.1±12.2	58.9±12.0	58.2±11.9	60.6±10.0	57.7±11.7
Body mass index (kg/m ²)	27.5±6.1	27.8±5.7	26.0±6.2	27.4±5.6	26.6±5.8	28.0±5.5
Parity	2.5±1.3	2.6±1.3	2.5±1.2	2.6±1.3	2.6±1.4	2.7±1.4
Gravidity	3.3±1.8	3.2±1.7	3.1±1.8	3.2±1.7	3.3±1.8	3.3±1.7
Number of vaginal deliveries	2.4±1.4	2.5±1.3	2.3±1.2	2.5±1.3	2.6±1.4	2.6±1.4
Number of caesarean deliveries	0.2±0.5	0.1±0.5	0.2±0.5	0.1±0.4	0.0±0.2	0.1±0.4

Table 6.2: Distribution of prolapse cases with their corresponding stages for the studied group

Stage	Anterior Prolapse	Apical Prolapse	Posterior Prolapse
0	2% (4)	10% (20)	2% (4)
1	26% (53)	63% (131)	26% (53)
2	24% (48)	6% (11)	38% (80)
3	39% (83)	12% (22)	27% (56)
4	9% (19)	9% (19)	7% (14)
TOTAL	100% (207)	100% (207)	100% (207)

The dynamic MRI data was de-identified and stored on a secure research computer for analysis. MR imaging was performed on a 3-Tesla GE system (General Electric Company, GE Healthcare, Buckinghamshire, UK) using an 8-channel torso phased-array coil with the patient in a modified dorsal lithotomy position. Prior to imaging, 60ml of ultrasound gel was placed in the rectum for improved visualization. Dynamic imaging was performed in a multiphase, single-slice sequence. The images were acquired in the midsagittal plane for 23-27 seconds, using a T2-weighted single-shot fast-spin echo sequence. Patients were coached, prior to imaging, on

performance of an adequate valsalva maneuver. The image data has been preprocessed and de-identified.

After acquiring the images, new and commonly used MRI-based image features were extracted from the images using previously developed automated pelvic floor measurement model (15-17). Previous MRI studies have mostly used PCL and MPL lines for the radiological assessment of POP. In this study, additional reference lines and angles are introduced and analyzed: true conjugate line (TCL), obstetric conjugate line (OCL), and diagonal conjugate line (DCL), angle between diagonal conjugate line and PCL, and angle between obstetric conjugate line and MPL as shown in Figure 6.1(b). These reference lines may provide additional insight on the correlation between MRI-based measurements and clinical information due to differences in pelvic configuration.

The following sections provide the description for extracting the MRI-based features using the proposed model, and for building the prediction model with clinical and MRI-based features for POP diagnosis.

6.2.2. Methods

6.2.2.1. Automatic Extraction of MRI-based Features

Prior to MRI-based feature extraction, MR images were pre-processed to reduce image noise, and to improve image contrast. Image noise reduction was performed by applying a convolution operation with a Gaussian smoothing kernel. Then, contrast stretching (image normalization) was performed to provide better intensity spread of pixels and to adjust de-noised images to gain better contrast. Finally, the images were calibrated to enable the gathering of real measurement values.

The proposed reference lines and angles were automatically extracted from MRI using previously developed pelvic floor measurement model. The model automatically identifies multiple bone structures on MRI and then extracts MRI-based features (lines, measurements, and angles) [113, 124].

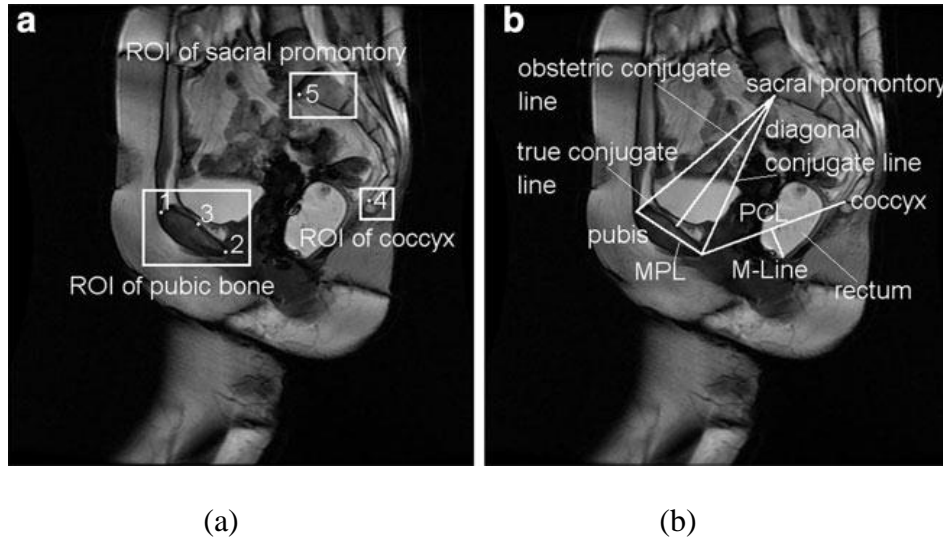


Figure 6.1: Region of interests and proposed MRI-based features. (a) Regions of interest, (b) Current and proposed MRI-based features

6.2.2.2. Prediction Model

A prediction model was built to analyze clinical and MRI-based features to differentiate patients with and without prolapse (anterior, apical, or posterior). The model is a two-class prediction model trained using SVM with significant feature subset selection process. SVM was selected as it has shown to achieve the highest classification accuracy for medical diagnosis compared to other classification techniques [113, 124].

The significant features, both clinical and MRI based were selected using correlation analysis. Pearson's correlation coefficient is used to measure the linear association between variables and is defined as follows:

$$\text{corr}(x, y) = \frac{\text{covariance}(x, y)}{\text{standart deviation}(x) * \text{standart deviation}(y)} = \frac{S_{xy}}{S_x S_y} \quad (6.1)$$

After selecting the best descriptive set of features, a classifier for each type of prolapse using SVM is built. The classification involves two steps: construction of the classifier and prediction. The dataset was divided into a training dataset and testing dataset for the prediction model. In the first step, a classifier structure is constructed based on the training data set using SVMs. SVMs is trained using the “kernel trick”, which allows the algorithm to fit the maximum margin hyperplane in a transformed feature space to provide for non-linear decision surface. The training vectors $x_i, i = 1, 2, \dots, L$ are nonlinearly mapped onto a high-dimensional feature space by $\Phi: \mathbb{R}^M \mapsto \mathcal{F}$ and then a linear separation is attempted in \mathcal{F} . If \mathcal{F} is a Hilbert space, K is a kernel function in the original space \mathbb{R}^M that describes the inner product in \mathcal{F} .

$$\Phi(u) \cdot \Phi(v) = K(u, v) = (u \cdot v + 1)^2 \quad (6.2)$$

where $K(u, v)$ should satisfy Mercer’s condition that ensures that the kernel function can always be expressed as the dot product between two input vectors in high dimensional space. This transformed space of the SVM kernels is called a reproducing kernel Hilbert space. The Radial Basis Function kernel (RBF) was employed in the training process to construct nonlinear SVMs and is described as follows:

$$K(u, v) = \exp(-\gamma ||u - v||^2) \quad (6.3)$$

There are two parameters for an RBF kernel that need to be determined: C representing the penalty parameter and γ representing the RBF sigma parameter. 10-fold cross validation is used in this study to identify the best (C, γ) so that the classifier can accurately predict unknown data. After the cases are trained according to the selected features, the second step of the prediction model is to apply the model to test cases in the testing dataset using the built SVM classifier. The anticipated outcome at the end of this process is a set of two groups of cases that are automatically classified as prolapse group and control group.

6.3. Results

A total of sixty-one (61) clinical and MRI-based features were collected and analyzed in this study. For each type of POP, the significant features were identified using correlation coefficient (r) at 95% significant level. As shown in Tables 6.3-6.5, the set of significant features vary based on the type of POP. For instance, body mass index < 20 ($r = -0.1879$; $p = 0.0067$) was found to be significant for posterior prolapse but not for anterior or apical prolapse. Ethnicity (Caucasian) ($r = -0.2002$; $p = 0.0038$) was found to have an impact on apical prolapse but not on anterior or posterior prolapse. As shown in the tables, the proposed MRI-based features were also found to be significant in the prediction of the different types of prolapse. H-Line anterior ($r = 0.4339$; $p = 0.0003$), H-Line apical ($r = 0.3489$; $p = 0.0021$), and the angle between TCL and MPL ($r = 0.1337$; $p = 0.0154$) have an impact in the assessment of anterior prolapse whereas H-Line posterior ($r = 0.2355$; $p = 0.006$) and the angle between DCL and PCL ($r = 0.1239$; $p = 0.014$) were found to impact the prediction of posterior prolapse. Only H-Line anterior ($r = 0.2654$; $p = 0.0011$) and H-Line apical ($r = 0.3775$; $p = 0.0002$) were found to be significant MRI-based features in the assessment of apical prolapse.

Table 6.3: Significant features for anterior prolapse

Clinical features:	correlation coefficient (r)	p value
# of Vaginal delivery= 2	0.1606	0.0208
# of Cesarean delivery= 2	-0.1492	0.0320
Hysterectomy-Abdominal incision	-0.1995	0.0040
Hysterectomy-Laparoscopic	-0.1432	0.0395
Hysterectomy-Vaginal	-0.1730	0.0127
Sacrocolpopexy	-0.2692	0.0087
MRI-based features:		
H-Line Anterior	0.4339	0.0003
H-Line Apical	0.3489	0.0021
Angle between TCL and MPL	0.1337	0.0154

Table 6.4: Significant features for apical prolapse

Clinical features:	correlation coefficient (r)	p value
Ethnicity-Caucasian	-0.2002	0.0038
Hysterectomy-Abdominal incision	-0.2155	0.0018
Rectocele (posterior) repair-Graft augmentation	0.1515	0.0293
MRI-based features:		
H-Line Anterior	0.2654	0.0011
H-Line Apical	0.3775	0.0002

Table 6.5: Significant features for posterior prolapse

Clinical features:	correlation coefficient (r)	p value
35<=Age<45	0.1715	0.0135
BMI<20	-0.1879	0.0067
Sacrocolpopexy	-0.1539	0.0268
Rectocele (posterior) repair_Traditional	-0.1510	0.0298
MRI-based features:		
H-Line Posterior	0.2355	0.006
Angle between DCL and PCL	0.1239	0.014

Table 6.6 shows the distribution of cases for the training and testing datasets for each type of prolapse. Then, Table 6.7 shows the distribution of prolapse stages within the testing and training datasets per type of prolapse. The prediction model was trained using SVM. For anterior prolapse, the model was trained using the data from 138 cases (100 prolapse cases, 38 controls). After training the classifier based on the selected clinical and MRI-based features, the testing process was performed on 69 cases (50 prolapse cases, 19 controls). Similarly, the prediction model was trained for apical prolapse with 138 cases (37 prolapse cases, 101 controls) and the testing process was performed with 69 cases (19 prolapse cases, 50 controls). Finally, for posterior prolapse, the model was trained with 136 cases (98 prolapse cases, 38 controls) and tested on 71 cases (51 prolapse cases, 20 controls).

Table 6.6: The distribution of cases for the training and testing datasets for each type of prolapse

Groups	Training Dataset	Testing Dataset	TOTAL
Prolapse			
Anterior	100	50	150
Apical	37	19	56
Posterior	98	51	149

Table 6.6 (Continued)

Control			
Anterior	38	19	57
Apical	101	50	151
Posterior	38	20	58

Table 6.7: The distribution of prolapse stages within the testing and training datasets

	Training Dataset					Testing Dataset					
	CONTROL		PROLAPSE			CONTROL		PROLAPSE			
Type of prolapse	Stage 0	Stage 1	Stage 2	Stage 3	Stage 4	Stage 0	Stage 1	Stage 2	Stage 3	Stage 4	
Anterior	2	36	32	56	12	2	17	16	28	6	207
Apical	13	88	9	16	12	7	43	4	9	6	207
Posterior	2	36	52	36	10	2	18	28	18	5	207

The prediction model is validated using correct rate, which is the percentage of cases correctly classified. Table 6.8 provides the accuracy comparison between the prediction model that uses only clinical features, prediction model that uses only MRI-based features, and the prediction model that uses both clinical and new MRI-based features. As can be seen in the table, incorporating the newly proposed MRI-based features increases the prediction accuracy of all types of prolapse. This improvement is especially noticeable on posterior prolapse where the incorporation of the new MRI-based features increased the correct rate from 47% to 80%. The significant clinical features for posterior prolapse were found to be: age ($35 \leq \text{Age} < 45$) ($r = 0.1715$; $p = 0.0135$), body mass index $< 20 \text{ kg/m}^2$ ($r = -0.1879$; $p = 0.0067$), rectocele (posterior) repair with traditional method ($r = -0.1510$; $p = 0.0298$), and sacrocolpopexy ($r = -0.1539$; $p = 0.0268$). The significant MRI-based features for posterior prolapse are H-Line ($r = 0.2654$; $p = 0.00114$) and the angle between DCL and PCL ($r = 0.1239$; $p = 0.014$).

For anterior prolapse, the model correctly predicted 91% of the cases using clinical and MRI-based features. Clinical features found to be significant include: # of Vaginal delivery=2 ($r = 0.1606$; $p = 0.0208$), # of Cesarean delivery=2 ($r = -0.1492$; $p = 0.0320$), Hysterectomy-Abdominal incision ($r = -0.1995$; $p = 0.0040$), Hysterectomy-Laparoscopic ($r = -0.1432$; $p = 0.0395$),

Hysterectomy-Vaginal ($r=-0.1730$; $p=0.0127$), Sacrocolpopexy ($r=-0.2692$; $p=0.0087$) whereas MRI-based features include H-Line anterior ($r=0.4339$; $p=0.0003$), H-Line apical ($r=0.3489$; $p=0.0021$), and the angle between TCL and MPL ($r=0.1337$; $p=0.0154$). Finally, for apical prolapse, 89% of the cases were correctly predicted using both clinical and MRI-based features. Significant clinical features for apical prolapse were found to be Ethnicity-Caucasian ($r=-0.2002$; $p=0.0038$), Hysterectomy-Abdominal incision ($r=-0.2155$; $p=0.0018$), and Rectocele (posterior) repair-Graft augmentation ($r=0.1515$; $p=0.0293$). H-Line anterior ($r=0.2654$; $p=0.0011$) and H-Line apical ($r=0.3775$; $p=0.0002$) were found to be significant MRI-based features for apical prolapse. Results show that the proposed prediction model can predict cases with anterior prolapse with very high accuracy (> 0.90), and apical and posterior prolapse with good accuracy ($0.80 - 0.90$).

Table 6.8: Accuracy of the proposed prediction model for different types of prolapse and different types of features

Type of prolapse	Correct rate (ONLY clinical features)	Correct rate (ONLY MRI based features)	Correct rate (BOTH clinical and MRI based features)
Anterior	82	56	91
Apical	83	53	89
Posterior	47	52	80

6.4. Conclusion

In this study, we presented a prediction model that fuses clinical and new MRI-based features to improve the diagnosis of POP. The prediction model uses Support Vector Machines and selects significant features using correlation analysis at 95% significant level. Results demonstrate that our prediction model using both clinical and new MRI-based features achieves higher classification accuracy compared to using only clinical features. Our analysis showed that two newly proposed MRI-based features: the angle between TCL and MPL, and the angle

between DCL and PCL have a significant impact in the prediction of anterior and posterior prolapse, respectively. For posterior prolapse, the consideration of the new MRI-based features significantly increased the prediction accuracy from 47% to 80%.

Chapter 7

Discussion and Future Work

In this chapter, the techniques developed in this research and the findings are summarized. Future research directions are proposed.

7.1. Discussion

In this dissertation, a fully automated bone localization and segmentation algorithm to predict pelvic organ prolapse is presented. This model can be applied to pelvic floor structures on MRI in the presence of image inhomogeneity and noise. In general, the presented methods offer the following:

An automated bone localization model that integrates local and global information to locate the bounding boxes of bone structures on MRI using support vector machines and non-linear regression is presented in Chapter 4. The main contribution of this scheme is a new parameterization paradigm through a non-linear regression approach for the multiple-bone localization problem on MRI. The location of the pubic bone is determined based on the relative location with respect to the pelvic organs and using a support vector machine based classification with texture features. The coccyx and sacral promontory are located using a non-linear regression model. Results demonstrate that the proposed scheme can accurately and consistently find the locations of the pubic bone, coccyx, and sacral promontory on MRI. Center error between automatically and manually identified pubic bone regions has been found to be lower than those for coccyx and sacral promontory. The reason is that local information of the pubic

bone is incorporated into the localization process along with the global information. The advantages of the proposed method are that it is robust and fully automated. It uses human anatomic information, such as relative positions of the anatomical structures to find the bone structures. Images of subjects with unusual health conditions may affect the effectiveness of the proposed method in finding the bone structures.

A new segmentation approach that provides leak detection for automating pelvic bone point identification on MRI is also presented in Chapter 5. The points located on the pubic bone are identified by segmenting the pubic bone and then identifying its reference points. The segmentation of bones on MRI is a challenging task due to weak boundaries and inhomogeneity. To overcome this problem, a multi-stage segmentation mechanism using texture-based classification, leak detection, and prior shape information is presented. The reference points of the pubic bone were identified using morphological skeleton operation whereas the points located on the vertebra are identified by intersecting point detection methods. Experiments demonstrate that the presented method provides more accurate and faster segmented regions compared to other commonly used segmentation methods. The point identification process is also accurate, faster and consistent compared with the process of manual point identification by experts. The presented method aims to overcome the current limitations of manually identifying points and measurements on MRI and to enable high throughput image analysis.

In Chapter 6, a model is designed to improve the diagnosis of POP by building a prediction model using SVM and incorporating new MRI-based features with clinical features. Results show that the proposed prediction model is able to accurately classify the testing cases into prolapse or control group. Prediction accuracies for anterior and apical prolapse are higher than posterior prolapse since the correlation between features and POP-Q information is lower

for posterior prolapse. The analysis showed that the newly proposed MRI-based features have a significant impact in the prediction of prolapse cases, particularly for posterior prolapse. These features are the angle between TCL and MPL for predicting anterior prolapse while the angle between DCL and PCL for predicting posterior prolapse. One of the strengths of this study is the large number of cases in the studied group. A total of 207 women with different types and stages of pelvic organ prolapse were analyzed in this study. Using a large number of cases for training the model provides a more powerful prediction model. Other strength of the study is that these cases are selected by a third party so there was no bias on the selection of the studied group. Finally, the proposed prediction model proposes and uses new MRI-based features. Previous studies have investigated the correlation between clinical features with PCL and MPL. However, correlation of these features with the clinical features was limited on posterior prolapse. Incorporating the new MRI-based features increases the prediction accuracy of posterior prolapse to 80% compared with using clinical features only (47%).

7.2. Future Work

Even though the proposed methods achieve good results for bone localization and segmentation on MRI, pelvic floor measurement identification, and prediction of pelvic organ prolapse, there is still room to improve the performance of these models.

For the automated bone localization model, the results demonstrate that the proposed scheme can accurately find the location of the pubic bone. However, the accuracy for both sacral promontory and coccyx are lower than for the pubic bone. The reason is that both local and global information is used to find the pubic bone region, while only global information was used for sacral promontory and coccyx. There is a need for investigating the use of local information

to improve the localization of the sacral promontory and coccyx regions. This is expected to improve and facilitate the accuracy of the detected regions.

Finally, although the proposed prediction model significantly increases the prediction accuracy of posterior prolapse to 80% compared with using clinical features only (47%), the incorporation of additional MRI-based features may increase the prediction accuracy. In the future, these MRI-based features will be investigated. Another item that will be considered is a prediction model for multiple POP stages. The current SVM based prediction model was designed for two-class prediction (prolapse or no prolapse). Future work will address the classification of cases into different stages of prolapse (stage 0 to stage 4) to provide more detailed diagnosis of POP. The study can also be further extended by investigating how findings of the proposed prediction model are correlated with post-operative information.

References

- [1] P. Dallenbach, Kaelin-Gambirasio, I., Jacob, S., Dubuisson, J.B., Boulvain, M., "Incidence rate and risk factors for vaginal vault prolapse repair after hysterectomy," *IntUrogynecol J*, vol. 19, pp. 1623-1629, 2008.
- [2] L. L. Subak, Waetjen, L. E., van den Eeden, S., Thom, D. H., Vittinghoff, E., Brown, J. S., "Cost of pelvic organ prolapse surgery in the United States," *Obstet Gynecol*, 2001, vol. 98, pp. 646-651, 2001.
- [3] L. Mouritsen, Larsen, J. P., "Symptoms, bother and POPQ in women referred with pelvic organ prolapse," *Int Urogynecol J Pelvic Floor Dysfunct.*, vol. 14, pp. 122-127, 2003.
- [4] U. C. Bureau. (2010, August 9.). *US interim projections by age, sex, race and Hispanic origins: 200-2050*. Available: <http://www.census.gov/ipc/www/usinterimproj/>
- [5] R. C. Bump, Mattiasson, A., Bo, K., Brubaker, L. P., DeLancey, J. O. L., Klarskov, P., Shull, B. L., Smith, A. R. B., "The Standardization of Terminology of Female Pelvic Organ Prolapse and Pelvic Floor Dysfunction," *Am J Obstet Gynecol*, vol. 175, pp. 10-17, 1996.
- [6] H. S. Fayyad A, Gurung V, Prashar S, Smith A, "How accurate is symptomatic and clinical evaluation of prolapse prior to surgical repair?," *Int Urogynecol J*, vol. 18, pp. 1179–1183, 2007.
- [7] D. Altman, Lopez, A., Kierkegaard, J., Zetterstrom, J., Falconer, C., Pollack, J., Mellgren, A., "Assessment of Posterior Vaginal Wall Prolapse: Comparison of Physical Findings to Cystodefecoperitoneography," *Int Urogynecol J Pelvic Floor Dysfunct*, vol. 16, pp. 96-103, 2005.
- [8] A. M. Agildere, Tarhan, N. C., Ergeneli, M. H., Yologlu, Z., Kurt, A., Akgun, S., Kayahan, E. M., "MR rectography evaluation of rectoceles with oral gadopentetate dimeglumine and polyethylene glycol solution," *Abdom Imaging*, vol. 28, pp. 28-35, 2003.
- [9] H. S. Kaufman, Buller, J. L., Thompson, J. R., Pannu, H. K., DeMeester, S. L., Genadry, R. R., Bluemke, D. A., Jones, B., Rychcik, J. L., Cundiff, G. W., "Dynamic pelvic magnetic resonance imaging and cystocolpoproctography alter surgical management of pelvic floor disorders," *Dis Colon Rectum* vol. 44, pp. 1575-1583, 2001.
- [10] A. M. Weber, Walters, M. D., Piedmonte, M. R., Ballard, L. A., "Anterior colporrhaphy: A randomized trial of three surgical techniques," *Am. J. Obstet. Gynecol.*, vol. 185, pp. 1299-1306, 2001.

- [11] S. R. Broekhuis, Futterer, J. J., Barentsz, J. O., Vierhout, M. E., "A systematic review of clinical studies on dynamic magnetic resonance imaging of pelvic organ prolapse: the use of reference lines and anatomical landmarks," *Int Urogynecol J Pelvic Floor Dysfunct*, vol. 20, pp. 721-729, 2009.
- [12] C. A. Woodfield, Hampton, B. S., Sung, V., Brody, J. M., "Magnetic resonance imaging of pelvic organ prolapse: comparing pubococcygeal and midpubic lines with clinical staging," vol. 20, pp. 695-701, 2009.
- [13] A. C. Lienemann A., Baron A., Kohn P., Reiser M., "Dynamic MR colpocystorectography assessing pelvic floor descent," *Eur Radiol* vol. 7, pp. 1309-1317, 1997.
- [14] H. S. Goh V., Kaplan G., Healy J.C., Bartram C.I. , "Dynamic MR imaging of the pelvic floor in asymptomatic subjects," *AJR Am J Roentgenol*, vol. 174, pp. 661-666, 2000.
- [15] M. M. Lakeman, Zijta, F. M., Peringa, J., Nederveen, A. J., Stoker, J., Roovers, J. P., "Dynamic magnetic resonance imaging to quantify pelvic organ prolapse: reliability of assessment and correlation with clinical findings and pelvic floor symptoms," *Int. Urogynecol J.* , vol. 23, pp. 1547-1554, 2012.
- [16] C. J. Robinson, Swift, S., Johnson, D. D., Almeida, J. S., "Prediction of pelvic organ prolapse using an artificial neural network," *American Journal of Obstetrics and Gynecology*, pp. 193.e1 – 193.e6, 2008.
- [17] C. Wallner, "Levator ani has a crucial role in the maintenance of continence," *European Urology Supplements*, vol. 55, pp. 932-944, 2009.
- [18] R. C. Bump, Mattiasson, A., Bo, K. , "The standardization of terminology of female pelvic organ prolapse and pelvic floor dysfunction," *Am. J. Obstet. Gynecol.*, vol. 175, 1996.
- [19] C. Persu C., C.R., Cauni, V., Gutue, S., Geavlete, P., "Pelvic Organ Prolapse Quantification System (POP-Q) – a new era in pelvic prolapse staging " *J Med Life*, vol. 4, pp. 75-81, 2011.
- [20] E. M. Hecht, Lee, V. S., Tanpitukpongse, T. P., Babb, J. S., Taouli, B., Wong, S., Rosenblum, N., et al, "MRI of pelvic floor dysfunction: dynamic true fast imaging with steady-state precession versus HASTE," *Ajr American Journal Of Roentgenology*, vol. 191, pp. 352-358, 2008.
- [21] V. Goh, Halligan, S., Kaplan, G., Healy, J. C., Bartram, C. I. , "Dynamic MR imaging of the pelvic floor in asymptomatic subjects," *AJR Am J Roentgenol*, vol. 174, pp. 661-666, 2000.
- [22] H. S. Healy J.C., Reznick R.H., "Dynamic MR imaging compared with evacuation proctography when evaluating anorectal configuration and pelvic floor movement," *AJR Am J Roentgenol* vol. 169, pp. 775-779, 1997.

- [23] A. E. Gousse, Barbaric, Z. L., Safir, M. H., Madjar, S., Marumoto, A.K., Raz, S. , "Dynamic half Fourier acquisition, single shot turbo spin-echo magnetic resonance imaging for evaluating the female pelvis," *J Urol*, vol. 164, pp. 1606-1613, 2000.
- [24] S. D. Lienemann A., Janssen U., Grosch E., Pellengahr C., Anthuber C., "Assessment of pelvic organ descent by use of functional cine-MRI: which reference line should be used? ," *Neurourol Urodyn* vol. 23, pp. 33-37, 2004.
- [25] H. D. S. Kelvin F.M., Maglinte D.D., Patten B.J., Benson J.T. , "Female pelvic organ prolapse: diagnostic contribution of dynamic cystoproctography and comparison with physical examination," *AJR Am J Roentgenol* vol. 173, pp. 31-37, 1999.
- [26] Z. E. Fauconnier A., Abichedid J., Bader G., Falissard B., Fritel X., "Dynamic magnetic resonance imaging for grading pelvic organ prolapse according to the international continence society classification: Which line should be used? ," *Neurourol Urodyn* vol. 27, pp. 191-197, 2007.
- [27] K. Pannu, H., Scatarige, C.,J., Eng, J., "MRI Diagnosis of Pelvic Organ Prolapse Compared with Clinical Examination," *Academic Radiology*, vol. 18, pp. 1245-1251, 2011.
- [28] E. Cortes, Reid, W.,M., N., Singh, K., Berger, L., "Clinical Examination and Dynamic Magnetic Resonance Imaging in Vaginal Vault Prolapse," *Obstetrics & Gynecology*, vol. 103, pp. 41-46, 2004.
- [29] C. J. Robinson, Swift, S., Johnson, D. D., Almeida, J. S. , "Prediction of pelvic organ prolapse using an artificial neural network," *Am J Obstet Gynecol*, vol. 199, pp. 191-193, 2008.
- [30] U. Kurkure, Avila-Montes, O.C., Kakadiaris, I.A., "Automated segmentation of thoracic aorta in non-contrast CT images," presented at the IEEE Intl. Symp. Biomedical Im., 2008.
- [31] B. Van Ginneken, Baggerman, W., van Rikxoort, E. M., "Robust segmentation and anatomical labeling of the airway tree from thoracic CT scans," presented at the MICCAI, 2008.
- [32] H. A. Vrooman, Cocosco, C.A., "kNN-based Multi-spectral MRI Brain Tissue Classification: Manual Training versus Automated Atlas-based Training," in *Proceedings of the SPIE Medical Imaging*, California, USA, 2006.
- [33] M. Fenchel, Thesen, S., Schilling, A., "Automatic labeling of anatomical structures in MR fastview images using a statistical atlas," *MICCAI*, 2008.
- [34] A. Shimizu, Ohno, R., Ikegami, T., Kobatake, H., "Multi-organ segmentation in three-dimensional abdominal CT images," *Int. J CARS*, vol. 1, 2006.

- [35] X. Han, Hoogeman, M.S., Levendag, P.C., Hibbard, L.S., Teguh, D.N., Voet, P., Cowen, A.C., Wolf, T.K., "Atlas-based auto-segmentation of head and neck CT images," presented at the MICCAI, New York, NY, USA, 2008.
- [36] X. Zhuang, Rhode, K., Arridge, S., Razavi, R., Hill, D., Hawkes, D., Ourselin, S., "An atlas-based segmentation propagation framework using locally affine registration-application to automatic whole heart segmentation," presented at the MICCAI, New York, NY, USA, 2008.
- [37] Y. Freund, Schapire, R. , "A Decision-Theoretic Generalization of on-Line Learning and an Application to Boosting," *Journal of computer and system sciences.*, vol. 55, pp. 119-139, 1997.
- [38] M. Freiman, Edrei, Y., Shmidmayer, Y., Gross, E., Joskowicz, L., Abramovitch, R., "Classification of liver metastases using MRI images: A machine learning approach," presented at the MICCAI, 2008.
- [39] M. Dolejst, Kybic, J., Tuma, S., Polovincak, M., "Reducing false positive responses in lung nodule detector system by asymmetric adaboost," presented at the ISBI, 2008.
- [40] M. Prasad, Sowmya, A., "Multi-level classification of emphysema in HRCT lung images using delegated classifiers," presented at the MICCAI, 2008.
- [41] Y. Zhan, Zhou, X.S., Peng, Z., Krishnan, A., "Active scheduling of organ detection and segmentation in whole-body medical images," presented at the MICCAI, 2008.
- [42] Z. Tu, Narr, K.L., Dollar, P., Dinov, I., Thompson, P.M., Toga, A.W., "Brain anatomical structure segmentation by hybrid discriminative/generative models.," *IEEE Trans. on Medical Imaging*, vol. 27, 2008.
- [43] K. M. Pohl, Bouix, S., Nakamura, M., Rohling, T., McCarley, R.W., Kikinis, R., Grimson, W.E.L., Shenton, M.E., Wells, W.M., "A hierarchical algorithm for MR brain image parcelation," *IEEE Trans. on Medical Imaging*, vol. 26, 2007.
- [44] Y. Zheng, Barbu, A., Georgescu, B., Scheuering, M., Comaniciu, D., "Four-chamber heart modeling and automatic segmentation for 3-D cardiac CT volumes using marginal space learning and steerable features," *IEEE Transactions on Medical Imaging* vol. 27, pp. 1668–1681, 2008.
- [45] Y. Zheng, Comaniciu, D., "Marginal Space Learning for Efficient Detection of 2D/3D Anatomical Structures in Medical Images," presented at the Information Processing in Medical Imaging, Williamsburg, VA, USA, 2009.
- [46] S. K. Zhou, Zhou, J., Comaniciu, D., "A boosting regression approach to medical anatomy detection," presented at the IEEE Conference on Computer Vision and Pattern Recognition, 2007.

- [47] A. Criminisi, Shotton, J., Robertson, D., Konukoglu, E., "Regression Forests for Efficient Anatomy Detection and Localization in CT Studies," presented at the MICCAI 2010.
- [48] R. Cuingnet, R. Prevost, D. Lesage, L. Cohen, B. Mory, and R. Ardon, "Automatic Detection and Segmentation of Kidneys in 3D CT Images Using Random Forests," in *Medical Image Computing and Computer-Assisted Intervention – MICCAI 2012*. vol. 7512, ed, 2012, pp. 66-74.
- [49] J. Mao, Jain, A., "Texture classification and segmentation using multiresolution simultaneous autoregressive models.," *Pattern Recognition*, vol. 25, pp. 173-188, 1992.
- [50] T. Hofmann, Puzicha, J., Buhmann, J., "Unsupervised texture segmentation in a deterministic annealing framework," *IEEE Transactions on Pattern Analysis and Machine Intelligence*, vol. 20 pp. 803-818, 1998.
- [51] L. O. Hall, Bensaid, A.M., Clarke, L.P., Velthuizen, R.P., Silbiger, M.S., Bezdek, J.C., "A comparison of neural network and fuzzy clustering techniques in segmenting magnetic resonance images of the brain. ," *IEEE Transactions on Neural Networks*, vol. 3 pp. 672-681, 1992.
- [52] A. Tremeau, Borel, N., "A region growing and merging algorithm to colour segmentation," *Pattern Recognition*, vol. 30, pp. 1191–1203 1997.
- [53] S. Hojjatoleslami, Kittler, J., "Region growing: A new approach," *IEEE Transactions on Image Processing*, vol. 7, pp. 1079-1084, 1998.
- [54] P. Bao, Zhang, L., Wu, X., "Canny edge detection enhancement by scale multiplication," *IEEE Transactions on Pattern Analysis and Machine Intelligence*, vol. 27, pp. 1485-1490, 2005.
- [55] P. Bao, Zhang, L., "Noise Reduction for Magnetic Resonance Images via Adaptive Multiscale Products Thresholding," *IEEE Transactions on Medical Imaging*, vol. 22, pp. 1089-1099, 2003 2003.
- [56] J. Canny, "A Computational Approach to Edge Detection," *IEEE Transactions on Pattern Analysis and Machine Intelligence*, vol. 8, pp. 679-698, 1986.
- [57] M. Unser, Aldroubi, A., and Laine, A., "Special Issue on Wavelets in Medical Imaging," *IEEE Transactions on Medical Imaging*, vol. 22, pp. 285-288, 2003.
- [58] L. Zhang, Bao, P., "Edge detection by scale multiplication in wavelet domain," *Elsevier Science B.V. Pattern Recognition letters*, pp. 1771-1784, 2002.
- [59] P. Chao, J., Lee, T.,F., Su, T.,J., Lee, C., Cho, M., Y.,Wang, C.,Y., "Boundary Finding Combining Wavelet and Markov Random Field Segmentation Based on Maximum Entropy Theory," presented at the 2009 Fourth International Conference on Innovative Computing, Information and Control, Kaohsiung, Taiwan 2009.

- [60] D. Flores-Tapia, Venugopal, N., Thomas, G., McCurdy, B., Ryner, L., Pistorius, S., "Real time MRI prostate segmentation based on wavelet multiscale products flow tracking,," in *32nd Annual International Conference of the IEEE, EMBS*, Buenos Aires, Argentina, 2010, pp. 5034-5037.
- [61] D. Terzopoulos, Fleischer, K., " Deformable models," *The Visual Computer*, vol. 4, pp. 306-331, 1988.
- [62] C. Davatzikos, Fan, Y., Wu, X., Shen, D., Resnick, S.M., "An Active Contour Model for Mapping the Cortex," *IEEE TRANSACTIONS ON MEDICAL IMAGING*, vol. 14, p. 65, 1995.
- [63] N. Ray, "Merging Parametric Active Contours Within Homogeneous Image Regions for MRI-Based Lung Segmentation," *IEEE Transactions on Fuzzy Systems Medical Imaging*, vol. 22, pp. 189-199, 2003.
- [64] T. Cootes, Taylor, C., Cooper, D. , "Cootes T, Taylor C, Cooper D et al. Active shape models - their training and application. Computer Vision and Image Understanding. 1995;61(1):38-59.," *Active shape models - their training and application*, vol. 61, pp. 38-59, 1995.
- [65] H. Ling, Zhou, S., Zheng, Y., "Hierarchical, learning-based automatic liver segmentation.,," presented at the Computer Vision and Pattern Recognition, 23-28 June 2008.
- [66] Y. Song, Bulpitt, A. J., Brodlie, K. W. , "Liver segmentation using automatically defined patient specific b-spline surface models," *MICCAI* (pp. 43-50, 2009.
- [67] Y. Zhen, Barbu, A., "Fast automatic heart chamber segmentation from 3d ct data using marginal space learning and steerable features," presented at the Conf. on Computer Vision (ICCV), 2007.
- [68] O. Ecabert, Peters, J., Schramm, H. , "Automatic model-based segmentation of the heart in ct images," *IEEE Trans. Med. Imaging*, vol. 27, pp. 1189-1201, 2008.
- [69] R. Toth, Sparks, R., Madabhushi, A. , "Medial axis based statistical shape model (massm): Applications to 3d prostate segmentation on MRI," presented at the IEEE International Symposium on Biomedical Imaging 2011.
- [70] L. Lorigo, "Segmentation of Bone in Clinical Knee MRI Using Based Geodesic Active Contours," presented at the MICCAI, 1998.
- [71] J. Fripp, Crozier, S., Warfield, S.K., Ourselin, S., "Automatic segmentation of the bone and extraction of the bone-cartilage interface from magnetic resonance images of the knee," *Phys. Med. Biol.* , vol. 52, pp. 1617-1631, 2007.
- [72] P. Bourgeat, Fripp, J., Stanwell, P., Ramadan, S., Ourselin, S., "MR image segmentation of the knee bone using phase information," *Med. Image Anal.*, vol. 11, pp. 325-335, 2007.

- [73] J. Schmid, Magnenat-Thalmann, N., "MRI bone segmentation using deformable models and shape priors," *Med. Image Comput*, pp. 119-126, 2008.
- [74] Y. Yin, Zhang, X., Sonka, M. , "Optimal multi-object multi-surface graph search segmentation: Full-joint cartilage delineation in 3d," *Proceedings of the Medical Image Understanding and Analysis*, S. McKenna and J. Hoey, Eds, pp. 104-108, 2008.
- [75] B. van Ginneken, Stegmann, M., Loog, M., "Segmentation of anatomical structures in chest radiographs using supervised methods: A comparative study on a public database. ," *Medical Image Analysis* vol. 10, pp. 19-40, 2006.
- [76] T. Porter, Green, B., "Identifying Diabetic Patients: A Data Mining Approach," in *Americas Conference on Information Systems*, 2009.
- [77] S. Panzarasa, Quaglini, S., "Data mining techniques for analyzing stroke care processes," in *13th World Congress on Medical Informatics*, 2010.
- [78] L. T. H. Li, Wu, Z., Gong, J., Gruidl, M., Zou, J., Tockman, M., Clark, R. A. , "Data mining techniques for cancer CRPIT Volume 121 - Data Mining and Analytics 2011 28detection using serum proteomic profiling," *Artificial Intelligence in Medicine*, Elsevier, 2004.
- [79] R. Das, Turkoglu, I., "Effective diagnosis of heart disease through neural networks ensembles.," *Expert Systems with Applications*, Elsevier, vol. 36, pp. 7675–7680, 2009.
- [80] V. A. Sitar-Taut, Zdrengea, D., "Using machine learning algorithms in cardiovascular disease risk evaluation," *Journal of Applied Computer Science & Mathematics.*, vol. 1, 2009.
- [81] G. Schwarzer, Vach, W., Schumacher, M. , "On the misuses of artificial neural networks for prognostic and diagnostic classification in oncology," *Stat. Med.*, vol. 19, pp. 541-561, 2000.
- [82] K. Polat, Gunes, S., "Breast cancer diagnosis using least square support vector machine," *Digital Signal Processing*, vol. 17, pp. 694-701, 2007.
- [83] A. Rajkumar, Reena, G. S., "Diagnosis Of Heart Disease Using Datamining Algorithm," in *Global Journal of Computer Science and Technology* vol. 10, ed, 2010.
- [84] C. Davatzikos, Fan, Y., Wu, X., Shen, D., Resnick, S. M. , "Detection of prodromal Alzheimer's disease via pattern classification of MRI," *Neurobiology of Aging*, vol. 29, pp. 514-523, 2008.
- [85] E. Duchesnay, Cachia, A., Roche, A., Rivie`re, D., Cointepas, Y., Papadopoulos-Orfanos, D., Zilbovicius, M., Martinot, J.-L., Re´gis, J., Mangin, J.F., "Classification based on cortical folding patterns," *IEEE Transactions on Medical Imaging*, vol. 26, pp. 553–565, 2007.

- [86] S. Kloppel, Stonnington, C.M., Chu, C., Draganski, B., Scahill, R.I., Rohrer, J.D., Fox, N.C., Jack, C. R., Ashburner, J., Frackowiak, R.S.J. , "Automatic classification of MR scans in Alzheimer's disease. *Brain*," *Epub*, vol. 131, pp. 681–689, 2008.
- [87] J. Padmavati, "A Comparative study on Breast Cancer Prediction Using RBF and MLP," *International Journal of Scientific & Engineering Research*, vol. 2, 2011.
- [88] M. U. Khan, Choi, J.P., Shin, H., Kim, M., "Predicting Breast Cancer Survivability Using Fuzzy Decision Trees for Personalized Healthcare," *IEEE Eng Med Biol Soc*, pp. 48-51, 2008.
- [89] C. Hinrichs, Singh, V., Xu, G., Johnson, S. C., "MKL for robust multi-modality AD classification," *International conference on medical image computing and computer assisted intervention*, pp. 786–794, 2009.
- [90] D. W. Zhang, Y., Zhou, L. Yuan, H., Shen, D., " Multimodal classification of Alzheimer's disease and mild cognitive impairment," *Neuroimage*, vol. 55, pp. 856-867, 2011.
- [91] T. Twellmann, Saalbach, A., Muller, C., Nattkemper, T.W., Wismuller, A. , "Detection of suspicious lesions in dynamic contrast-enhanced MRI data," *Engineering in Medicine and Biology Society* pp. 454-457, 2004.
- [92] C. A. Pena-Reyes, Sipper, M. , "A cooperative coevolutionary approach to fuzzy modeling," *IEEE Transactions on Fuzzy Systems*, vol. 9, pp. 727-737, 2001.
- [93] R. Setiono, "Generating concise and accurate classification rules for breast cancer diagnosis," *Artificial Intelligence in Medicine*, vol. 18, pp. 205-217, 2000.
- [94] E. D. Ubeyli, "Implementing automated diagnostic systems for breast cancer detection," *Expert Systems with Applications, Elsevier*, vol. 33, pp. 1054-1062, 2007.
- [95] M. F. Akay, "Support vector machines combined with feature selection for breast cancer " *Expert Systems with Applications, Elsevier*, vol. 36, pp. 3240-3247, 2009.
- [96] T. J. Hua, W., Dougherty, E. R., "Feature selection in the classification of highdimension data," presented at the EEE International Workshop on Genomic Signal Processing and Statistics, 2008.
- [97] X. Jin, Xu, A., Bie, R., Guo, P., "Title," unpublished|.
- [98] H. Peng, Long, F., Ding, C., "Feature selection based on mutual information criteria of max-dependency, max-relevance, and min redundancy," *IEEE Transactions on Pattern Analysis and Machine Intelligence*, vol. 27, pp. 1226-1238, 2005.
- [99] J. Biesiada, Duch, W. , "Feature selection for high-dimensional data—a Pearson redundancy based filter, " *Advances in Soft Computing*, vol. 45, pp. 242-249, 2008.

- [100] L. Rocchi, Chiari, L., Cappello, A. , "Feature selection of stabilometric parameters based on principal component analysis," *Medical and Biological Engineering and Computing*, vol. 42, pp. 71-79, 2004.
- [101] M. L. Raymer, Doom, T. E., Kuhn, L. A., Punch, W. F., "Knowledge Discovery in Medical and Biological Datasets Using a Hybrid Bayes Classifier/Evolutionary Algorithm," *IEEE Trans. systems, Man, and Cybernetics*, pp. 236-245, 2001.
- [102] A. Whitney, "A direct method of nonparametric measurement selection," *IEEE Trans. Computers*, vol. 20, pp. 1100-1103, 1971.
- [103] D. Goldberg, *Genetic Algorithms in Search, Optimization, and Machine Learning*: Addison Wesley, Reading, MA., 1989.
- [104] X. Wang, Yang, J., Teng, X., Xia, W., Richard, J., "Feature selection based on rough sets and particle swarm optimization," *Pattern Recognition Letters*, vol. 28, pp. 459-471, 2007.
- [105] M. Ronen, Jacob, Z., "Using simulated annealing to optimize feature selection problem in marketing applications," *European Journal of Operational Research*, vol. 171, pp. 842-858, 2006.
- [106] F. Tan, Fu, X., Wang, H., Zhang, Y., Bourgeois, A. , "A hybrid feature selection approach for microarray gene expression data, *Lecture Notes in Computer Science 3992* ", ed, 2006, pp. 678–685.
- [107] K. M. Shazzad, Park, J. S., "Optimization of intrusion detection through fast hybrid feature selection," in *Sixth International Conference on Parallel and Distributed Computing*, *IEEE Computer Society*, Washington, DC, USA, 2005, pp. 264–267.
- [108] M. Fatourechi, Birch, G., "Application of a hybrid wavelet feature selection method in the design of a self-paced brain interface system, ," *Journal of Neuroengineering and Rehabilitation*, vol. 4, 2007.
- [109] A. Karahaliou, Skiadopoulos, S., Boniatis, I., Sakellaropoulos, P., Likaki, E., Panayiotakis, G., Arikidis, N., Costaridou, L., "Breast cancer diagnosis: Analyzing texture of tissue surrounding microcalcifications," *IEEE Transactions on Information Technology in Medicine*, vol. 12, 2008.
- [110] S. Gould, Rodgers, J., Cohen, D., Elidan, G., Koller, D., "Multi-class Segmentation with Relative Location Prior," *Int. J. Comput. Vis.*, vol. 80, pp. 300-316, 2008.
- [111] C. W. Chen, Luo, J., Parker, K. J. , "Image segmentation via adaptive K-mean clustering and knowledge based morphological operations with biomedical applications " *IEEE Transactions on Image Processing*, vol. 7, pp. 1673-1683 1998.

- [112] S. Onal, Lai-Yuen, S., Hart, S., Bao, P., Weitzenfeld, A., "MRI-based Semi-Automatic Pelvimetry Measurement for Pelvic Organ Prolapse Diagnosis," in *ISSPA 2012*, Montreal, Quebec, Canada, 2012.
- [113] S. Onal, Lai-Yuen, S., Bao, P., Weitzenfeld, A., Hart, S., "Image based measurements for evaluation of pelvic organ prolapse," *Journal of Biomedical Science and Engineering*, vol. 6, pp. 45-55, 2013.
- [114] R. M. Haralick, Shapiro, L. G., "Survey of image segmentation techniques," *Computer Vision Graphics Image Process*, vol. 29, pp. 100-132., 1985.
- [115] S. M. Weiss, *Predictive Data Mining: A Practical Guide*. San Francisco, Ca: Morgan Kaufmann, 1998.
- [116] M. Steinbach, Karypis, G., Kumar, V. (2000). *A Comparison of Document Clustering Techniques*. (M. Grobelnik, D. Mladenic, & N. Milic-Frayling, Eds.)*KDD workshop on text mining*, 400(X), 1-2. *Ieee*. Available: <http://ieeexplore.ieee.org/lpdocs/epic03/wrapper.htm?arnumber=4721382>
- [117] C. Schmid, Mohr, R., Bauckhage, C., "Evaluation of interest point detectors," *International Journal of Computer Vision*, vol. 37, pp. 151–172, 2000.
- [118] N. Archip, Clatz, O., Whalen, S., "Non-rigid alignment of pre-operative MRI, fMRI, and DT-MRI with intra-operative MRI for enhanced visualization and navigation in image-guided neurosurgery," *Neuroimage* vol. 35, pp. 609-624, 2007.
- [119] R. Adams, Bischof, L., "Seeded region growing," *IEEE Trans. Pattern Anal. Machine Intell*, vol. 16, pp. 641-647, 1994.
- [120] T. F. Chan, Vese, L. A., "Active Contours Without Edges," *IEEE Transaction on Image Processing*, vol. 10, pp. 266-277, 2001.
- [121] Y. Y. Boykov, "Interactive graph cuts for optimal boundary & region segmentation of objects in N-D images " in *Computer Vision, 2001. ICCV 2001. Proceedings. Eighth IEEE International Conference on*, 2001, pp. 105 - 112
- [122] C. Li, "Distance Regularized Level Set Evolution and Its Application to Image Segmentation," *IEEE Transactions on Image Processing*, vol. 19, pp. 3243-3254, 2010.
- [123] S. Maghsoodloo, "Strengths and limitations of taguchi's contributions to quality, manufacturing, and process engineering.," *Manufacturing systems*, vol. 23, pp. 73-126, 2004.
- [124] S. Onal, Lai-Yuen, S., Bao, P., Weitzenfeld, A., Hart, S., "MRI based Segmentation of Pubic Bone for Evaluation of Pelvic Organ Prolapse," *IEEE Journal of Biomedical and Health Informatics*, vol. PP, 2013.

Appendices

Appendix A Data Acquisition Form

Table A.1: Data acquisition form

Clinical features:	Clinical sub-features	Feature #
Age		
	Age<35	1
	35≤Age<45	2
	45≤Age<55	3
	55≤Age<65	4
	65≤Age<75	5
	75≤Age	6
BMI(kg/m2)		
	BMI<20	7
	20≤BMI<25	8
	25≤BMI<30	9
	30≤BMI<35	10
	35≤BMI<40	11
	40≤BMI	12
Parity		
	0	13
	1	14
	2	15
	3	16
	4	17
	5	18
	5≤	19
Gravida		
	0	20
	1	21
	2	22
	3	23
	4	24
	5≤	25
Vaginal delivery		
	0	26
	1	27
	2	28
	3	29
	4	30
	5	31
	6≤	32
Caesarean Delivery		
	0	33
	1	34

Table A.1 (Continued)

	2	35
	3≤	36
Ethnicity		
	Caucasian	37
	African American	38
	Hispanic	39
Hysterectomy		
	Abdominal Incision	40
	Laparoscopic	41
	Vaginal	42
Uterosacral colpexy		
	Abdominal	43
	Laparoscopic	44
	Vaginal	45
Sacrospinous ligament fixation		46
Sacrocolpopexy		47
Cystocele (anterior) repair		
	Traditional	48
	Graft augmentation	49
Rectocele (posterior) repair		
	Traditional	50
	Graft augmentation	51
Incontinence Surgery		
	Burch/MMK	52
MRI-based features:		
H-Line	Anterior	53
	Apical	54
	Posterior	55
Distance Ratio		
	PCL/MPL	56
	TCL/MPL	57
	OCL/MPL	58
	DCL/MPL	59
Angle	between TCL and MPL	60
	between DCL and PCL	61

Appendix B IRB Approval



DIVISION OF RESEARCH INTEGRITY AND COMPLIANCE
Institutional Review Boards, FWA No. 00001669
12901 Bruce B. Downs Blvd., MDC035 • Tampa, FL 33612-4799
(813) 974-5638 • FAX (813) 974-5618

December 3, 2012

Stuart Hart, MD
Obstetrics and Gynecology
2 Tampa General Circle, 6th Floor
Tampa, FL 33606

RE: Not Human Research Activities Determination

Activity Title: MRI-based Pelvimetry Modeling for Pelvic Organ Prolapse Diagnosis
(Pro00007792)

Dear Dr. Hart:

I have reviewed the information you provided regarding the above referenced project and have determined the activities do not meet the USF definition of human subjects research activities; therefore, IRB approval is not required. If, in the future, you change this activity such that it becomes human subjects research activities, prior IRB approval is required. If you wish to obtain a determination about whether the activity, with the proposed changes, will be human research activities, please contact the IRB Office for further guidance.

All research activities, regardless of the level of IRB oversight, must be conducted in a manner that is consistent with the ethical principles of your profession and the ethical guidelines for the protection of human subjects. As principal investigator, it is your responsibility to ensure subjects' rights and welfare are protected during the execution of this project

We appreciate your dedication to the ethical conduct of human subject research at the University of South Florida and your continued commitment to human research protections. If you have any questions regarding this matter, please call 813-974-5638.

Sincerely,



E. Verena Jorgensen, MD, Chairperson
USF Institutional Review Board

Appendix C Copyright Permissions

This is copyright permission for use of material in Chapter 5.



RightsLink®

Home

Create Account

Help



Title: MRI based Segmentation of Pubic Bone for Evaluation of Pelvic Organ Prolapse
Author: Onal, S.; Lai-Yuen, S.; Bao, P.; Weitzenfeld, A.; Hart, S.
Publication: Biomedical and Health Informatics, IEEE Journal of
Publisher: IEEE
Copyright © 1969, IEEE

User ID

Password

☐ Enable Auto Login
LOGIN
[Forgot Password/User ID?](#)
If you're a copyright.com user, you can login to RightsLink using your copyright.com credentials. Already a **RightsLink user** or want to [learn more?](#)

Thesis / Dissertation Reuse

The IEEE does not require individuals working on a thesis to obtain a formal reuse license, however, you may print out this statement to be used as a permission grant:

Requirements to be followed when using any portion (e.g., figure, graph, table, or textual material) of an IEEE copyrighted paper in a thesis:

- 1) In the case of textual material (e.g., using short quotes or referring to the work within these papers) users must give full credit to the original source (author, paper, publication) followed by the IEEE copyright line © 2011 IEEE.
- 2) In the case of illustrations or tabular material, we require that the copyright line © [Year of original publication] IEEE appear prominently with each reprinted figure and/or table.
- 3) If a substantial portion of the original paper is to be used, and if you are not the senior author, also obtain the senior author's approval.

Requirements to be followed when using an entire IEEE copyrighted paper in a thesis:

- 1) The following IEEE copyright/ credit notice should be placed prominently in the references: © [year of original publication] IEEE. Reprinted, with permission, from [author names, paper title, IEEE publication title, and month/year of publication]
- 2) Only the accepted version of an IEEE copyrighted paper can be used when posting the paper or your thesis on-line.
- 3) In placing the thesis on the author's university website, please display the following message in a prominent place on the website: In reference to IEEE copyrighted material which is used with permission in this thesis, the IEEE does not endorse any of [university/educational entity's name goes here]'s products or services. Internal or personal use of this material is permitted. If interested in reprinting/republishing IEEE copyrighted material for advertising or promotional purposes or for creating new collective works for resale or redistribution, please go to http://www.ieee.org/publications_standards/publications/rights/rights_link.html to learn how to obtain a License from RightsLink.

If applicable, University Microfilms and/or ProQuest Library, or the Archives of Canada may supply single copies of the dissertation.

This is copyright permission for use of material in Chapter 5.

**SPRINGER LICENSE
TERMS AND CONDITIONS**

May 11, 2014

This is a License Agreement between sinan onal ("You") and Springer ("Springer") provided by Copyright Clearance Center ("CCC"). The license consists of your order details, the terms and conditions provided by Springer, and the payment terms and conditions.

All payments must be made in full to CCC. For payment instructions, please see information listed at the bottom of this form.

License Number	3382540249595
License date	May 05, 2014
Licensed content publisher	Springer
Licensed content publication	International Urogynecology Journal
Licensed content title	Assessment of a semiautomated pelvic floor measurement model for evaluating pelvic organ prolapse on MRI
Licensed content author	S. Onal
Licensed content date	Jan 1, 2013
Type of Use	Thesis/Dissertation
Portion	Full text
Number of copies	1
Author of this Springer article	Yes and you are a contributor of the new work
Order reference number	None
Title of your thesis / dissertation	Automated Localization and Segmentation of Pelvic Floor Structures on MRI to Predict Pelvic Organ Prolapse
Expected completion date	May 2014
Estimated size(pages)	130
Total	0.00 USD
Terms and Conditions	

This is copyright permission for use of material in Chapter 5.



jbise

to me ▾

Dear Dr. Onal,

OK, but please make sure the paper is properly cited in your new paper.

Sincerely yours,

Karen Zhang

Editorial assistant of JBISE

E-mail: jbise@scirp.org

www.scirp.org/journal/jbise/

This is copyright permission for use of material in Chapter 2.

Hello,

You have **permission** to use the image you have cited for the purposes of your dissertation.

Good luck with your career.

Dave Heiserman

Free-Ed.Net

----- Original Message ----- From: "Free-Ed.Net" <admin@waybuilder.net>

To: <daveh@free-ed.net>

Sent: Wednesday, May 07, 2014 6:02 AM

Subject: User Comment Form

User Comment

User Page: /sweethaven/MedTech/ObsNewborn/default.asp

Sender's E-Mail: sonal@mail.usf.edu

Comment

Dear Mr./ Ms.

I would like to ask a **copyright permission** for one of the images that you use in your website. (Figure 1-1. The female reproductive organs (sagittal section). I will use it for my dissertation

<http://www.waybuilder.net/sweethaven/MedTech/ObsNewborn/default.asp?iNum=10101>

This is copyright permission for use of material in Chapter 2.



Scott Leighton

11:23 AM (7 minutes ago) ☆

to me ▾

Sinan,

You have my permission to use the illustration — Please have the credit line read:

Scott Leighton, CMI
medicusmedia.com

Good luck,

Scott

Scott Leighton, CMI
Medicus Media
t [207 837 0635](tel:2078370635)
f [207 512 1100](tel:2075121100)

Find, Follow & Interact:
medicusmedia.com
facebook.com/medicusmedia
twitter.com/medicusmedia

This is copyright permission for use of material in Chapter 2.



TIM PETERS AND COMPANY, INC.

87 Main Street • Peapack, NJ 07977 USA • (908) 234-2050 • Fax (908) 234-1961

ARTWORK USAGE AGREEMENT

TO: Sinal Onal, MSEM
FR: Shane Smith
DATE: May 12, 2014
RE: Pelvic Organ Prolapse Artwork Usage

This usage agreement is between Tim Peters and Company, Inc. (TPC) and Sinal Onal. This agreement grants Sinal Onal permission to use the following illustration from the *Pelvic Organ Prolapse: An Interactive Guide*® program in a dissertation.

Pelvic Organ Prolapse

1. Stage 3: Leading Edge: Posterior Wall Prolapse

Terms and Conditions:

- The TPC copyright must appear below this illustration. The copyright line should appear as:

Illustrations ©2014 Tim Peters and Company, Inc. All Rights Reserved. Developed in consultation with Patrick Culligan, MD. Morristown, NJ

- The artwork listed above is not to be used in any other format and/or design without the written permission of TPC.
- Please fax your approval to (908) 234-1961.



Shane Smith
Vice President
Tim Peters and Company, Inc.



Sinal Onal, MSEM

05/13/2014

About the Author

After receiving his B.S. in Wood Processing Industrial Engineering from Hacettepe University, Turkey, Sinan Onal worked for twelve years in several companies in different positions and different departments. He then completed his master's degree in Engineering Management at the Department of Industrial and Management Systems Engineering in summer 2010.

In addition to this dissertation project, he has also worked on a variety of research projects, such as electronic catheter stethoscope and universal laparoscopic suturing device (in collaboration with researchers from College of Medicine) and ethanol stove for an industry partner. His works have appeared in scholarly journals such as *IEEE Journal of Biomedical and Health Informatics*, *International Journal of Urogynecology*, and *Journal of Biomedical Science and Engineering*. In addition, he has presented in high quality conferences such as *Institute for Operation Research and Management Sciences (INFORMS)* and *Information Science, Signal Processing and their Applications (ISSPA)*.

Being involved in such research projects during his graduate studies enabled him to gain experience and develop his expertise in medical image processing using machine learning, pattern recognition, and data mining for medical diagnosis, and new product development for medical applications. He plans to continue his research in this realm in the future, as he undertakes a tenure-track position as an assistant professor of Industrial and Manufacturing Engineering at Southern Illinois University, Edwardsville. He can be reached at sinanonal@gmail.com or at www.sinanonal.com